The Limits of Ultra-Fine Particle Flotation Through Entrainment in a Bubble Column to Optimize the Removal of Fission Products in a Molten Salt Reactor by Helium Bubbling

Britta Bor

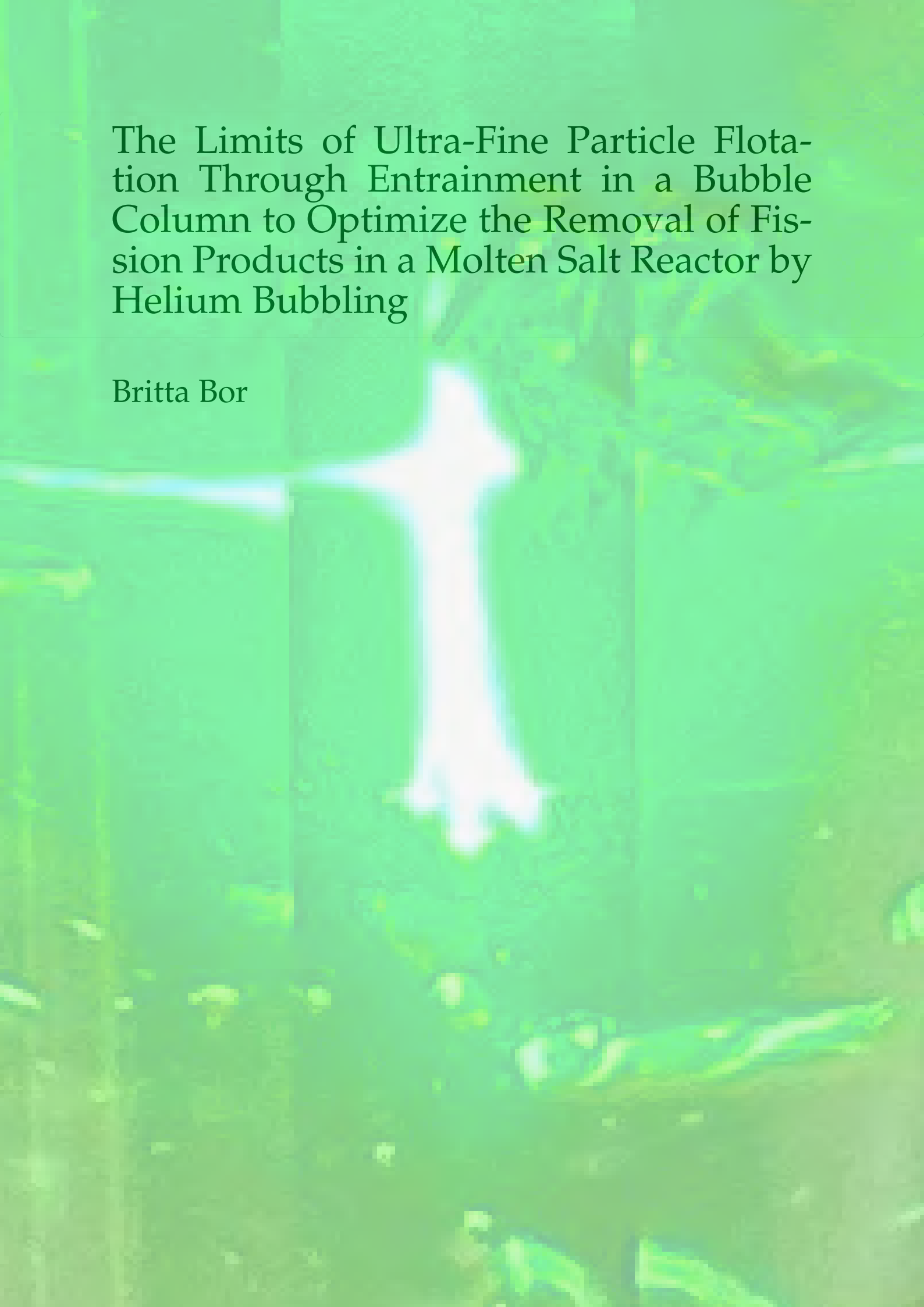

The Limits of Ultra-Fine Particle Flotation Through Entrainment in a Bubble Column to Optimize the Removal of Fission Products in a Molten Salt Reactor by Helium Bubbling

Master Thesis

by

Britta Bor
4652096

to obtain the degree of Master of Science
in Applied Physics
at the Delft University of Technology
to be defended publicly on Thursday April 18, 2024 at 15:00

September 2023 - April 2024

Committee

Dr. Ir. Martin Rohde	TU Delft, Supervisor
Dr. Ir. Ruben Dewes	TU Delft, Daily Supervisor
Dr. Ir. Danny Lathouwers	TU Delft
Dr. Stephan de Roode	TU Delft

REACTOR INSTITUTE DELFT

TU Delft

[This page has been left blank intentionally]

HIGHLIGHTS

The most noteworthy contributions of this theses are

- *A fundamental experimental study was conducted to investigate the potential of particle removal within a bubble column through entrainment. Unlike previous studies, entrainment was utilized instead of avoided as an efficient method to remove ultra-fine particles within the bubble column, demonstrating the advantages of this mechanism*
- *A simple 2D Computational Fluid Dynamics model was developed to facilitate the simulation of a single bubble rising within a bubble column and its impact on fluid streamlines influencing particle elevation within the column*

ABSTRACT

The Molten Salt Reactor is one of the revolutionary generation IV reactors currently under development to provide sustainable, safe, and economically favorable energy supply. Inside the Molten Salt Reactor fissile material is dissolved in a molten salt. Molybdenum-99, which is the precursor of Technetium-99m commonly used in radiotherapy, is one of the major insoluble fission products. Extracting Molybdenum-99 from the reactor would lead to a production of several orders of magnitudes larger than currently produced. Proposed removal solutions include an on-line bubbling system. In the Molten Salt Reactor the particles will commonly occur as ultra-fine particles, for which flotation is proven to be insufficient. Therefore, this study aims to investigate ultra-fine particle removal through entrainment and its possible application in the Molten Salt Reactor.

Two model columns were used to experimentally determine particle recovery under different conditions. To characterize the flow regime inside the column, the bubble shape was determined at different volume flows. The bubble size distributions showed evidence that when increasing the volume flow, the flow regime transitioned from a homogeneous towards a heterogeneous regime. Additionally, decreasing the column width, and increasing the inlet diameter from 1 to 1.5 and 2.5 mm, increased the bubble size. An investigation of the bubble rise velocity showed that bubbles in the large column experienced higher velocities than in the small column.

An investigation of the velocity of nickel and zinc-oxide particles for a size range of 500 nm to 10 μm showed that there was no significant difference between the different velocity distributions. Additionally, a comparison of the velocity distributions of nickel and zic-oxide particles with neutrally buoyant glass beads showed no significant difference. Thus, all particles follow the streamlines present in the column. This was confirmed by numerical simulations, where the size and the type of particle did not significantly affect the particle lift inside the bubble column.

Looking at the fraction of particles recovered in the column, in the smaller column, particle recovery reached up to values of ~ 0.7 $g \cdot g^{-1}$. This proves that particle recovery through entrainment is a promising technique for particle removal.

ACKNOWLEDGMENTS

This thesis was written as part of my master's degree Applied Physics at the TU Delft. I would like to take this opportunity to thank some people who helped me during this journey.

Firstly, I want to express my gratitude to Ruben for your guidance throughout the project and our weekly discussions, which significantly improved my thesis through your critical thinking! I wish you the besh wished with completing your postdoc and finding a job in The Hague afterwards! Secondly, I extend my appreciation to Martin for offering me the opportunity to join the group. In the few meetings that we had I admired your dedication to pose questions and engage in debates to enhance my thesis. Additionally, I want to thank my committee, I hoped you enjoyed reading about the research that I engaged in during the last few months!

Moreover, I am grateful to my parents and sisters. While I may never win a Nobel Prize, I can at least find a job and stop lending money from you. I also want to acknowledge Guus for your unwavering support during stress full times, and Nikki for your assistance in understanding statistics and guiding me towards appropriate statistical tests. Lastly, I extend my thanks to all my other friends who helped lowering my stress levels during the project.

NOMENCLATURE

Symbols

Symbol	Definition	Unit
d_{32}	Sauter mean diameter	m
v_T	Terminal rise velocity	$m \cdot s^{-1}$
F_B	Buoyancy force	N
F_D	Drag force	N
c_D	Drag coefficient	$-$
ρ_L	Density liquid	$kg \cdot m^{-3}$
ρ_G	Density gas	$kg \cdot m^{-3}$
g	Gravitational constant	$m \cdot s^{-2}$
V_b	Volume bubble	m^3
A_b	Surface area bubble	m^2
v	Velocity	$m \cdot s^{-1}$
t	Time	s
d_e	Volumetric equivalent diameter	m
d_h	Horizontal diameter	m
d_v	Vertical diameter	m
d_{inl}	Inlet diameter	m
d_c	Collector diameter	m
χ	Bubble deformation degree	$-$
d_b	Bubble diameter	m
v_b	Bubble rise velocity	$m \cdot s^{-1}$
σ	Surface tension	$N \cdot m^{-1}$
η_L	Viscosity liquid	$Pa \cdot s$
η_G	Viscosity gas	$Pa \cdot s$
D_T	Column diameter	m
$\dot{V}$	Volume Flow	$cm^3 \cdot min^{-1}$
SF	Scale Factor	$-$
AF	Acceleration Factor	$-$

P_{at}	Attachment probability	$-$
φ_{cr}	Critical angle	$^{\circ}$
P_f	Probability of thinning	$-$
P_r	Probability of rupture	$-$
P_{tpc}	Probability of expansion	$-$
k	Wave vector	$-$
λ	Wavelength	$-$
f	Frequency	Hz
Θ	Angle	rad
f_D	Doppler frequency	Hz
μ	Mean	$-$
σ	variance	$-$
$\bar{x}$	Group mean	$-$
s	Group variance	$-$
N	Sample size	$-$
α	Nominal cut-off value	$-$
R	Radius	m
S_m	Source term	$-$
τ	Stress tensor	$-$
$\dot{V}$	Volume flow	$cm^3 \cdot min^{-1}$
N_p	Number of particles	$-$
m	mass	kg
V_L	Volume liquid	m^3
R	Recovery	$g \cdot g^{-1}$
H/h	Height	m
f	Focal length	m
SS_{res}	Residual sum of squares	$-$
SS_{tot}	Total sum of squares	$-$
d_i	Bubble chord length	m
k	Recovery rate	s^{-1}

Abbreviations

Abbreviation	Definition
IPCC	Intergovernmental Panel on Climate Change
SNF	Spent Nuclear Fuel
LWR	Light Water Reactor
FMSR	Fast Molten Salt Reactor
MSR	Molten Salt Reactor
MSRE	Molten Salt Reactor Experiment
Mo	Molybdenum
Tc	Technetium
LDA	Laser Doppler Anemometry
LRHI	Long Range Hydrodynamic Interaction

BLT	Boundary Layer Theory
BWT	Bubble Wake Theory
BST	Bubble Swarm Theory
H_0	Null hypothesis
H_1	Alternative hypothesis
LRT	Likelihood Ratio Test
ANOVA	Analysis of Variance
FWHM	Full Width at Half Maximum

Constants

Symbol	Definition	Value
g	Gravitational constant	$9.81\ m \cdot s^{-2}$
μ	Kinematic viscosity	$1.0016e-3\ Pa \cdot s$
ρ_L	Density Water	$997\ kg \cdot m^{-3}$
ρ_{MS}	Density Molten-salt	1847.6
ρ_{Ni}	Density Nickel	$8900\ kg \cdot m^{-3}$
ρ_{ZnO}	Density Zinc-oxide	$5610\ kg \cdot m^{-3}$
ρ_{air}	Density Air	$1.293\ kg \cdot m^{-3}$
ρ_{He}	Density Helium	$0.166\ kg \cdot m^{-3}$
σ	Surface tension water/air	$0.0728\ N \cdot m^{-1}$
N_A	Avogadro's constant	$6.022e23\ mol^{-1}$

Non-Dimensional Numbers

Symbol	Definition	Equation
Re	Reynolds number	$\frac{\rho_L v d}{\mu_L}$
M	Morton number	$\frac{g\mu_L^4 \Delta\rho}{\rho_L \sigma^3}$
Eo	Eotvos number	$\frac{g\Delta\rho d^2}{\sigma}$
We	Weber number	$\frac{\rho v^2 d}{\sigma}$
Ar	Archimedes number	$\frac{d^3 g \Delta\rho\rho_L}{\mu_L^2}$
Ly	Lyshchenko number	$\frac{v^3 \rho_L^2}{g\Delta\rho\mu_L}$

Contents

Highlights i

Abstract ii

Acknowledgments iii

Nomenclature iv

List of Figures IX

List of Tables X

1 Introduction 1
- 1.1. The Fission Reaction . . . 2
- 1.2. MIMOSA . . . 3
- 1.3. The Molten Salt Reactor . . . 4
  - 1.3.1 Helium Bubbling for the Removal of Fission Products . . . 5
- 1.4. Thesis Outline . . . 6
  - 1.4.1 Thesis goals . . . 6
  - 1.4.2 Structure . . . 7

2 Theoretical Background 8
- 2.1. Gas-Liquid Flows in Bubble Columns . . . 8
  - 2.1.1 Bubble Behavior in Bubble Column . . . 9
    - 2.1.1.1 Formation of Gas Bubbles in Liquid . . . 10
    - 2.1.1.2 Bubble Size Distribution in Bubble Column . . . 11
    - 2.1.1.3 Bubble Rise Velocity and Shape of Gas Bubbles in Liquid Medium . . . 12
    - 2.1.1.4 Bubble Trajectories in Liquid Medium . . . 17
    - 2.1.1.5 Bubble Coalescence and Breakup . . . 17
- 2.2. Particle Separation in Bubble Column . . . 18
  - 2.2.1 The Limits of Fine Particle Flotation . . . 18
    - 2.2.1.1 Particle Collision and Attachment Models . . . 19
    - 2.2.1.2 Entrainment . . . 21
- 2.3. Laser Doppler Anemometry . . . 23
- 2.4. Useful Statistical Theories . . . 24
  - 2.4.1 Levene's test . . . 25
  - 2.4.2 Two sample t-test . . . 26

2.4.3 ANOVA test . . . 27
2.4.4 Kruskal-Wallis test . . . 28
2.5. Computational Fluid Dynamics Modeling . . . 29
2.5.1 Basis of CFD Modeling . . . 29
2.5.2 Multiphase Models using the Euler-Euler Approach . . . 30
2.5.2.1 Volume of Fluid Model . . . 30
2.5.2.2 Mixture Model . . . 31
2.5.2.3 Eulerian Models . . . 32
2.5.2.4 Discrete Phase Model . . . 33
2.5.3 Turbulence Models . . . 34
2.5.3.1 $k-\epsilon$ Models . . . 34
2.5.3.2 $k-\omega$ Models . . . 35
2.5.3.3 Reynolds Stress Model . . . 36

3 Methodology **37**
3.1. Materials . . . 37
3.2. Experimental set-up . . . 38
3.3. Experimental Procedure . . . 39
3.4. Characterization . . . 40
3.4.1 Bubble Size . . . 40
3.4.2 Bubble Rise Velocity . . . 43
3.4.3 LDA output . . . 44
3.4.4 Recovery over Time . . . 46
3.5. Numerical Simulations in Ansys Fluent . . . 47

4 Results and Discussion **51**
4.1. Quantification of Bubble Characteristics . . . 51
4.1.1 Bubble Size Distribution . . . 51
4.1.1.1 Bubble Sizes in Small Column . . . 51
4.1.1.2 Bubble Sizes in Large Column . . . 55
4.1.1.3 Bubble sizes at Formation . . . 58
4.1.2 Bubble Trajectories . . . 58
4.1.3 Bubble Rise Velocity . . . 59
4.1.4 Dimensionless numbers . . . 62
4.2. Particle Behavior in Bubble Column . . . 64
4.2.1 Bubble Induced Velocity Profiles in Water . . . 64
4.2.2 Vertical Velocity Zinc-oxide and Nickel Particles . . . 66
4.2.2.1 Small Column . . . 66
4.2.2.2 Large Column . . . 68
4.2.3 Dimensionless Analysis . . . 70
4.3. Particle Recovery . . . 71
4.3.1 Particle Recovery in Small Column . . . 71
4.3.2 Particle Recovery Difference in Large Column . . . 72
4.3.3 Particle Recovery over Time . . . 74
4.4. CFD Study of the Vertical Velocity in a Bubble Column . . . 78
4.4.1 Velocity Profiles of a Single Bubble in the Small Column . . . 78

4.4.1.1 Bubble Size Dependent Velocity without Collector 78
4.4.1.2 Velocity of Liquid Dependency on Collector 79
4.4.2 Velocity Profiles of a Single Bubble in the Large Column 80
4.4.2.1 Velocity of Liquid Dependency on Collector 80
4.4.2.2 Velocity of Multiple Bubbles and Effect of Column Shape . . 82
4.4.3 From Water and Air to Molten Salt and Helium 83
4.4.4 Convergence Issues in Ansys Fluent 83
4.5. CFD Study of Particle Lift in a Bubble Column 85
4.5.1 Particle Lift in Small Column Without collector 85
4.5.2 Particle Lift in Small Column with Collector 85
4.5.3 Particle Lift in Large Column with Collector 86
4.5.4 Particle Lift in Large Column for Multiple Bubbles 87
4.5.5 Particle Lift in Bubble Column with Molten-salt and Helium 89
4.5.6 Particle Lift in 3D 90

5 Conclusions and Recommendations **92**
5.1. Conclusions 92
5.2. Recommendations 94
5.2.1 Improvements in Experimental and Numerical Procedure 94
5.2.2 Improvements Towards Implementation in a Molten Salt Reactor 95

References **97**

Appendix **104**
A. Additional Experimental Information 104
A.1 Particle Rinsing and Particle Ejection 104
A.2 Bubble Sizes Bottom of the Column 105
A.3 Bubble Size Distribution that Visualizes Two-peaked Distribution . . . 107
A.4 Additional LDA velocity profiles 107
A.4.1 Small Column 107
A.4.2 Large Column 108
A.5 Particle Recovery at Different Volume Flows 110
A.6 Sedimentation Time 111
A.7 R^2 Values from Fits 111
A.7.1 R^2 values bubble size distributions 112
A.7.2 LDA Velocity Profiles 113
A.7.3 R^2 values time recovery 116
B. Numerical Simulations 117
B.1 Additional Velocity Profile Plots 117
B.1.1 Small Column 117
B.1.2 Large Column 119
B.2 Additional Figures for Particle Behavior 123
B.2.1 Small Column 123
B.2.2 Large Column 124
C. Python Codes 124

List of Figures

1.0.1 Median estimates of life cycle carbon intensity of selected electricity sources. The figure includes mining, raw material and waste disposal impacts, but excludes infrastructure requirements such as energy storage, strengthened transmission grid, or backup generators. Figure originally published by the IPCC in 2014 [8]. 2

1.3.1 Schematic representation of the Molten Salt Reactor [21]. 4

2.1.1 Representation of flow regimes in vertical pipes. Originally posted by Wu, B et al. and reposted by Besagni, Varallo, and Mereu (2023) [34]. 9

2.2.1 Schematic of Boundary Layer Theory and Bubble Wake Theory. Figure adopted by Wang et al. 2015 [65]. 22

2.2.2 Recovery of siderite as a function of the average particle size. A: Recovery by entrainment, B: recovery by true flotation, C: Recovery by entrainment and true flotation. Figure adopted by Wang et al. (2015) [65]. 23

3.2.1 Dissembled experimental setup (a) and schematic (b) consisting of 1: screws to assemble lower part of column set-up, 2: Column with diameter 50 mm, 3: column with diameter 30 mm, 4: inlets with different diameters, options are 1, 1.5, 2, and 2.5 mm, 5: lower part of column, where the inlet diameter can be switched, 6: gas inlet, 7: collectors, options are for the 50 mm column an opening diameter of 10 mm with angle 61.9° and for the 30 mm column an opening diameter of 10 mm with angle 64.7 ° or an opening diameter of 7.5 mm with angle 60°. 39

3.4.1 x and y coordinates obtained from python code (a) and ellipse fitted to x and y coordinates found from python code (b). Example displayed from a single bubble in the small column with a volume flow of 150 $cm^3 \cdot min^{-1}$ and inlet diameter of 1 mm. 41

3.4.2 Comparison between computational time and mean error in long and small axis of fitted ellipse. 42

3.4.3 The Dantec laser placed upon a 3D traverse system (a) and measurement position of the laser beams (b). 44

3.4.4 Decision making flowchart to determine which datasets obtained from LDA experiments could be taken together. The colors depict the following: yellow: input, green: tests performed, blue: output test, and red: output data. 46

3.5.1 Dimensions of the 50 mm column, including full shape of column. 48

4.1.1 Log-normal distribution fitted through experimentally obtained bubble chord lengths at different volume flows for the small column for inlet diameters 1 mm (a), 1.5 mm (b), and 2.5 mm (c), and a comparison for selected volume flows at the three different inlet sizes (d). The unit of the volume flow is $cm^3 \cdot min^{-1}$. The R^2 values of the fits can be found in Table A2 in the Appendix. 52
4.1.2 Sauter mean diameter for bubble size distribution at the middle of the small column for different volume flows, d_{inlet} in mm. 54
4.1.3 Log-normal distribution fitted through experimentally obtained bubble chord lengths at different volume flows for the large column with an inlet diameter of $1\ mm$ (a), and for selected volume flows for the large and the small column ith an inlet diameter of $1\ mm$ (b). The unit of the volume flow is $cm^3 \cdot min^{-1}$. The R^2 values of the fits can be found in the Appendix. 55
4.1.4 Sauter mean diameter for bubble size distribution at the middle of the large column for different volume flows, d_{inlet} in mm. 56
4.1.5 Trajectories of ten bubbles in the small column with inlet diameter $1\ mm$ at volume flow 100 (a), 300 (b), and $500\ \ cm^3 \cdot min^{-1}$ (c), small column with inlet diameter $1.5\ mm$ at volume flow 100 (d), 300 (e), and $500\ \ cm^3 \cdot min^{-1}$ (f), small column with inlet diameter $2.5\ mm$ at volume flow 100 (g), 300 (h), and $500\ \ cm^3 \cdot min^{-1}$ (i), and large column with inlet diameter $1\ mm$ at volume flow 300 (j), 400 (k), and $500\ \ cm^3 \cdot min^{-1}$ (l). 59
4.1.6 Experimentally determined velocity and Reynolds number for small and large column at different volume flows. 60
4.1.7 Experimentally determined average bubble rise velocity compared to different developed models. 62
4.1.8 Dimensionless numbers with respect to Clift regime map [59]. 63
4.2.1 Velocity profiles in vertical direction for glass hollow spheres with inlet size of 1 mm in diameter, for small column (a), and large column (b) with no collector, and with collector with opening diameter of $7.5\ mm$ and angle $60°$ for the small column (c) and the large column with collector with opening diameter $10\ mm$ and angle $61.9°$ (d). 64
4.2.2 FWHM of velocity distributions for glass hollow spheres (a) and velocity distribution maximum for LDA velocity profiles (b) in Figure 4.2.1. 65
4.2.3 Velocity profiles in vertical direction in small column with inlet diameter of $1\ mm$ for different particles with volume flow of $100\ \ cm^3 \cdot min^{-1}$. 67
4.2.4 FWHM (a) and velocity at maximum of velocity distribution (b) at a volume flow of $100\ \ cm^3 \cdot min^{-1}$ for an inlet of $1\ mm$ in Figure 4.2.3. 67
4.2.5 Velocity distribution in vertical direction (a) and corresponding FWHM (b) and maximum of velocity distribution (c) with inlet diameter of $1\ mm$ for $1\ \mu m$ nickel particles with volume flow of $100\ \ cm^3 \cdot min^{-1}$ and $200\ \ cm^3 \cdot min^{-1}$ over time. 68
4.2.6 Velocity profiles in vertical direction in large column with inlet diameter of $1\ mm$ for nickel particles with volume flow of $400\ \ cm^3 \cdot min^{-1}$, velocity profile of $500\ nm$ particles obtained at power of $210\ mW$. 69
4.2.7 FWHM (a) and velocity at maximum of velocity distribution (b) at a volume flow of $400\ \ cm^3 \cdot min^{-1}$, and inlet diameter of $1\ mm$ corresponding to Figure 4.2.6. 69

4.2.8 Stokes number for a range of bubble sizes with velocity described by Equation 2.23, jumps in Stokes number occur due to the change in $\frac{d_b}{D_T}$, which affects the SF in the determination of the bubble rise velocity. w_{column} is given in mm. . . 70
4.3.1 Particle recovery for a range of sizes of zinc-oxide and nickel particles at a volume flow of $100\ cm^3 \cdot min^{-1}$ in the small column, d_{inl} is given in mm. . . 71
4.3.2 Particle recovery for a range of sizes of nickel particles at different volume flows in the large column. 73
4.3.3 Particle recovery over time for $10\ \mu m$ zinc-oxide and nickel particles, fitted with Equation 3.14, for different inlets, volume flows, and collector opening diameters, $\dot{V}$ is given in $cm^3 \cdot min^{-1}$, d_i in mm, and d_c in mm. 75
4.3.4 Particle recovery over time for differently sized nickel particles, fitted with Equation 3.14 at volume flow $400\ cm^3 \cdot min^{-1}$. 76
4.4.1 Velocity profiles of water in the small column with no collector with bubble equivalent diameter 7.5 (a), 10 (b), and $15\ mm$ (c), the unit of the position is given in mm, of time in s which indicates the flow-time of the simulation. Positions with zero velocity can indicate the position of the bubble. 79
4.4.2 Velocity profiles of water in the small column with collectors $d_{opening} = 7.5\,mm$, $\theta = 60°$ (a), and $d_{opening} = 10\ mm$, $\theta = 64.7°$ (b) with bubble equivalent diameter $10\ mm$, the unit of the position is given in mm, of time in s which indicates the flow-time of the simulation. Positions with zero velocity can indicate the position of the bubble. 80
4.4.3 Velocity profiles of water in the large column with collectors $d_{opening} = 7.5\,mm$, $\theta = 60°$ (a), and $d_{opening} = 10\ mm$, $\theta = 61.9°$ (b) with bubble equivalent diameter $10\ mm$, the unit of the position is given in mm, of time in s which indicates the flow-time of the simulation. Positions with zero velocity can indicate the position of the bubble. 81
4.4.4 Velocity profiles of water in the large column with a collector with opening diameter of $10\ mm$ and angle $61.9°$ for a bubble with equivalent diameter of $15\ mm$ (a), where the conical shape is included (c), and for a second round of bubbles excluding (b), and including the conical shape (d), the unit of the position is given in mm, of time in s which indicates the flow-time of the simulation. Positions with zero velocity can indicate the position of the bubble. . . 82
4.4.5 Velocity of molten salt induced by a helium bubble with bubble equivalent diamter of $10\ mm$ in the small column with the collector with opening diameter $10\ mm$ and angle $64.7°$ 84
4.5.1 Particle lift of different sized zinc-oxide and nickel particles in the small column, with a bubble with bubble equivalent diameter of 10 mm after a flow-time of $1.9\ s$. 86
4.5.2 Particle lift of $10\ \mu m$ nickel particles in the small column with collectors $d_{collector} = 7.5\,mm$, $\theta = 60°$ (a), and $d_{collector} = 10\,mm$, $\theta = 64.7°$ (b), with a bubble with bubble equivalent diameter of $10\ mm$, the timeline is given in s of flow-time. . 87
4.5.3 Particle lift of $10\ \mu m$ nickel particles in the large column with collectors $d_{collector} = 7.5\,mm$, $\theta = 60°$ (a), and $d_{collector} = 10\,mm$, $\theta = 61.9°$ (b), with a bubble with bubble equivalent diameter of $10\ mm$, the timeline is given in s of flow-time . . 88

4.5.4 Particle lift of $10\ \mu m$ nickel particles in the large column, with three bubbles with bubble equivalent diameter of $4.3\ mm$ (a), and a second round of bubbles (b), with collector with opening diameter of $10\ mm$ and angle of $61.9°$, the timeline is given in s of flow-time. 89

4.5.5 Particle lift of $10\ \mu m$ nickel particles in the small column with the addition of a collector with opening diameter of 10 mm and angle $64.7°$ and a bubble equivalent diameter of $10\ mm$ in molten salt of a helium bubble, the timeline is given in s of flow-time. 90

A1 $500\ nm$ nickel particles before particle collection, after particle collection, and after rinsing. 104

A2 $10\ \mu m$ of zinc-oxide with $7.5\ mm$ collector and inlet diameter of $1\ mm$ at volume flow of $300\ cm^3 \cdot s^{-1}$. Many particles were ejected out of the column, leading to an underestimation of particles recovered. 105

A3 Log-normal distribution fitted through experimentally obtained bubble chord lengths at different volume flows for the small column for inlet diameters 1 mm (a), 1.5 mm (b), and 2.5 mm (c), and a comparison for selected volume flows at the three different inlet sizes (d). The unit of the volume flow is $cm^3 \cdot min^{-1}$. The R^2 values of the fits can be found in Table A2. 106

A4 Sauter mean diameter for bubble size distribution at the bottom of the small column for different volume flows. The inlet diameter is given in mm. 106

A5 Bubble size distribution for bubbles measured at volume flow of 300, inlet diameter of 1.5. From here it becomes evident that for this bubble size distribution the fit would probably benefit from a two-peaked distribution rather than a one-peak distribution. 107

A6 Velocity distribution in vertical direction for glass beads with inlet size of 1 mm in diameter, for small column, with collector with 10 mm opening diameter and angle of 64.7°. 107

A7 Velocity distribution in vertical direction for small column with inlet diameter of $1.5\ mm$ (a), and $2.5\ mm$ (b) at a volume flow of $100\ \ cm^3 \cdot min^{-1}$ for different particles. 108

A8 FWHM of velocity profiles in vertical direction with inlet diameter of $1.5\ mm$ (a), and $2.5\ mm$ (c) for different particles with volume flow of $100\ \ cm^3 \cdot min^{-1}$, and the velocity at the maximum of the velocity distribution with inlet diameter $1.5\ mm$ (b) and $2.5\ mm$ (d) for Figure A7. 108

A9 Velocity distribution in vertical direction for large column with inlet diameter of $1\ mm$ for nickel particles with volume flow of 350 (a), 450 (b), and $500\ \ cm^3 \cdot min^{-1}$ (c). 109

A10 FWHM of velocity profiles in vertical direction of large column with inlet diameter of $1\ mm$ for different particles with volume flow of 350 (a), 450 (c), and $500\ \ cm^3 \cdot min^{-1}$ (e) and velocity at maximum of velocity profiles in vertical direction of large column with inlet diameter of $1\ mm$ for different particles with volume flow of 350 (b), 450 (d), and $500\ \ cm^3 \cdot min^{-1}$ (f) for Figure A9. . 110

A11 Particle recovery at different conditions in small column. 111

B1 Velocity profiles of water in the small column with no collector for a bubble equivalent diameter of $5\ mm$ (a), and $12.5\ mm$ (b), the unit of the position is given in mm, of time in s which indicates the flow-time of the simulation. Positions with zero velocity can indicate the position of the bubble. 117

B2 Velocity profiles of water in the small column with the collector with opening diameter $7.5\ mm$ and angle $60°$ (a), and opening diameter $10\ mm$ and angle $64.7°$ (b) for a bubble equivalent diameter of $6.5\ mm$, the unit of the position is given in mm, of time in s which indicates the flow-time of the simulation. Positions with zero velocity can indicate the position of the bubble. 118

B3 Velocity profiles of water in the small column with opening diameter $7.5\ mm$ and angle $60°$ (a), and opening diameter $10\ mm$ and angle $60°$ (b) for a bubble equivalent diameter of $8\ mm$, the unit of the position is given in mm, of time in s which indicates the flow-time of the simulation. Positions with zero velocity can indicate the position of the bubble. 118

B4 Velocity profiles of water in the large column with the collector with opening diameter $7.5\ mm$ and angle $60°$ for a bubble equivalent diameter of $6.5\ mm$ (a) and $8\ mm$ (b), and with the collector with opening diameter $10\ mm$ and angle $61.9°$ for a bubble equivalent diameter of $6.5\ mm$ (c) and $8\ mm$ (d), the unit of the position is given in mm, of time in s which indicates the flow-time of the simulation. Positions with zero velocity can indicate the position of the bubble. 119

B5 Velocity profiles of water in the large column for three bubbles with equivalent diameter of $4.3\ mm$ with a collector with opening diameter of $10\ mm$ and angle $61.9°$ (a), a second round of bubbles (b), and including the cone shape for three bubbles (c), and a second round of three bubbles (d), the unit of the position is given in mm, of time in s which indicates the flow-time of the simulation. Positions with zero velocity can indicate the position of the bubble. 120

B6 Velocity profiles of water in the large column for two bubbles with equivalent diameter of $5.8\ mm$ with a collector with opening diameter of $10\ mm$ and angle $61.9°$ (a), a second round of bubbles (b), and including the cone shape for two bubbles (c), and a second round of three bubbles (d), the unit of the position is given in mm, of time in s which indicates the flow-time of the simulation. Positions with zero velocity can indicate the position of the bubble. 121

B7 Velocity profiles of water in the large column for a second round of two bubbles with equivalent diameter of $7.1\ mm$ with a collector with opening diameter of $10\ mm$ and angle $61.9°$ (a), and including the conical shape (b), the unit of the position is given in mm, of time in s which indicates the flow-time of the simulation. Positions with zero velocity can indicate the position of the bubble. 121

B8 Velocity profiles of water in the large column for a second round of three bubbles with equivalent diameter of $5.4\ mm$ with a collector with opening diameter of $10\ mm$ and angle $61.9°$ (a), and including the conical shape of the column (b), the unit of the position is given in mm, of time in s which indicates the flow-time of the simulation. Positions with zero velocity can indicate the position of the bubble. 122

B9 Velocity profiles of water in the large column for a bubble with equivalent diameter of $20\ mm$ with a collector with opening diameter of $10\ mm$ and angle $61.9°$ (a), and including the conical shape of the column (b), the unit of the position is given in mm, of time in s which indicates the flow-time of the simulation. Positions with zero velocity can indicate the position of the bubble. . . 122
B10 Particle lift of $10\ \mu m$ molybdenum particles in the small column, with a bubble with bubble equivalent diameter of $10\ mm$, with a collector with opening diameter $10\ mm$ and angle $64.7°$, the timeline is given in s of flow-time. 123
B11 Particle lift of $10\ \mu m$ nickel particles in the large column, with a bubble with bubble equivalent diameter of $15\ mm$, with a collector with opening diameter $10\ mm$ and angle $61.9°$, the timeline is given in s of flow-time. 124

List of Tables

3.1 All particles used in experimental work. 38
3.2 Constants used to scale pixels to metric size. 41
3.3 Conditions differed in videos to determine bubble rise velocity. 43
3.4 All sizes of the meshes used. 47

4.1 Dimensionless numbers for bubbles under different conditions. 62

A1 Sedimentation time for different particles in the small and the large column, velocity calculated as described in Equation 2.37. 111
A2 All R^2 values for bubble size distributions. 112
A3 Data glass beads small and large column, w_{column} is given in mm, $d_{collector}$ in mm, $\Theta_{collector}$ in $^\circ$, and $\dot{V}$ in $cm^3 \cdot min^{-1}$. 113
A4 Data zinc-oxide particles at volume flow of $100\ \ cm^3 \cdot min^{-1}$ in small column with different inlet diameters, w_{column} is given in mm, d_{inlet} in mm, and $\dot{V}$ in $cm^3 \cdot min^{-1}$. 114
A5 Data nickel particles with collector for large column at different volume flows and inlet diameter of $1\ mm$, w_{column} is given in mm, and $\dot{V}$ in $cm^3 \cdot min^{-1}$. . . 115
A6 Data $1\ \mu m$ nickel particles with collector for small column at different volume flows and inlet diameter of $1\ mm$ at different points in time. 116
A7 Data for particle recovery over time. 116

CHAPTER 1

INTRODUCTION

In December 2019 the European Council agreed that the European Union should achieve climate neutrality by the year 2050. Additionally, by the year 2030 the emission of greenhouse gases by the European Union should be 55% lower compared to the levels in 1990 [1]. This movement has been produced by a global concern of the changing climate and its consequences. Climate change is in great part due to human perturbation in the natural carbon cycle, which started at the beginning of the Industrial Revolution [2]. The Industrial Revolution generated the change from an agrarian and handicraft economy to one dominated by industry and machine manufacturing, resulting in a world dependent on energy production. This energy is mainly derived from the exploitation of fossil fuels [3, 4]. Across many countries in the world, the demand for energy is growing each year with the increase in wealth and population. This growing energy consumption makes the transition from burning fossil fuels to generate energy towards low-carbon sources of energy even more difficult. The new energy source has to be able to meet this additional demand, whilst replacing the existing fossil fuels simultaneously [5]. Powering an energy system by clean energy technologies like solar photovoltaic plants, and wind farms generally requires more minerals, including rare earth elements (REEs), than their fossil fuel-based counterparts. Minerals, that have a limited supply on Earth [6]. Moreover, the rapid development of existing green energy technologies leads to an unsustainable consumption of REEs, leading to environmental problems of its own. These include environmental degradation due to dust that contains REE, other toxic metals and chemicals that is generated during the primary production of REEs, and excessive water consumption during the processing of REEs [7]. Another disadvantage of green energy technologies like wind mills and solar panels is their variability. Consequently, to ensure reliable electricity generation, it is highly likely that additional infrastructure will be required to transport electricity from locations with high wind and sun capacity to areas where demand for electricity exists. This then results in both economic and environmental costs, resulting in a higher carbon footprint. Therefore, to be able to achieve energy security sustainably, many of the world's nations are turning their eyes to nuclear power. In 2014 the Intergovernmental Panel on Climate Change (IPCC) published the median estimates of life cycle carbon intensity of some selected electricity sources. According to Figure

1.0.1 the CO_2 emissions of wind energy are equal to nuclear energy. However nuclear energy reduces CO_2 emissions compared to solar panels. Since in Figure 1.0.1 infrastructure requirements such as energy storage are excluded, some people might suggest that nuclear power is the most important electricity source today [8]. However some limitations to nuclear energy still remain. Among these are radioactive waste production, risk of accidents, an expensive initial cost to build a powerplant, and a limited fuel supply. Furthermore, nuclear powerplants take at least five to ten years to build, and are therefore not a quick solution to the environmental problem [9]. Nuclear energy retains its potential as a complementary resource, offering reliable low-carbon base-load electricity to a system that exploits wind mills and solar panels. However, to ensure the safety, public acceptance, and affordability of nuclear energy, necessary advancements should be developed [10]. To understand these ongoing innovations, it is required to first establish an understanding of fundamental principles underpinning nuclear power. Hence, the next section will feature where nuclear energy originates from.

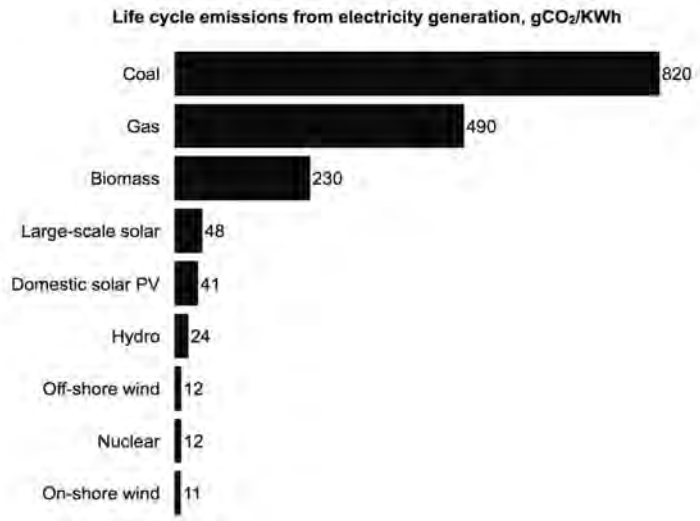

Figure 1.0.1: Median estimates of life cycle carbon intensity of selected electricity sources. The figure includes mining, raw material and waste disposal impacts, but excludes infrastructure requirements such as energy storage, strengthened transmission grid, or backup generators. Figure originally published by the IPCC in 2014 [8].

1.1. The Fission Reaction

Nuclear energy comprehends both fission reactions and fusion reactions. For the scope of this thesis, the focus will be on fission reactions only. In a fission reaction neutrons are used to induce the splitting of a heavy nuclei. These heavy nuclei then fission into lighter nuclei (fission products), accompanied by the release of energy plus some additional neutrons. These fission neutrons can then be utilized to induce new fission reactions, thereby creating a nuclear chain reaction, where each neutron is responsible for the splitting of one atom. This can be written down as a mass and energy balance

as follows

$$Neutron + Fissionable\,material \rightarrow Fission\,products + Neutrons + Energy.$$

Conventional fissionable materials include uranium [11]. The International Energy Agency (IEA) and the Nuclear Energy Agency (NEA) predicted that nuclear energy will remain the low-carbon technology with the lowest expected costs in 2025. Where levelised costs of generating electricity (LCOE) including long term operation costs for nuclear power remain below $33\ \$/MWh$ with a discount rate of 3%, the costs for coal, gas, utility-scale solar, and onshore/offshore wind power will be notably higher, at 92, 106, 126, $104/157\ \$/MWh$, respectively [12]. While uranium is inexpensive, there is no eternal supply of uranium on Earth. Therefore, in nuclear reactor development, the need arises to close the fuel cycle with expanded breeding of fuel using not only uranium but also thorium [13]. Another objective to nuclear energy is the production of radioactive waste [14]. This could also be solved by closing the fuel cycle. Therefore, closing the fuel cycle will reduce the radioactive waste disposal footprint by using waste as fuel and the need for natural resources by breeding fuel. To close the fuel cycle one needs to be able to reprocess spent nuclear fuels (SNFs) and extract elements that can be (re)used [15]. For this purpose, the MIMOSA project was initiated.

1.2. MIMOSA

The MIMOSA project aims to develop a multi-recycling strategy for spent nuclear fuels from light-water reactors based on molten salt technologies. This involves reprocessing of SNFs and the extraction of elements that can be (re)used. Specifically, the project aims to formulate and demonstrate an integrated muti-recycling strategy of plutonium and uranium that combines multi-recycling options in Light Water Reactors (LWRs) with recycling of plutonium and other transuranics in a Fast Molten Salt Reactor (FMSR) using chloride salt. To this end, twelve partners, including the TU Delft, are researching various aspects to establish the targets formulated [15].

To provide nuclear energy that meets the energy demands of the future, the future generation of nuclear energy systems, needs to meet certain standards. The evolution of nuclear power plants can be classified into four categories. The generation I reactors are the early prototypes of several different designs. Generation II nuclear reactors include commercial power plants, usually Light Water Reactors (LWRs), that are reliable and economically competitive. The generation III reactors comprehend further developments in generation II LWRs. Finally, the generation IV reactor designs contains a list of promising nuclear reactor designs currently under development [16]. The generation IV reactors should account for fundamental issues that are often cited as arguments against nuclear energy. These issues include nuclear resources, breeding fuel cycle, safety, radioactive-waste and their incineration, nuclear proliferation and terrorism, and public and institutional acceptances related not only to the previously discussed topics, but also with the technological simplicity, flexibility, and economy in the global applications [17]. Six revolutionary reactor designs were selected in the Generation IV reactors, one of which is the Molten Salt Reactor (MSR) [16].

1.3. The Molten Salt Reactor

The concept of the MSR was originally developed in the 1950s with the Aircraft Reactor Experiment, and a MSR was build with the MSR Experiment (MSRE) in the 1960s. Shortly after, the research in the MSR declined in favor of LWR technology, due to the market demands to make step-change improvements to existing LWR technology. However, a renewed interest in the MSR has taken hold [18], as the MSR is considered to have the greatest inherent safety as compared to the other six Generation IV advanced nuclear reactor designs [19, 20]. The design of the MSR is visualized in Figure 1.3.1.

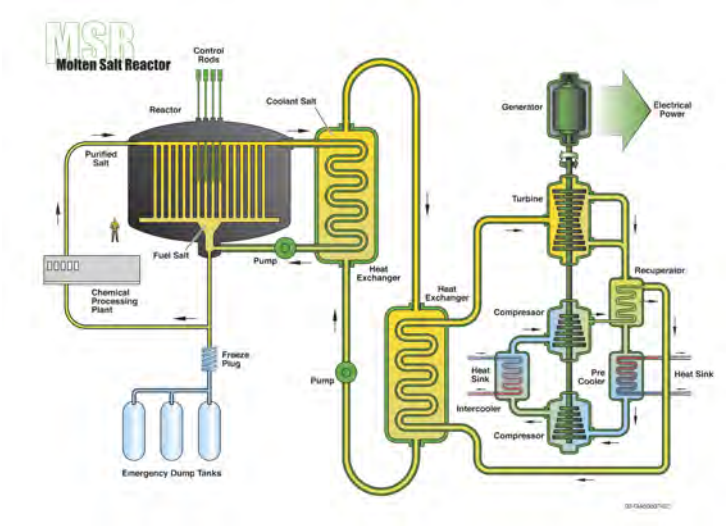

Figure 1.3.1: Schematic representation of the Molten Salt Reactor [21].

In the MSR the fissionable material is dissolved in the molten salt. A salt is an ionically bonded chemical, which consists of positively and negatively charged ions. Salts have typically high melting ranges, and reasonable thermodynamic properties at their melting temperatures [16, 18]. Additionally, molten salts are chemically and physically stable, contain a wide liquid temperature range, have high thermal conductivity and specific heat capacity, low viscosity, are non combustible, have a low price, and are abundant in supply [22]. The molten salt in the MSR serves as both fuel and coolant. The fuel salt is pumped through the core, and through a heat exchanger where it transfers heat to a secondary salt system. The secondary system then generates steam in another heat exchanger, from which electricity can be produced [23].

Inside the MSR the molten salt can be heated to high temperatures, even greater than 700 °C, without boiling while remaining at near atmospheric pressure. Operating at atmospheric pressure is advantageous, since reactor vessels capable of maintaining high pressure are expensive and difficult to produce. Operating at high temperature increases the efficiency of the nuclear reactors [24]. In addition, the MSR design includes an increased safety aspect compared to other nuclear reactor designs, since there is no concern of melting fuel or fission products that leak into the cladding even at the operation at low pressure. Additionally, continuous separation of fission products and noble gases ensures that they are non-influential in the event of an accident.

Due to the fact that the fuel salt is a stable liquid, no expansions or explosion can occur that are typically associated with LWRs. Moreover, the MSR is economically favorable since the core design is simplified, the structural section thickness is reduced due to lower operating pressure, which reduces manufacturing costs. The liquid nature of a MSR provides a series of advantages. Firstly, a higher heat capacity, which aids in the design of compact. Secondly, the reactor design is less-expensive, resulting in compact reactors that can be mass-produced and shipped to reactor sites, which reduces construction costs. Lastly, used LWR fissile material could be utilized to start up a reactor, reducing waste materials. Additionally, the MSR has the ability to breed fuel, like thorium, to produce fuel. Thorium is more abundant than uranium, which would increase the global fuel supply. Actinides can be burned or recycled, which reduces the global stock of nuclear waste. Plutonium can be recycled and burned in the MSR as well, preventing plutonium generation that could be utilized for non-proliferation purposes. Additionally, the MSR has been proposed to be able to be operated both in the fast and thermal regime [16, 18, 21, 24, 25].

There are however also some drawbacks to the MSR. Firstly, the molten salt has been proposed to be fluorine based, because fluorine has only one stable isotope [26]. Fluorine salts are highly corrosive to metallic alloys, resulting in a vessel that would need regular replacement, which increases expenses. As an alternative to fluoride salts, chloride salts could be used. Since chloride salts are more thermodynamically favored than the transition metal chlorides, it is expected that the salt would not be reduced by common alloying events, and thus no corrosion should occur when structural alloys are in contact with molten chloride salts. The corrosion in molten chlorides is therefore to a great extent driven by the impurities in the salt. Chloride ions can destabilize passive surface oxide films, however, the fluxing action is not as severe as fluoride salts [27]. Another drawback of the MSR can arise through insoluble fission products created from the fissile material.

1.3.1. Helium Bubbling for the Removal of Fission Products

After fission, fission products are generated in the liquid fuel during burn up that are free to migrate and mix in the reaction, rather than being held stationary as in a solid fuel pellet. Fission products can be grouped into salt-seekers, and insoluble fission products. The salt-seeking fission products remain with the fuel salt in inventory amounts. However, the insoluble materials are in the form of noble gases and noble metals, and form gaseous bubbles and solid particles. These insoluble fission products may affect the spatial dependence of the fuel-salt composition. It is important to remove these insoluble fission products, since build-up of fission products to the reactor vessel can lead to patches of heat and radioactivity, that can result in precarious conditions [20, 28, 23].

To remove fission products from the MSR, an on-line bubbling system is proposed that removes both gaseous fission products via dilution and metallic insoluble particles via capillary sticking [29, 30]. A carrier gas that does not interact with the molten salt, is injected in the fuel circuit from the bottom, put in contact with the fuel salt, and extracted from the top [29, 30]. Before being able to implement the on-line bubbling

system, the efficiency of the insoluble fission products extraction by helium bubbling needs to be demonstrated. If the efficiency would be proven to be insufficient, this would drastically alter the life-time of certain components in the MSR and thus compromise the safety of the MSR design [26].

Another reason for the removal of fission products in the MSR is that the fission products produced can be utilized. The noble metals include Niobium, Molybdenum, Ruthenium, Antimony, and Tellurium [23]. Molybdenum is majorly formed in the form of Molybdenum-99, or Mo-99. Mo-99 is the parent isotope of Technetium-99m, or Tc-99m, which is the most common used radioisotope in medicine. Since Tc-99m has a relatively short half-life of $6\ h$ which brings challenges with storage and transportation of Tc-99m, often Mo-99 is extracted since it has a much larger half-life of $66\ h$. Nowadays, Mo-99 is either produced by inducing fission in uranium targets, or by irradiation of Mo-98 targets in a separate reactor. In the MSR the possibility arises to extract Mo-99 from the fuel that is powering the reactor, so that no additional reactor needs to be build next to the reactors producing electricity. Since the Mo-99 will be extracted from the fuel, the rate of Mo-99 production has the potential to be of several orders of magnitude larger than that from current reactors. Additionally, since the Mo-99 will be extracted continuously, this would lead to a smaller fraction of isotopes being lost due to decay [31].

1.4. Thesis Outline

In this section the goals proposed in this thesis and the structure will be reviewed.

1.4.1. Thesis goals

The objective of this thesis is to contribute to the ongoing research on the MSR, with a specific focus on closing the fuel cycle by removing non-soluble fission products from the molten salt. To this end, both experimental work and numerical simulations have been carried out. In the experimental part a model column was used to quantify the limits of ultra-fine particle flotation through entrainment in the set-up. The column was filled with water, and air bubbles were formed at the gas inlet. Then the bubbles ascended to the top of the column, leading to particles following in their trails. Water and air was used as a replacement for molten salt and helium, because of its easier use. With the help of numerical simulations, a simple model was implemented for additional information of particle and bubble behavior inside the bubble column.

This thesis aims to answer the question whether there is an trade-off between bubble size, particle size, and particle density on particle recovery. As a part of the main question, some sub-questions have been identified. First, what mechanism can be used to recover ultra-fine particles with bubbling and lift them up to the top of the column? Secondly, what is the optimal volume flow, consequently the optimal bubble size for the most effective particle removal? Thirdly, what is the size-range of fission particles being recovered for which particle removal is possible? Lastly, what would be the influence of replacing water with molten salt and air with helium bubbles on the effectiveness of particle removal in the column?

1.4.2. Structure

This current chapter has provided the relevance of the ongoing research in the MSR development, by introducing the need for a sustainable energy source and the possibility of the MSR to fill this gap. Additionally, the research goals have been presented. In Chapter 2 the necessary theoretical background will be examined. This background includes flow patterns in a bubble column, bubble behavior, particle behavior, Laser Doppler Anemometry (LDA), useful statistical tests, and numerical models. In Chapter 3 the experimental, and numerical approach is reviewed. In Chapter 4 the Results are considered. In Section 4.1 the quantification of bubbles in the bubble column, including the bubble size, trajectory, and bubble rise velocity is discussed. Section 4.2 provides an overview of particle behavior in the column. Here the main objective lies in the bubble induced velocity of the particles. Section 4.3 concerns the effectiveness of particle removal in the model column. And Sections 4.4, and 4.5 deal with results obtained from numerical simulations, including the velocity profiles in water induced by a single bubble, and the dependency of particle behavior on the bubble size. Finally, Chapter 5 presents the conclusions and further recommendations that can be drawn from this thesis.

CHAPTER 2
THEORETICAL BACKGROUND

This section provides a complete, but concise theoretical framework of the relevant background information needed to understand concepts discussed in this thesis. To this end, first flows in a bubble column, including bubble behavior and bubble-particle behavior are reviewed, then a relevant measurement technique to determine flow patterns in the bubble column is described in Section 2.3. Thirdly, section 2.4 provides an outline of relevant statistical theories used in this thesis. Lastly, the numerical background in computation fluid dynamics modeling is provided.

2.1. Gas-Liquid Flows in Bubble Columns

Gas-liquid flows are a type of two-phase flow. Two-phase flow is a type of multi-phase flow, which in turn is defined as a flow in which more than one phase, i.e., gas, solid and liquid, occurs [32]. A wide range of industrial systems, including bubble columns, feature gas-liquid flows [33]. Bubble columns are a class of gas-liquid multiphase reactors widely used in chemical, biochemical, and petrochemical industries. They are of simple design - there are no moving parts present or a need for mechanical stirring, they include excellent heat and mass transfer properties, have low maintenance and operating costs, and a high durability. The simplest bubble column includes a vertical vessel without internals, with some kind of gas injection system. In general, in a vertical vessel, i.e., pipe, four flow regimes can be encountered, see Figure 2.1.1 [34]. At low gas volume fractions, the flow consists of a composition of individual gas bubbles rising to the top. This flow regime is classified as a bubbly flow, and can be further divided into two sub-regimes - bubble flow occurring at lower liquid flow rates, and dispersed bubble flow occurring at higher liquid flow rates. When increasing the volume fraction of the gas, a pattern materializes called slug flow. The Taylor bubbles encountered in slug flow have a spherical cap nose and are somewhat rectangular at the bottom edge. The Taylor bubbles are separated from each other, and in this area smaller bubbles may be present. The size of the bubbles can vary considerably, resulting in an unsteady accumulation of bubbles, producing the flow regime known as churn-turbulent flow. When increasing the gas velocity, the annular flow regime is

observed. Here parts of the liquid flows along the pipe, and the other part is observed as droplets entrained in the gas flow. At even higher gas velocities, no considerable amount of liquid is encountered in the gas core [33].

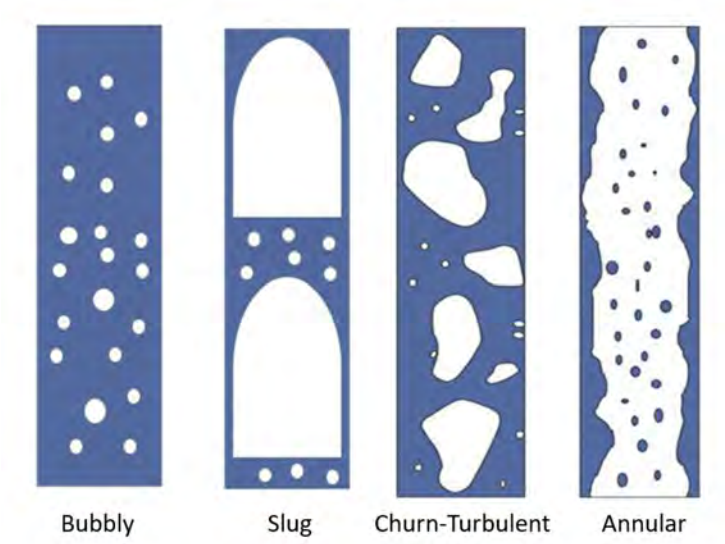

Figure 2.1.1: Representation of flow regimes in vertical pipes. Originally posted by Wu, B et al. and reposted by Besagni, Varallo, and Mereu (2023) [34].

In a bubble column, generally bubbles are generated by injection of a gas flow through a needle, a sparger or, an orifice on a solid wall under parallel flow [35]. Depending on the velocity of the gas flow into the inlet, bubble columns can be operated in different flow regimes. When there are no solids present in the column, there are two typical regimes, the homogeneous, i.e., uniform and laminar, and heterogeneous, i.e., nonuniform and churn-turbulent, flow regimes. The homogeneous regime occurs at low gas flow rates, and turns into the heterogeneous regime at high gas flow rates. The homogeneous regime is characterized by relatively small uniform gas bubbles, and the gas holdup increases almost linearly with increasing superficial gas velocity. The heterogeneous regime, where churn-turbulent flow occurs, is characterized by vigorous bubble coalescence and break-up, high bubble rise velocities, and much larger, less-uniform bubbles. When increasing the gas velocity the flow transitions from a homogeneous to a heterogeneous regime. The flow regime transition and heterogeneous regime are difficult to characterize [36, 37, 38].

The performance of the bubble column is influenced by microscopic phenomena, such as bubble formation, dynamic equilibrium between bubble coalescence and breakup, liquid flow pattern, energy dissipation rate, and wall effect [39]. The upcoming sections will highlight some physical aspects of these phenomena.

2.1.1. Bubble Behavior in Bubble Column

Since fluid patterns inside a bubble column are dependent on the formation of bubbles it is important to understand the formation of bubbles and how it influences the bubble size, rise velocity, and trajectory. The bubble rises due to buoyancy, but its shape

and velocity depends on the balance of forces produced by surface tension, inertia, and viscosity [40]. Furthermore, multiple bubbles are present in the bubble column, therefore bubbles might interact with each other, thereby influencing the conditions found in the bubble column. To understand the bubble behavior, the next sections will provide an understanding of essential processes that occur in the bubble column.

2.1.1.1. Formation of Gas Bubbles in Liquid

Gas bubble formation in a liquid includes two steps. Firstly, the growth of the bubble occurs, and secondly the detachment of the bubble from the location of formation. The growth and detachment of the bubbles can occur in a variety of ways and are mostly dependent on the purpose and the actual conditions of the bubble formation process. For example, the gas injection conditions can influence the characteristics of the bubbles. When studying the bubble formation process, often a constant volumetric gas flow rate is assumed, although this condition is not always easy to achieve [35].

Jamialahmadi et al. (2001) argued that depending on the controlling mechanisms, there are three forces that control the mechanism of bubble formation. Surface tension, viscous drag, and liquid inertia all contribute to the bubble detachment diameter. At very small volume flow rates, the bubble diameter is controlled entirely by surface tension and buoyancy forces. Whereas at high gas volume flow rates, the effect of surface tension is generally considered negligible for liquids with low viscosity [41]. However Terasaka and Tsuge noted that next to surface tension, viscous drag, and liquid inertia, gravity, buoyancy, gas momentum transfer, and drag force are also involved in bubble development on the orifice. At low gas flow rates, the bubbles are grown in the form of individual bubbles until detachment occurs, whereas when increasing the flow rate, bubble growth starts to be affected by the wake of the preceding bubbles. In this case, the bubbles elongate in the vertical direction and show a slightly earlier detachment. The detached bubble then accelerates into and collides with the preceding bubbles. The collision causes bubble aggregates, which either coalesce or segregate depending on the magnitude of the collision momentum energy. When increasing the gas flow rate further, the detachment period of the bubble increases, which generates very large bubbles with vigorously vibrating and unstable surfaces. The collision of these large bubbles may cause numerous microscopic collisions at the interface between the bubbles, which produces a lot of small bubbles [39].

Upon detachment of the bubble, a residual small bubble remains attached to the orifice. While still anchored to the orifice edge, the small bubble starts to grow at constant volumetric flow rate [35]. The increase in bubble volume leads to an increase in buoyancy. Once the buoyancy and inertia overcome the surface tension and viscous drag, a gas neck forms and continuously thins to a thread [42]. When the bubble has grown sufficiently large, the bubble is stretched due to buoyancy force, leading to rapid detachment. The continuous gas flow through the injection orifice prevents the interface retracting back inside the orifice after its neck break. However, the interface does move back to the orifice and, after a very short oscillation, it forms a small bubble anchored to the edge of the orifice before the bubble starts to rise [35].

After formation of bubbles, further characterization of the bubbles is needed, since

the overall mass transfer is affected by the bubble size, pressure inside the gas phase, interaction between bubbles, rise velocity and trajectory [43]. In the following sections, characterizations of the bubble size, the rise velocity, and the bubble trajectories are examined.

2.1.1.2. Bubble Size Distribution in Bubble Column

Both bubble rise velocities, and bubble trajectories are governed by the bubble sizes. Therefore, accurate prediction of bubble size is required for reliable estimation of bubble column design parameters [41]. The factors influencing the bubble size are among others the gas density or operating pressure, surface tension of the liquid, viscosity of the liquid, operating conditions, and liquid impurities.

Gas density and operating pressure are closely related, since the operating pressure mainly influences the gas density. It has been found that bubble sizes decrease when the gas density increases. This can be explained by an increase of bubble breakage if the pressure increases due to the increase in gas density. The gas density increases by the larger inertia of the gas in the fluctuating bubble. In a bubble swarm, both coalescence and breakage influence the bubble size. Coalescence of bubbles is almost unaffected by pressure, but breakage increases, so the mean bubble size decreases with increasing pressure. For surface tension, the size of the bubbles decreases if surface tension decreases. Whereas if the viscosity increases, the bubble size increases. This is because when the liquid viscosity is increased, the turbulence of the liquid phase is reduced. As a result, the energy of eddies is reduced, and bubble breakage is damped. Hence, the bubble size increases. For the operating conditions, especially temperature and gas flow rate are important. Increasing the temperature leads to a decrease in stable bubble size. In turn, increasing the gas flow rate influences the bubble number density and hydrodynamics. With hydrodynamics, the gas holdup, bubble size and flow regime are considered [44]. As a result, the bubble collision frequency is increased, which leads to a higher coalescence rate, thus, an increase in bubble size. Lastly, impurities in the liquid can influence the bubble size by inhibition of coalescence, thus decreasing the bubble size [45].

The bubble size is frequently characterized with a single length scale, often the Sauter mean diameter (d_{32}) [46, 47, 48, 49, 50, 51]. The Sauter mean diameter is the average volume-surface mean diameter of the bubbles [48]. It expresses the mean diameter of poly-dispersed particulate matter by taking into account the volume-to-surface area. The resulting mean diameter is equal to the diameter of a system of identical spherical objects so that these spherical objects have identical total surface area, and identical total volume, but a different number of spherical objects than the original population of bubbles [49]. The Sauter mean diameter is determined by

$$d_{32} = \frac{\sum_{i=1}^{n} n_i d_i^3}{\sum_{i=1}^{n} n_i d_i^2} \quad . \tag{2.1}$$

Here n_i is the number of bubbles with size d_i.

2.1.1.3. Bubble Rise Velocity and Shape of Gas Bubbles in Liquid Medium

The motion of a rising or falling body in a liquid with its terminal velocity, v_T, is described by the balance between the buoyancy, F_B, and the drag, F_D, force [52]. The terminal rise velocity of a single bubble is defined as the velocity attained at steady state where all forces are balanced [43, 19]. The buoyancy, and drag force are described by Equations 2.2 and 2.3, respectively [52].

$$F_B = \Delta\rho V_b g \tag{2.2}$$

$$F_D = 0.5 C_D \rho_L v_T^2 A_b \tag{2.3}$$

where C_D is the drag coefficient, ρ_L is the liquid density, g the gravitational constant, V_b the volume of the bubble, and A_b the surface of projection on a horizontal plane of the bubble. From these two equations, it becomes evident that the terminal rise velocity of a single bubble rising in a liquid depends on the volume of the bubble and on the physical properties, like the viscosity and density, of the bubble and the liquid. Generally, the dynamics of a rising bubble are nonlinear, with the degree of non-linearity increasing with the bubble size. When surface tension dominates over the internal and buoyancy force, the bubbles are small and of spherical shape. The bubbles tend to retain their shape as long as their rising velocity remains small. However, in most practical situations, all three factors - inertia effect, viscosity, and surface tension, should be regarded, since the bubbles are not spherical and they move in an oscillatory manner [43].

Determining the bubble rise velocity does not require sophisticated techniques from an experimental point of view. However, due the complexity of a bubble rising in a liquid predicting the theoretical terminal velocity of the bubble is a rather complicated task that has been the subject of investigation for over a century. Generally, the bubble velocity is defined as

$$v = \frac{\sqrt{(x_{i+1} - x_i) + (y_{i+1} - y_i) + (z_{i+1} - z_i)}}{\Delta t} \tag{2.4}$$

where $(x_{i+1}, y_{i+1}, z_{i+1})$ and x_i, y_i, z_i are the coordinates of the subsequent positions in three directions of the bubble and Δt is the time interval. Experimentally, it is thus fairly easy to study the velocity using visual observation with a camera. For a theoretical prediction of the bubble rise velocity, multiple models have been proposed, from which a selection will be discussed here.
Often in theoretical studies the bubble equivalent diameter, d_e, is used to describe the size of the rising bubbles, since a bubble deforms as it moves through the liquid due to resistance of the continuous phase. The bubble equivalent diameter is defined as the diameter of the sphere with the same volume as the rising bubble. The real shape of the rising bubble can often be described with a good approximation as an oblate spheroid with horizontal, d_h, and vertical, d_v, diameters. The equivalent diameter can then be calculated as

$$d_e = (d_h^2 d_v)^{1/3} \tag{2.5}$$

[19, 43, 52]. The bubble shape can then be described using the bubble deformation degree, χ, defined as

$$\chi = \frac{d_h}{d_v} \quad . \tag{2.6}$$

Using Equation 2.2 and 2.3, the terminal velocity can then be expressed as

$$v_T = \left(\frac{4 d_b \Delta\rho g}{3 C_D \rho_L} \right)^{1/2} \quad . \tag{2.7}$$

Here the bubble equivalent diameter can be used as the bubble diameter, d_b, and $\Delta\rho = \rho_L - \rho_G$, with ρ_G the density of the gas. The drag coefficient proves to be the main problem when solving Equation 2.7 analytically. The drag coefficient depends on the conditions of the motion, and is often expressed as a function of the Reynolds number, Re.

$$Re = \frac{d_b v_T \rho_L}{\eta_L} \tag{2.8}$$

with η_L the dynamic viscosity of the liquid. The Reynolds number is a measure of the ratio between the inertial forces and the viscous drag [52]. For low Reynolds numbers, $Re \ll 1$, the viscous forces are large relative to internal terms. Viscosity thus dominates the terminal motion and the terminal rise velocity increases with an increase in bubble diameter. In this regime it is assumed that the bubble moves under creeping flow conditions. At intermediate Reynolds numbers, $Re > 1$, surface tension and inertia forces determine the bubble rise velocity. Additionally, bubbles are no longer spherical as their size increases, and the terminal velocity may increase, remain constant, or decrease with the diameter of the bubble. For $Re < 20$, it is assumed that a bubble moves as in the spherical regime, and for $20 < Re < 4700$ in the ellipsoidal regime. At high Reynolds numbers, $Re > 4700$, bubbles move under a spherical or ellipsoidal cap regime, and have thus a spherical cap or mushroom shape. The motion of the bubble is dominated by the inertia forces. In this region, the bubble rise velocity increases again with the increase of the equivalent diameter of the bubble [43, 52, 53].

Next to the Reynolds number, the Eotvos (Eo), Weber (We), and Morton (Mo) numbers are used to characterize the shape and terminal velocity of the bubble. The Eotvos number compares the importance of gravitational forces to surface tension forces, and is often used together with the Morton number to characterize the shape of the bubbles moving in the liquid. High Eotvos numbers indicate a dominance of buoyancy effects, while low Eotvos numbers indicate that surface tension is dominant over buoyancy. The Weber number relates the inertial forces to the surface tension forces. At low Weber number, $We \ll 1$, the bubble shape tends to be a spherical geometry. At $We \sim 1$, moderate deviations in the bubble shape occur. Often an oblate spheroid is observed. For high Weber numbers, $We \gg 1$, bubbles are easily deformed by the fluid acceleration at the gas-liquid interface. Therefore, the bubble shape experiences large distortions and often a spherical cap and oblate ellipsoidal cap are observed. The analytical expressions of these dimensionless numbers are provided in Equations 2.9, 2.10, and 2.11.

$$Eo = \frac{d_b^2 g \Delta\rho}{\sigma_L} \tag{2.9}$$

$$We = \frac{d_b v_T^2 \Delta\rho}{\sigma_L} \tag{2.10}$$

$$Mo = \frac{\eta_L^4 g \Delta\rho}{\rho_L^2 \sigma^3} \tag{2.11}$$

with σ_L the surface tension of the liquid [19, 43, 52]. Further dimensionless numbers that are often used are the Archimedes, Ar, and Lyshchenko, Ly, numbers

$$Ar = \frac{d_b^3 g \Delta\rho\rho_L}{\eta_L^2} \tag{2.12}$$

$$Ly = \frac{v_T^3 \rho_L^2}{g\Delta\rho\eta_L} \quad . \tag{2.13}$$

When determining the bubble rise velocity of a single bubble, two stages at the velocity profile can be distinguished. First there is an acceleration stage, where the local velocity increases monotonically. Secondly, there is a terminal stage when a constant value of the velocity is achieved. Depending on the bubble size after about 30-40 mm the velocity of the bubble starts to be constant [52].

Since the bubble rise velocity, v_b, is highly dependent on the bubble shape, but the bubble shape is again highly dependent on the bubble rise velocity, some kind of iterative scheme is needed to simultaneously determine both quantities. Therefore, Park et al. (2017) proposed a simple parameterization for the rise velocity for which the bubble shape does not need to be identified in advance. The proposed model for the bubble rise velocity of bubbles in a liquid pool is a combination of the velocity due to viscous force, the velocity due to inertial force, and the velocity for spheroidal bubbles.

$$v_b = \frac{1}{\sqrt{\frac{1}{v_{b,vis}^2} + \frac{1}{v_{b,in}^2} + \frac{1}{v_{b,speroid}^2}}} \tag{2.14}$$

where

$$v_{b,vis} = \frac{g(\rho_L - \rho_G)d_e^2}{6\eta_L}\left(\frac{1+\kappa}{2+3\kappa}\right) = \frac{g\rho_L d_e^2}{12\eta_L} \tag{2.15}$$

where $\kappa = \frac{\eta_G}{\eta_L} \approx 0$, since $\eta_G \ll \eta_L$ for most liquids and gases. Furthermore,

$$v_{b,in} = 0.14425 g^{5/6}\left(\frac{\rho_L}{\eta_L}\right)^{2/3} d_e^{3/2} \tag{2.16}$$

and

$$v_{b,spheroid} = \sqrt{\frac{2.14\sigma_L}{\rho_L d_e} + 0.505 g d_e} \quad . \tag{2.17}$$

If d_e is sufficiently large, $v_{b,spheroid}$ converges to

$$v_{b,speroid} = 0.711\sqrt{g d_e} \quad . \tag{2.18}$$

The bubble rise velocity can then be determined by Equation 2.19 [53].

$$v_b = \frac{1}{\sqrt{\frac{144\eta_L^2}{g\rho_L d_e^2} + \frac{\eta_L^{4/3}}{0.14425^2 g^{5/3}\rho_L^{4/3} d_e^3} + \frac{1}{\frac{2.14\sigma_L}{\rho_L d_e} + 0.505 g d_e}}} \tag{2.19}$$

Since the model of Park et al. (2017) includes a parameterization of the bubble rise velocity of bubbles in a liquid pool, no effect of a potential wall has been taken into account. However, in a bubble column the wall effects might influence the magnitude of the bubble terminal rise velocity. Particularly the effect of the wall becomes important for bubble-equivalent diameter to column diameter, D_T, ratios, $\lambda = \frac{d_e}{D_T}$, greater than or equal to 0.2 [19]. Therefore, Islam et al. (2013) looked at the influence of different geometries on the bubble rise velocity. They showed that the bubble velocity increases with bubble size and is affected by the shape of the column. They tested for both a rectangular, and a trapezoidal domain, and found that the bubble velocity is higher in a rectangular domain and lower in a trapezoidal domain. They proposed the following correlation for the bubble rise velocity

$$v_b = SF\left(\frac{2\sigma}{\rho_L d_b} + \frac{g d_b}{2}\right)^{1/2}, \quad SF = \left(1 - \left(\frac{d_b}{D_T}\right)^2\right)^{3/2} \tag{2.20}$$

with SF the scale factor, and again $d_b = d_e$ [54].

Next to the wall effects, bubbles in a bubble column might experience an additional acceleration due to the wake of the bubble preceding it. While the estimation of the rise velocity of a swarm of bubbles is reasonably well established if the bubbles are small, the estimation of the bubble rise velocity is much more uncertain if the bubbles are large. There are two empirical correlations for estimating the rise velocity of swarms of large bubbles, the first one proposed by Wilkinson et al. in 1992

$$\frac{v_b \eta_L}{\sigma} = 2.25\left(\frac{\sigma^3 \rho_L}{g\eta_L^4}\right)^{-0.273}\left(\frac{\rho_L}{\rho_G}\right)^{0.03} + 2.4\left(\frac{(U - U_{trans})\eta_L}{\sigma}\right)^{0.757}\left(\frac{\sigma^3 \rho_L}{g\eta_L^4}\right)^{-0.077}\left(\frac{\rho_L}{\rho_G}\right)^{0.077} \tag{2.21}$$

here U_{trans} is the superficial gas velocity at the point of transition from homogeneous to heterogeneous flow regime. The Wilkinson correlation does not include that the bubble rise velocity of large bubbles experience wall effects, and is thus column independent. Hence, Krishna and Ellenberger developed the correlation

$$V_b \equiv \frac{U - U_{trans}}{\epsilon_b} = D_T^{0.8}\frac{(U - U_{trans})^{0.42}}{0.268} \tag{2.22}$$

and found that the large bubble rise velocity is virtually independent of the properties of the liquid phase, but it increases significantly when increasing the column diameter. However this equation has some disadvantages, the extrapolation is not straightforward, and this correlation cannot be used when simulating bubble movement. Therefore, a correction factor was proposed to the existing Davies-Taylor relation

$$v_b^0 = 0.71\sqrt{g d_b}(SF) \tag{2.23}$$

for a single, isolated, bubble. For the scale factor, the empirical relations developed by

Collins in 1967 can be used

$$\begin{aligned} SF = 1 \quad & \frac{d_b}{D_T} < 0.125 \\ SF = 1.13e^{-\frac{d_b}{D_T}} \quad & 0.125 < \frac{d_b}{D_T} < 0.6 \\ SF = 0.496\sqrt{\frac{D_T}{d_b}} \quad & \frac{d_b}{D_T} > 0.6 \end{aligned} \tag{2.24}$$

For a swarm of large bubbles Equation 2.25 was proposed.

$$v_b = v_b^0(AF) \quad AF = \alpha + \beta(U - U_{trans}) \tag{2.25}$$

Here the acceleration factor, AF, increases linearly with decreasing distance of separation of the bubbles. Since for a large swarm of bubbles, each bubble is a trailing bubble [55].
Lastly, the terminal rise velocity could be influenced by contamination of the liquid. A correlation for the terminal velocity for contaminated liquids was proposed by Nguyen and Schulze in 2004 and Clift et al. in 1978. Both correlations have been adopted by Chavez et al. (2021), see Equation 2.26 (Nguyen) and 2.27 (Clift) [19].

$$V_{T,Nguyen} = 18U_{St}\left(\frac{4a^2Ar^{2b-1}Mo^{0.46b}}{3C_D}\right)^{\frac{1}{2-2b}} \tag{2.26}$$

$$v_{T,Clift} = \frac{\eta_L}{\rho_L d_b}Mo^{-0.149}(J - 0.857) \tag{2.27}$$

where

$$U_{St} = \frac{d_e^2 g \rho_L}{18\eta_L} \quad , \tag{2.28}$$

$$\begin{aligned} 12332 \leq Ar \leq 3.158Mo^{-0.46} \quad & a = 1,\ b = 0 \\ 3.158Mo^{-0.46} \leq Ar \leq 29.654Mo^{-0.46} \quad & a = 1.14,\ b = -0.176 \\ 29.654Mo^{-0.46} \leq Ar \leq 506.719Mo^{-0.46} \quad & a = 1.36,\ b = -0.280 \\ 506.719 \geq Ar \quad & a = 0.62,\ b = 0 \end{aligned} \tag{2.29}$$

and

$$\begin{aligned} J = 3.42H^{0.441} \quad & H > 59.3 \\ J = 0.94H^{0.757} \quad & 2 < H \leq 59.3 \\ J = ReMo^{0.149} + 0.857 \quad & \end{aligned} \tag{2.30}$$

with

$$H = \frac{4}{3}EoMo^{-0.149}\left(\frac{\eta_L}{\eta_W}\right)^{-0.14} \tag{2.31}$$

where η_W the viscosity of water in Braida's experiments, for which $0.0009\,Pa \cdot s$ was recommended [19].

2.1.1.4. Bubble Trajectories in Liquid Medium

The motion of a bubble is different than that of a solid particle rising due to buoyancy or sinking due to gravity. A solid particle can have the same shape as a bubble, however bubbles experience constant circulation internally. Additionally, a bubble tries to follow a path of least resistance during its motion. When the bubble rises upwards through the liquid, it experiences the most resistance directly on the top. But if the bubble would move slightly to one side, less total resistance is experienced. Therefore, it is often observed that bubbles commence a zigzag, helical, or spiral shaped path as they rise in a column of liquid [43].
It has been shown that a small bubble rises through water in a straight line at its terminal velocity until it finishes its journey. Larger bubbles do not have stable paths and zigzag, whereas even larger bubbles start to spiral. It is evident that with increasing bubble size, the bubble surface oscillations change from a simple oscillation to higher order modes. As a result the trajectory changes from a simple helix to more a complex path [43]. Additionally, the viscosity of the liquid medium the bubbles travel in, has an influence on the trajectory of the bubbles. When the viscosity increases, the zigzag path of big bubbles becomes tighter until they remain in a vertical line [56]. Nevertheless, a complete understanding of the dynamics of the bubble characteristic in a gas-liquid system is not yet available [43].

The bubble size distribution in a column is not constant, but may undergo constant change due to bubble-bubble interactions that can lead to breakage or coalescence of bubbles. In turn, interactions like clustering, collision, and merging affect the local and global characteristics of the liquid-phase flow [57]. The next section concerns the mechanisms behind bubble coalescence and breakup.

2.1.1.5. Bubble Coalescence and Breakup

Bubble coalescence occurs due to the rupture of the liquid film between adjacent bubbles [57]. When bubbles collide with each other, a thin liquid film is trapped between the bubbles. If this liquid is gradually drained out of the thin film by osmosis and the film thickness reaches the critical thickness, the film ruptures and the bubbles start to merge into a single bubble [39]. When two bubbles approach each other at a velocity v, the surfaces of the bubbles deform and become flatter when the distances between their surfaces, h, becomes small. The flattening occurs when the hydrodynamic pressure P_{hyd} at the film center exceeds the capillary pressure P_{cap} in the bubbles. When assuming no slip boundary conditions and spherical bubbles of radius R, $P_{hyd} > P_{cap}$ when h is smaller than a distance h^*, where $h^* \sim R\sqrt{\frac{\eta_L v}{\sigma}}$.

Kirkpatrick and Lockett introduced a mechanism of bubble-interface coalescence based upon the approach velocity of the bubble. They proposed that this mechanisms can be subdivided into three types, low, moderate, and large approach velocities. At low approach velocities the rate of increase of the contact film area between the bubbles is sufficiently slow so that the film is allowed to drain to the rupture thickness. At large approach velocities the rate of increase of the contact film area between the bubbles with time is sufficiently rapid to delay film thinning. This results in insufficient time for the contact film to drain to the rupture thickness before the bubble is brought to

rest. The motion of the bubbles tends to reverse because of the strain energy stored in the deformed bubbles. At moderate approach velocities, a transition region occurs between the small and large approach velocities regions. They found that if the approach velocity of the bubbles is less than about $12\ cm \cdot s^{-1}$, the bubbles would be expected to coalesce on first contact, whereas at higher approach velocities the bubbles are expected to bounce. Therefore, coalescence at large approach velocities is no longer a simple process, but depends on the oscillation of the bubbles after contact and the complex shape for the drainage film that is formed between the two interfaces [58].

Breakup of bubbles is caused by various processes. In a stagnant media, the interface between the two fluids experience Rayleigh-Taylor instabilities, leading to growing perturbations at the interface. The interface is in turn stabilized by surface tension, while viscous forces slow down the rate of growth of unstable surface waves. The surface of a bubble may therefore become unstable if the wavelength of a disturbance at the surface exceeds a critical value $\lambda_{cr} = 2\pi\sqrt{\frac{\sigma}{g\Delta\rho}}$. For rising bubbles, an instability manifests as an dent along the upper surface which grows deeper with time. If the disturbance grows sufficiently quickly relative to the velocity with which it is swept around to the equator by tangential movement along the interface, splitting tends to occur.

Another process by which breakup might occur is due to velocity gradients. A bubble in a shear field tends to rotate and deform. If the velocity gradients are large enough, interfacial tension forces can no longer maintain the fluid particle, result in a rupture of one large bubble into two or more smaller bubbles [59].

2.2. Particle Separation in Bubble Column

A technique that uses a bubble column to separate insoluble particles from water is known as flotation. Flotation is a widely used cost-effective separation technique that is utilized in, among others, wastewater treatment, mineral benefication, microoxygenation of wine, fermentation, ink removal, and plastic recycling [60]. Particle flotation is especially successful for a particle size range of about $15 - 150\ \mu m$ [61]. However, the flotation of fine particles and its limits has been under investigation for many years. Key parameters for fine particle flotation have been identified as bubble size, particle aggregation, and flow conditions [61]. In the next sections, the limits of fine particle flotation, and key events in bubble-particle behavior are reviewed.

2.2.1. The Limits of Fine Particle Flotation

To predict the rate constant of flotation kinetics, the various microprocesses that occur during collection of solid particles by air bubbles, need to be understood. The microprocesses that occur during flotation are collision, attachment, and detachment. Unlike collision, both attachment and detachment are dependent on the chemistry and physical chemistry of the surface of solid particle and bubble [62]. The rate constant is

then defined as

$$k = F_c \cdot E_c \cdot E_a \cdot E_d \quad , \tag{2.32}$$

where F_c is the collision frequency, E_c the collision probability, E_a the attachment probability, and E_d the detachment probability [61]. There are two main types of particle-bubble attachment models, namely the kinetic and thermodynamic models. In the kinetic model, attachment occurs if the sliding time of the particle on a bubble surface is larger than or equal to the induction time, which will be explained in the next section. In the thermodynamic models, attachment only occurs if the kinetic energy of the particle that approaches the bubble is larger than the energy needed to disrupt the intervening liquid film and form a stable three-phase contact line. The Particle-bubble detachment models that have been developed only apply to coarse particles, and are based on a force balance which is mostly affected by gravity and external acceleration [61]. Therefore, in the next section only collision and attachment models will be examined.

2.2.1.1. Particle Collision and Attachment Models

Before bubble-particle attachment can occur, the particle needs to collide with a bubble, and reach a distance at which surface forces start to operate. Bubble-particle collision models are based on an evaluation of the forces that cause a particle to deviate in its trajectory from fluid streamlines near the bubble surface and collide with the bubble. The forces that affect the particle motion include gravitational-, inertial-, and hydrodynamic drag forces. Additionally, bubble-particle collision models based on diffusion and shear have also been defined. From these models, the models based on shear are usually not considered, since shear-induced mechanisms are only significant for collision of spheres with equal size.

Coarse and dense particles are unable to follow fluid streamlines and tend to move along a straight path. Therefore, these particles collide with bubbles based on an inertial mechanism. The particles may collide with bubbles because of a deviation of their trajectory from fluid streamlines due to a certain settling velocity caused by a higher density of the particles compared to the fluid. Another mechanism for collision is by interception. Bubble-particle collision by interception occurs when particles are carried along the fluid streamlines due to flow patterns and the particles come into contact with the bubble due to finite size. Lastly, bubble-particle collision models based on Brownian diffusion are only significant for submicron particles, since they move randomly in the fluid.

Mainly, the inertial forces and the long range hydrodynamic interaction, or LRHI, due to drag govern the mechanism of transfer of small particles to the bubble surface. Where for large particles inertial forces dominate, for small particles, especially if the density of the particles is close to the density of the fluid, the LRHI changes the trajectory of the particle to coincide with the fluid streamlines. Equation 2.33 represents the Stokes number, which describes the ratio of the stopping distance of the particle in the presence of the LRHI to a characteristic dimension.

$$St = \frac{\rho_p v_b d_p^2}{9 d_b \eta_L} \tag{2.33}$$

Here, ρ_p and d_p are the density and diameter of the particle, respectively. If $St \ll 1$ inertial forces have practically no effect on the motion of the particles. The motion can therefore be considered inertia-free. If $St \leq 0.1$ negative inertial forces can impede particle deposition on a bubble. For $0.1 < St < 1$ an inelastic inertial impact of particles occurs on a bubble surface. Additionally, a major portion of the kinetic energy of the particles is lost during the approach of the particle to the bubble and at the impact itself, when a liquid layer is formed between the surfaces of the particles and the bubbles. Lastly, if $St > 3$, the trajectory of the particle deviates slightly from a straight line, and the collision between bubble and particle can be considered quasi-elastic since the energy of the particles changes so little. As a result, the particle bounces away from the bubble surface at almost the same speed as it approaches the bubble surface.

Two of the best known collision models are the Stokes flow model and the potential flow model. The Stokes flow model holds for Reynolds numbers significantly smaller than unity. A Stokes flow regime is assumed to be around the bubble surface, and inertial forces on the particles are ignored. The Stokes flow bubble-particle collision model is described by

$$E_{C-St} = \frac{3}{2}\left(\frac{d_p}{d_b}\right)^2 \quad . \tag{2.34}$$

The potential flow model includes Brownian motion and its effect on bubble-particle collision. It applies to Reynolds numbers based on the bubble velocity between 80 and 500, and particle sizes larger than 0.1 μm [63].

$$E_{C-pot} = \frac{3d_p}{d_b} \tag{2.35}$$

There are three key steps in particle-bubble attachment. Firstly, the thinning of the intervening liquid film to the rupture thickness called the critical thickness, secondly the rupture of the intervening liquid film and the formation of a three-phase contact nucleus, and lastly the expansion of three-phase contact line from the critical radius to form a stable wetting perimeter [62, 63, 64].

During the first step various forces operate between the bubble and the particle. The surface forces act on the radial direction along the inter-center line and are the most characteristic. In addition, the drag force, and especially the steady drag force in the radial direction, is important since it resists the motion of the particle towards the bubble surface. Furthermore, gravitational and buoyancy forces act on the particle [64]. Generally, bubble-particle attachment models are described in terms of the contact- and induction time. Additionally, the bubble-particle attachment can also be modeled using the energy barrier approach. Here, for bubble-particle attachment, the kinetic energy of a particle has to be higher than an energy barrier between the particle and the bubble surface.

The induction time is the time required for the thinning of the intervening liquid film between the particle and bubble, the film rupture, and the resulting formation of a stable three-phase contact line. Generally, the formation of the three-phase contact line has been assumed to be very short. Furthermore, the time of film rupture is of the order of magnitude 10^{-9} s, so the thinning of the intervening liquid film is considered to be the dominant factor of induction time. Experimental results indicate that

induction time increases with increasing particle size and decreasing particle surface hydrophobicity. The relation between induction time and particle diameter is suggested to follow a power function [63].

The contact time represents the time for which a particle and a bubble are in contact after their collision. The contact time consists of the impact time and the sliding time. When a particle and a bubble collide, either the particle bounces off of the bubble, in this case only the impact time influences the contact time, or the particle slides along the bubble surface, for which both the impact time and the sliding time influence the contact time. Because rebound is only possible if the bubble surface deforms, particles with a diameter less than $100\ \mu m$ only impact and slide on the bubble surface since their kinetic energy is too small to distort the bubble surface. Typically, the contact time is maximally $10\ ms$ [63].

A simple model for the probability of attachment was developed by Dobby and Finch in 1990. According to them, the attachment probability can be determined by

$$P_{at} = \left(\frac{sin(\phi_{cr})}{sin(\phi_c)} \right)^2 \quad . \tag{2.36}$$

Here ϕ_{cr} represents the angle beyond which no attachment occurs, and ϕ_c the angle beyond which no collision occurs [63, 62]. Additionally, Nguyen, Ralston and Schulze suggested that the probability of attachment can be described as $P_{at} = P_f P_r P_{tpc}$, with P_f the probability of thinning of the liquid film to the critical thickness, P_r the probability of rupture of the intervening film, and P_{tpc} the probability of expansion of three-phase contact line. For fine particles, it has been shown that P_{tpc} is almost equal to unity. Determination of these probabilities is not a straightforward process, and more deeper experimental and theoretical investigations of the elementary steps in bubble-particle attachment needs to be performed [62].

The low recovery of fine particle flotation is often attributed to the low particle bubble collision efficiency [63, 61]. Several strategies have been proposed to increase fine particle flotation. These include aggregation of particles, or decreasing the bubble size [61]. However, another mechanism occurs simultaneously along flotation, namely entrainment, that increases the recovery of fine particles. Entrainment will be the subject of the next section.

2.2.1.2. Entrainment

Mechanical entrainment is a process by which particles move upwards. It is not chemically selective and it occurs without a direct attachment of particles to bubbles. Therefore, entrainment plays especially a role in fine particle flotation. Three mechanisms have been proposed to characterize particles traveling in a flotation cell by entrainment. These three mechanisms are denoted the Boundary Layer Theory (BLT), the Bubble Wake Theory (BWT), and the Bubble Swarm Theory (BST). In the Boundary Layer Theory, the particles are transported in the thin hydrodynamic layer of water surrounding the bubble, called the bubble lamella. In the Bubble Wake Theory, the particles are transported along with water in the wake of an ascending bubble, see Figure 2.2.1. Next to the boundary layer and the bubble wake, an additional theory

was proposed by Smith and Warren in 1989 for particle transport [65]. However, the Bubble Swarm Theory is limited to a conventional flotation setup, and is outside of the scope of this master thesis.

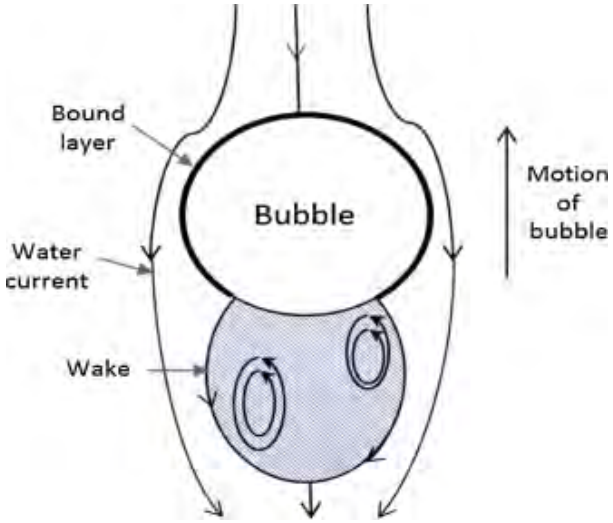

Figure 2.2.1: Schematic of Boundary Layer Theory and Bubble Wake Theory. Figure adopted by Wang et al. 2015 [65].

The particle size is one of the parameters with a profound effect on entrainment. The recovery of hydrophilic minerals by entrainment increases significantly with decreasing particle size, see Figure 2.2.2. Generally, mineral particles with a size under $50\,\mu m$ are known to be recovered by entrainment more easily than larger particles. Additionally, particle density is also a factor affecting entrainment. The higher entrainment of low-density particles can be associated with the fact that low-density particles tend to move with the water due to their low sedimentation velocities. Whereas particles with higher density settle more quickly and have less chance to be transported upwards. This sedimentation rate can be explained by using Stokes' law [65]. The particles sinking through the column under the influence of gravity experience a drag force that resist against their fall through the fluid medium. The drag force, acting upwards is expressed by $F_D = 6\pi r\eta v$, and the gravitational force acting downward is equal to $F_g = \frac{4}{3}\pi r^3(\rho_p - \rho_L)g$. Here, r is the radius of the particle, η the viscosity of the liquid, v the velocity of fall, ρ_p the density of the particle, ρ_L the density of the liquid, and g the acceleration due to gravity. At a constant terminal fall velocity, the drag force and gravitational force are in balance. We can therefore express the fall velocity as

$$v = \frac{2}{9}\frac{(\rho_p - \rho_L)gr^2}{\eta} \quad . \tag{2.37}$$

Stokes' law is applicable in situations where the motion of the particle does not produce turbulence in the fluid [66].

Next to particle behavior, bubble size and velocity might have an impact on entrainment [67]. The particle velocity induced by the bubbles can be measured using Laser Doppler Anemometry, or LDA. In short, LDA utilizes the Doppler shift in a laser beam to calculate the velocity of tracer particles in a transparent or semi-transparent fluid [68]. The physical concept of LDA will be the subject of the next section.

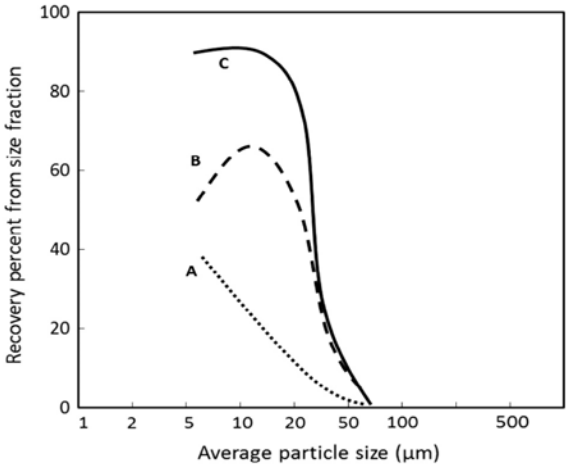

Figure 2.2.2: Recovery of siderite as a function of the average particle size. A: Recovery by entrainment, B: recovery by true flotation, C: Recovery by entrainment and true flotation. Figure adopted by Wang et al. (2015) [65].

2.3. Laser Doppler Anemometry

The LDA technique is one of the most widely used techniques for point velocity and turbulence measurements in gas or liquid flows [69]. The technique is based on the principle of the Doppler shift. The Doppler shift is a change in frequency due to the relative motion of the source. If a wave is emitted by a source, the waves spread out spherically from the point at which the wave is emitted. For a stationary source, the center of the spherical wave is at the same point, and the stationary observers on all sides of the source receive the wave with equal wavelength and frequency as emitted by the source. However, if the source is moving, the source does not emit waves from the same location. In contrast to a stationary source, for a moving source the waves are emitted from a different location each time. In the direction of the movement, the wave is then compressed, whereas in the opposite direction, the wave is elongated. Therefore, the wavelength in the same direction as the source is moving is shorter, whereas in the opposite direction the wavelength is longer than the original wavelength emitted by the source [70]. The frequency change size is dependent on the velocity and the scattering geometry of the moving source, and is given by the following equation

$$\Delta v = (k_s - k_0)v_s \tag{2.38}$$

here $k_0 = \frac{2\pi}{\lambda}$ is the incident wave vector, λ the wavelength of the incident radiation, k_s the scattered wave vector, v_s the velocity of the scatterer, and Δv the Doppler shift.

The LDA has a laser source that is split into two equal parts by a simple beam splitter. The point where the two beams cross, together with the aperture (field stop) on the face of the detector, define the region from which measurements can be obtained. The beam splitter can be adjusted by both rotation and translation to adjust the crossing point and the angle of intersection of the beams. Often, a Bragg cell is used as a beam splitter. A Bragg cell is a glass crystal with a vibrating piezo crystal attached. The vibration generates acoustical waves acting like an optical grid. The output of the

Bragg cell is then two beams of equal intensities, with frequency f_0 and f_{shift}. The two beams are focused into optical fibres bringing them to a probe. In the probe, the parallel exit beams are focused at the point of intersection, by inserting a simple lens paraxially to the laser. The probe volume is typically a few millimeters long, where the light intensity is modulated due to interference between the laser beams. Planes of high light intensity, called fringes, are then produced, from which the fringe distance, d_f, can be defined. The particles that pass the beam will scatter the light of the laser beam. The scattered light contains a Doppler shift, or the Doppler frequency, which is proportional to the velocity component that is perpendicular to the bisector of the two laser beams. The fringe distance can then be calculated as

$$u = d_f f_D = \frac{\lambda}{2sin(\Theta/2)} f_D \quad . \tag{2.39}$$

Here Θ is the angle between the two beams, λ the wavelength of the laser light, and f_D the Doppler frequency. The scattered light is then received and focused on the photo-detector. The photo-detector converts the fluctuating light intensity to an electrical signal, called the Doppler burst. The Doppler burst is sinusoidal with a Gaussian envelope due to the intensity profile of the lasers. A large-aperture lens collects the received data. The data is then filtered and amplified in the signal processor, which determines the Doppler frequency for each particle. From the Doppler frequency, the fringe distance is calculated, which determines the distance traveled by the particle. From the Doppler frequency, the time of the movement can be calculated. Using the distance and the time, the velocity of the particle can in turn be calculated. To measure the velocity in multiple directions extra beams can be added in a plane perpendicular to the first beams, which can be measured by addition of additional probes and interference filters. Since LDA is dependent on the quality of the measurement of the received scattered light, it is particularly well suited to flows in which the density of scattering particles is low. Furthermore, the particles should be small enough to be affected by the flow, but large enough to scatter sufficient light to obtain a good signal-to-noise ratio at the photo-detector output. The typical size range of adequate particles is between $1\,\mu m$ and $10\,\mu m$ [71, 72].

The advantages of LDA are that it is a non-intrusive technique, so it does not affect the flow patterns of the fluid, no drift and no calibration are needed, the directional response is well-defined, the temporal and spatial resolution are high, and it enables multi-component bi-directional measurements [68].

When obtaining datasets from the LDA, it is useful to find a correlation between the data. Consequently, multiple statistical theories have been invented. Some relevant statistical theories, are discussed in the next sections.

2.4. Useful Statistical Theories

In statistics, techniques used to make decision about the parameters of a population are based on parametric or non-parametric methods. Which kind of test can be used, depends on the type of measurement of the data. To this end there are four measurement scales. The weakest scale is the nominal or categorical scale, which is used to

classify a number to an object, person, characteristic, etc. One scale higher is the ordinal or ranking scale, where a number is used for objects that have some kind of ranked relation to other objects. The third scale is the interval scale. Here a number is used for objects that have some kind of ranked relation to other objects, and the differences between numbers have meaning. The highest scale is the ratio scale, where a number is used for objects that have some kind of ranked relation to other objects, the differences between numbers have meaning, and there is a true zero point at its origin.

In general, four assumptions must hold to properly conduct a parametric test. Firstly, the observations need to be independent. Secondly, the observations must be drawn from a normally distributed population. Thirdly, the variance of the different groups need to be equal. And lastly, variables must be measured in an 'interval' or higher scale in order to interpret results. For non-parametric tests only two assumptions are needed: the observations need to be independent, and sometimes data is drawn from an underlying continuous distribution. The advantages of a non-parametric test over a parametric test is that very small sample sizes can be used, variables do not need to be measured in an 'interval scale', but can also be measured in other scales, and outliers have less impact. However, when the assumptions are met, a parametric test is preferred over a non-parametric test, since they have more 'power' [73]. In statistical tests, often a null hypothesis, H_0, and a research, or the alternative, hypothesis, H_1, are proposed. The null hypothesis is what we accept as true unless we have compelling evidence that it is not true. The research hypothesis is what we accept as true whenever we reject the null hypothesis as true. Since it is not possible for both the null hypothesis as the research hypothesis to be true, the task of hypothesis testing using statistical formulas is to decide which one will be accepted as true, and which one will be rejected [74]. In the following sections, some parametric and non-parametric tests based on null- and research hypotheses are considered.

2.4.1. Levene's test

To test the homogeneity of variances, Levene's test can be employed as a measure of the degree to which sample variances vary. If the sample variances do not differ too much, it is a reasonable assumption that the population variances are equal. The problem considered in Levene's test is the testing of the equality of variances of I populations given samples $x_{ij} : j = 1, ..., n_i$ from the ith population with mean μ_i, variance σ_i^2, and distribution function $F\{\sigma_i^{-1}(x - \mu_i)\}(i = 1, ..., I)$. The function F, and the constants μ_i, and σ_i are unknown. The proposed null hyopthesis is then

$$H_0 : \quad \sigma_1^2 = \sigma_2^2 = ... = \sigma_I^2$$

and the alternative hypothesis is

$$H_1 : \quad \sigma_i^2 \neq \sigma_j^2 \; for \; at \; least \; one \; i \neq j.$$

The group mean is defined as $\overline{x}_i = \sum_{j=1}^{n_i} \frac{x_{ij}}{n_i}$, the group variance is $s_i^2 = \sum_{j=1}^{n_i} \left(\frac{(x_{ij} - \overline{x}_i)^2}{n_i - 1} \right)$, and the total sample size $N = \sum_{i=1}^{I} n_i$. We can then define $z_{ij} = |x_{ij} - \tilde{x}_i|$, where $\tilde{x}_i$ is

the median of $\{x_{ij} : j = 1, ..., n_i\}$. The test statistic of Levene's test is

$$L = \frac{\sum_{i=1}^{I} \frac{n_i(\overline{z}_{i.} - \overline{z}_{..})^2}{I-1}}{\sum_{i=1}^{I} \sum_{j=1}^{n_i} \frac{(z_{ij} - \overline{z_{i.}})^2}{N-I}} \tag{2.40}$$

with

$$\overline{z_{i.}} = \sum_{j=1}^{n_i} \frac{z_{ij}}{n_i}$$

and

$$\overline{z_{..}} = \sum_{i=1}^{I} \sum_{j=1}^{n_i} \frac{z_{ij}}{N}$$

The null hypothesis is rejected when the $p - value$ is less than the nominal level α.

Levene's test has been proven to be robust and of high power. However, Lim and Loh 1996 suggested that when using Levene's test it is highly desirable to have a balanced design with large sample sizes to achieve good power [75].

2.4.2. Two sample t-test

The t-test is a test for the hypothesis of equal means. It assumes that the underlying distribution of the variable of interest is normally distributed [76]. Using the t-test, it is possible to determine whether there is a significant difference in the mean and variance between two groups. The two-sample t-test (for two independent groups) and the paired t-test (for matched samples) are the most widely used methods for the comparison of two samples [77]. There are two well-known versions of the two-sample t-test,- Student's t-test and Welch's t-test [78]. Welch's t-test is the non-parametric equivalent of the parametric Student's t-test. In the Student's t-test, let two samples x_{ij} and x_{ik} be statistically independent if $j \neq k$. The sample means and sample variances of these two samples are then

$$\overline{x}_i = \frac{1}{n_i} \sum_{j=1}^{n_i} x_j$$

$$s_i^2 = \frac{1}{n_i - 1} \sum_{j=1}^{n_i} (x_j - \overline{x}_i)^2$$

where $i = 0, 1$. If $\overline{x}_d = \overline{x}_1 - \overline{x}_0$ is the difference of the sample mean values, the mean and the variance of $\overline{x}_d$ are then as described in equations 2.41 and 2.42

$$E(\overline{x}_d) = \mu_1 - \mu_0 \tag{2.41}$$

$$V(\overline{x}_d) = \frac{\sigma_0^2}{n_0} + \frac{\sigma_1^2}{n_1} \tag{2.42}$$

The variance of $\overline{X}_d$ can be estimated by a simple moment estimator:

$$s_d^2 = \frac{s_0^2}{n_0} + \frac{s_1^2}{n_1}$$

If the variance of the two samples are the same, i.e. $\sigma_0^2 = \sigma_1^2$, we can rewrite the simple moment estimator more efficiently to equation 2.43.

$$s_d^2 = \left(\frac{1}{n_0} + \frac{1}{n_1}\right) \frac{(n_0 - 1)s_0^2 + (n_1 - 1)s_1^2}{n_0 + n_1 - 2} \tag{2.43}$$

If we then want to test the hypothesis that the velocities have the same mean values, i.e., $H_0 : \mu_0 = \mu_1$ we use a t-test of the form $\frac{sample\ mean\ difference}{sample\ standard\ deviation\ of\ the\ sample\ mean\ difference}$. For the two-sample t-test we then obtain equation 2.44.

$$T_1 = \frac{x_d}{\sqrt{\left(\frac{1}{n_0} + \frac{1}{n_1}\right)\frac{(n_0-1)s_0^2+(n_1-1)s_1^2}{n_0+n_1-2}}} \tag{2.44}$$

Under the null hypothesis, H_0, if $\sigma_0 = \sigma_1$, T_1 follows the t-distribution with degrees of freedom n_0+n_1-2. If $\sigma_0 \neq \sigma_1$, the distribution of T_1 is described by the Behrens-Fisher problem in statistics, which is out of the scope of this thesis [77].

It is often recommended to use Student's t-test when the sample sizes are similar, or if the variances of the samples are similar. If both of these conditions are violated, it is recommended to use Welch's t-test. For Welch's t-test, let $V_1 = \frac{S_1}{\phi_1}$, $V_2 = \frac{S_2}{\phi_2}$. The test statistic is

$$t_{w0} = \frac{\overline{x}_1 - \overline{x}_2}{\sqrt{\frac{V_1}{n_1} + \frac{V_2}{n_2)}}} \quad , \tag{2.45}$$

which is compared against $t(\phi^*; \alpha)$, where

$$\phi^* = \frac{\left(\frac{V_1}{n_1} + \frac{V_2}{n_2}\right)^2}{\left(\frac{(V_1/n_1)^2}{\phi_1} + \frac{(V_2/n_2)^2}{\phi_2}\right)} \quad . \tag{2.46}$$

The approximation is then made that Equation 2.46 can be approximated by a χ^2 distribution with ϕ_0 degrees of freedom, as shown in Equation 2.47.

$$W = \frac{\phi_0\left(\frac{V_1}{n_1} + \frac{V_2}{n_2}\right)}{\left(\frac{\sigma_1^2}{n_1^2} + \frac{\sigma_2^2}{n_2}\right)} \tag{2.47}$$

In both the Student's t-test as the Welch's t-test, a p-value can be obtained from the t-distribution with degrees of freedom df. The p-value is compared to a preset standard, α, that determines whether the null hypothesis is false or not [79].

2.4.3. ANOVA test

When dealing with more than two groups, a common test to test for differences between the groups is the Analysis of Variances (ANOVA) test. ANOVA is a parametric test, and therefore normality, independence, and equal variance of the samples must be satisfied. When performing ANOVA a minimum sample size of 30 is desired,

but the group numbers do not need to be equal. A one-way ANOVA compares the means of two or more groups for one dependent variable. ANOVA compares the variation within a group to the equivalent variation based on all group means' variation. Consider k random samples $x_1, x_2, ..., x_k$, where the i^{th} sample $\mathbf{x}_i = (x_{i1}, x_{i2}, ..., x_{in_i})$, $i = 1, 2, ..., k$. is coming from distribution $N(\mu_i, \sigma^2)$. Here N is defined as $N = \sum_{i=1}^{k} n_i$, and $\overline{x}_i$ as $\overline{x}_i = \frac{1}{n_i}\sum_{j=1}^{n_i} x_{ij}$. Furthermore, we define $\overline{x}_w = \frac{1}{N}\sum_{i=1}^{k} n_i\overline{x}_i$, and $S_{\mathbf{x}}^2 = \sum_{i=1}^{k}\sum_{j=1}^{n_i}(x_{ij} - \overline{x}_i)^2$. The null hypothesis can then be defined as

$$H_0: \quad \mu_1 = \mu_2 = \mu_3 = ... = \mu_n$$

with the alternative hypothesis

$$H_1 : At\, least\, one\, inequality\, in\, H_0 \quad .$$

ANOVA uses a F distribution as the reference distribution. The ANOVA F distribution is formed by the variance ratios, and can be expressed as

$$F = \frac{Intergroup\, variance}{Intragroup\, variance} = \frac{\sum_{i=1}^{K} \frac{n_i(\overline{Y}_I - \overline{Y})^2}{K-1}}{\sum_{ij=1}^{n} \frac{(Y_{ij} - \overline{Y}_i)^2}{N-K}} \quad .$$

Here, $\overline{Y_i}$ is the mean of the group, n_i the number of observations of the group i, $\overline{Y}$ the overall mean, K the number of groups, Y_{ij} the $j'th$ observational value of group i, and N the number of observational values.

Based on the original data $\mathbf{x} = (\mathbf{x}_1, \mathbf{x}_2, ..., \mathbf{x}_k)$, the likelihood ratio test (LRT) is provided by the standard F-statistic. The F-statistic is defined as

$$F_x = \left(\frac{N-k}{k-1}\right)\frac{BSS}{WSS}$$

where $BSS = \sum_{i=1}^{k} n_i(\overline{x}_i - \overline{x}_w)2$ and $WSS = S_x^2$.
From the F-statistic a p-value can in turn be extracted. As with the tests mentioned above, the null hypothesis is rejected when the p-value is less than the nominal level α [80, 81].

2.4.4. Kruskal-Wallis test

When the means of k populations are compared and it is known that the populations do not have equal variances, the Kruskal-Wallis test can be used as a substitute for ANOVA. The Kruskal-Wallis test assumes that the observations in each group originate from populations with the shape of a normal distribution and that the samples are random and independent. Let us assume that the data $x_{11}, x_{12}, ..., x_{1n_1}$ are a sample from population 1, $x_{21}, x_{22}, ..., x_{2n_2}$ a sample from population 2, and $x_{k1}, x_{k2}, ..., x_{kn_k}$ a sample from population k. x_{ij} with $i = 1, 2, ...k$ and $j = 1, 2, ..., n_i$ denote the data from the i^{th} group (level) and j^{th} observation. Furthermore, $F_i(x)$ is defined as the continuous distributions of x_{ij}. We also assume that the independent random samples have sizes $n_1, n_2, ..., n_k$, and are drawn from k continuous, not necessarily normal, populations. We can then define the null hypothesis as

$$H_0: \quad F_1(x) = F_2(x) = ... = F_k(x)$$

for all x. In words, this states that the distributions for all k populations are the same. The alternative hypothesis is then

$$H_1: \quad \exists 1 \leq i, l \leq k : F_i(x) \neq F_l(x) \quad ,$$

i.e., at least two population distributions differ in location.

We can then assign ranks to the observations by ranking all observations $N = \sum_{i=1}^{k} n_i$ from smallest to largest without regard to which sample they originated from. The smallest observation is ranked 1, the next 2, up until rank N for the largest observation. We call the rank of the observation x_{ij}, R_{ij} and we define R_i to be the sum of the ranks in the i^{th} sample. So that $R_i = \sum_{j=1}^{n_i} R_{ij}$, and denote the sample each sample mean by $\overline{R}_i \frac{R_i}{n_i}$. We represent the overall mean by $\overline{R}$. Since we know $\sum_{i=1}^{k} R_i = \frac{N(N+1)}{2}$, we conclude $\overline{R} = \frac{\sum_{i=1}^{k} R_i}{N} = \frac{N+1}{2}$. The Kruskal-Wallis test determines the degree to which the actual observed mean ranks $\overline{R}_i$ differ from their expected value $\frac{N+1}{2}$. If the difference is large, we can reject the null hypothesis [82].

2.5. Computational Fluid Dynamics Modeling

The complexity of the bubble motion, and bubble-particle interactions make it a very difficult process to study analytically. Therefore, in recent years with the enhancement of numerical algorithm and computing power computational fluid dynamics (CFD) has proven to be a useful tool to obtain a better physical understanding of flow problems encountered in a bubble column [54]. In the next sections, some models used in CFD modeling are covered. Since in this thesis Ansys Fluent was used as a CFD modeling software, the discussed theories are applied to Ansys Fluent. However, the basis of the different models is often universal and thus other software might have a similar basis.

2.5.1. Basis of CFD Modeling

For all kinds of flows the basis of CFD modeling lies in solving for equations for mass and momentum. The equation for the conservation of mass, also called the continuity equation can be described as follows

$$\frac{\partial \rho}{\partial t} + \nabla \cdot (\rho \vec{v}) = S_m \quad . \tag{2.48}$$

Equation 2.48 deviates from the Navier-Stokes equations due to the parameter S_m. This parameter is added as a source term of the mass added to the continuous phase from the dispersed second phase. The conservation of momentum is described by

$$\frac{\partial}{\partial t}(\rho \vec{v}) + \nabla \cdot (\rho \vec{v} \vec{v}) = -\nabla \mathbf{p} + \nabla \cdot \overleftrightarrow{\tau} + \rho \vec{g} + \vec{F} \quad . \tag{2.49}$$

Here $\mathbf{p}$ is the static pressure, $\rho \vec{g}$ and $\vec{F}$ the gravitational and external body forces, and $\overleftrightarrow{\tau}$ the stress tensor described by

$$\overleftrightarrow{\tau} = \eta \left[(\nabla \vec{v} + \nabla \vec{v}^T) - \frac{2}{3} \nabla \cdot \vec{v} I \right] \tag{2.50}$$

with η the molecular viscosity, I the unit tensor, and second term on the right hand side describes the effect of volume dilatation [83].

Modeling of flotation requires the modeling of a mixture of phases. Subsequently, CFD deals with the concept of multiphase flows. In multiphase flow a phase can be defined as an identifiable class of material with a particular inertial response to and interaction with the flow and potential field in which it is immersed. For example, different sized solid particles of the same material can be treated as different phases because a collection of the particles with the same size will have a similar dynamical response to the flow field [84].

2.5.2. Multiphase Models using the Euler-Euler Approach

Currently, two approaches exist for the numerical calculation of multiphase flows: the Euler-Lagrange approach, and the Euler-Euler approach. In the Euler-Euler approach, the different phases are treated mathematically as interpenetrating continua. The volume of a phase cannot be occupied by the other phases, therefore, the concept of phasic volume fraction is introduced. These volume fractions are assumed to be continuous functions of space and time, with their sum being equal to one. For each phase conservation equations are derived to obtain a set of equations with similar structure for all phases. The equations are closed by providing constitutive relations that are obtained from empirical information, or by application of kinetic theory for granular flows [84]. In the next sections, different models based on the Euler-Euler approach will be highlighted, since the Euler-Lagrange models are outside the scope of this thesis.

2.5.2.1. Volume of Fluid Model

The Volume of Fluid, VOF, model is a surface-tracking technique applied to a fixed Eulerian mesh, i.e., the mesh does not change as the material flows inside the mesh. The VOF model uses a single set of momentum equation shared by all fluids, and a volume fraction of each of the fluids is tracked throughout the domain in each computational cell. The tracking of the interfaces between the different phases is accomplished by the continuity equation for the volume fraction of the phases. For the q^{th} phase, the equation has the following form

$$\frac{1}{\rho_q}\left(\frac{\partial}{\partial t}(\alpha_q\rho_q) + \nabla\cdot(\alpha_q\rho_q\vec{v}_q) = S_{\alpha_q} + \sum_{p=1}^{n}(\dot{m}_{pq} - \dot{m}_{qp})\right) \tag{2.51}$$

where $\dot{m}_{qp}$ and $\dot{m}_{pq}$ are the mass transfer from phase q to p and p to q respectively. The volume fraction of the primary phase will be computed based on the constraint that $\sum_{q=1}^{n}\alpha_q = 1$. To solve the volume fraction equation, either an implicit or explicit time discretization can be used. An implicit scheme requires the volume fraction values at the current time step. Furthermore, a standard scalar transport equation is solved iteratively at each time step for each of the secondary-phase volume fractions.

$$\frac{\alpha_q^{n+1}\rho_q^{n+1} - \alpha_q^n\rho_q^n}{\Delta t}V + \sum_f(\rho_q^{n+1}U_f^{n+1}\alpha_{q,f}^{n+1}) = \left[S_{\alpha_q} + \sum_{p=1}^{n}(\dot{m}_{pq} - \dot{m}_{qp})\right]V \tag{2.52}$$

In the explicit approach, standard finite difference interpolation schemes are applied to the volume fraction values that were computed at the previous time step.

$$\frac{\alpha_q^{n+1}\rho_q^{n+1} - \alpha_q^n \rho_q^n}{\Delta t} V + \sum_f (\rho_q U_f^n \alpha_{q,f}^n) = \left[\sum_{p=1}^{n} (\dot{m}_{pq} - \dot{m}_{qp}) + S_{\alpha_q} \right] V \quad . \tag{2.53}$$

Here $n+1$ denotes the index for a new (current) time step, n the previous time step, $\alpha_{q,f}$ the face value of the q^{th} volume fraction, V the volume of the cell, and U_f the volume flux through the face, based on the normal velocity.

The explicit scheme does not require iterative solution of the transport equation during each time step, however it does require a time-dependent solution.

In the VOF model a single momentum equation is solved throughout the domain, see Equation 2.49. Where in Equation 2.50 the term $\frac{2}{3}\nabla \cdot \vec{v}I$ is neglected. The resulting velocity field is shared among all phases. The VOF model is designed for two or more immiscible fluids where the position of the interface between the fluids is of interest. When the assumptions for the VOF model do not hold, the mixture model could be used [84].

2.5.2.2. Mixture Model

The mixture model treats the different phases as interpenetrating continua. It solves for the the mixture momentum equation and prescribes relative velocities to describe the dispersed phase. It is different from the VOF model because the mixture model allows the phases to be interpenetrating, and to move at different velocities using the concept of slip velocities. The continuity equation for the mixture is

$$\frac{\partial}{\partial t}(\rho_m) + \nabla \cdot (\rho_m \vec{v}_m) = 0 \tag{2.54}$$

with $\vec{v}_m$ the mass-averaged velocity

$$\vec{v}_m = \frac{\sum_{k=1}^{n} \alpha_k \rho_k \vec{v}_k}{\rho_m} \quad , \tag{2.55}$$

ρ_m the mixture density

$$\rho_m = \sum_{k=1}^{n} \alpha_k \rho_k \quad , \tag{2.56}$$

and α_k the volume fraction of phase k. The momentum equation for the mixture can be obtained by summing the individual momentum equations for all phases. This leads to the following equation for the conservation of momentum

$$\frac{\partial}{\partial t}(\rho_m \vec{v}_m) + \nabla \cdot (\rho_m \vec{v}_m \vec{v}_m) = -\nabla p + \nabla \cdot \left[\eta_m (\nabla \vec{v}_m + \nabla \vec{v}_m^T) \right] + \rho_m \vec{g} + \vec{F} + \nabla \cdot \left(\sum_{k=1}^{n} \alpha_k \rho_k \vec{v}_{dr,k} \vec{v}_{dr,k} \right) \tag{2.57}$$

where n is the number of phases, F the body force, η_m the viscosity of the mixture expressed as

$$\eta_m = \sum_{k=1}^{n} \alpha_k \eta_k \quad , \tag{2.58}$$

and $v_{dr,k}$ the drift velocity for secondary phase k

$$\vec{v}_{dr,k} = \vec{v}_k - \vec{v}_m \tag{2.59}$$

If the phases are moving at different velocities, the mixture model solves for the relative velocities of the secondary phases. Additionally, it solves for a volume fraction equation for the secondary phase, that can be obtained from the continuity equation [84].

2.5.2.3. Eulerian Models

The Eulerian model is the most complex out of the multiphase models discussed. As with the mixture model, it treats the different phases as interpenetrating continua. The Eulerian model solves a set of n momentum and continuity equations for each phase. The coupling of the phases is achieved through the pressure and interphase exchange coefficients. It allows for the modeling of multiple separate, yet interacting phases. The Eulerian model is based on a single pressure that is shared by all phases, and momentum and continuity equations that are solved for each phase.

In the Eulerian model, the volume fractions represent the space occupied by each phase, and the laws of conservation of mass and momentum are satisfied by each phase individually. The volume fraction of each phase is calculated from a continuity equation, described by

$$\frac{1}{\rho_{rq}} \left(\frac{\partial}{\partial t}(\alpha_q \rho_q) + \nabla \cdot (\alpha_q \rho_q \vec{v}_q) = \sum_{p=1}^{n} (\dot{m}_{pq} - \dot{m}_{qp}) \right) \tag{2.60}$$

with ρ_{rq} the phase reference density, or the volume averaged density of the q^{th} phase in the solution domain. The conservation of momentum for a fluid phase q is given as

$$\begin{aligned} \frac{\partial}{\partial t}(\alpha_q \rho_q \vec{v}_q) + \nabla \cdot (\alpha_q \rho_q \vec{v}_q \vec{v}_q) = -\alpha_q \nabla p + \nabla \cdot \overleftrightarrow{\tau} + \alpha_q \rho_q \vec{g} + \sum_{p=1}^{n} (K_{pq}(\vec{v}_p - \vec{v}_q) \\ + \dot{m}_{pq} \vec{v}_{pq} - \dot{m}_{qp} \vec{v}_{qp}) + (\vec{F}_q + \vec{F}_{lift,q} + \vec{F}_{vm,q}) \end{aligned} \tag{2.61}$$

with $\vec{F}_q$ the external body force, $\vec{F}_{lift,q}$ the lift force, $\vec{F}_{vm,q}$ the virtual mass force, K_{pq} the exchange coefficient, and $\overleftrightarrow{\tau}$ the phase stress tensor defined by

$$\overleftrightarrow{\tau} = \alpha_q \eta_q (\nabla \vec{v}_q + \nabla \vec{v}_q^T) + \alpha_q (\lambda_q - \frac{2}{3} \eta_q) \nabla \cdot \vec{v}_q \overleftrightarrow{I} \quad . \tag{2.62}$$

Here η_q and λ_q are the shear and bulk viscosity of phase q. Furthermore, the exchange coefficient is defined by

$$K_{pq} = \frac{\alpha_q \alpha_p \rho_p f}{\tau_p} \quad , \tag{2.63}$$

with f the drag function, and τ_p the particulate relaxation time defined by

$$\tau_p = \frac{\rho_p d_p^2}{18\eta_q} \quad . \tag{2.64}$$

Here d_p is the diameter of the bubbles or droplets of phase p. The drag function is a function of the drag coefficient, and the Reynolds number [84].

Depending on what is simulated, an appropriate model should be chosen. Additionally, a discrete phase can be added into the simulation.

2.5.2.4. Discrete Phase Model

The trajectory of a discrete phase particle is predicted by integration of a force balance on the particle. The force balance equates the particle inertia with the forces acting on the particle, and can be written as (for the x direction in Cartesian coordinates)

$$\frac{dv_p}{dt} = F_D(v - v_p) + \frac{g_x(\rho_p - \rho_L)}{\rho_p} + F_x \quad . \tag{2.65}$$

Here, F_x is an additional acceleration term, v the fluid phase velocity, v_p the particle velocity, and $F_D(v - v_p)$ is the drag force per unit particle mass in which

$$F_D = \frac{18\eta}{\rho_p d_p^2} \frac{C_D Re}{24} \tag{2.66}$$

Here, Re is the relative Reynolds number, defined as

$$Re \equiv \frac{\rho d_p \left| v_p - v \right|}{\eta} \tag{2.67}$$

In F_x a virtual mass force can be added. This is used to model the force required to accelerate the fluid surrounding the particle, and is defined as

$$F_x = \frac{1}{2} \frac{\rho}{\rho_p} \frac{d}{dt} \left(v - v_p \right) \quad . \tag{2.68}$$

Additionally, Saffman's lift force can be added to the force balance. This is the lift due to shear, and is intended for small particle Reynolds numbers. This force is often added for submicron particles, and is defined by

$$\vec{F} = \frac{2K\nu^{1/2}\rho_L d_{ij}}{\rho_p d_p (d_{lk} d_{kl})^{1/4}} \left(\vec{v} - \vec{v}_p \right) \quad . \tag{2.69}$$

Here $K = 2.594$, and d_{ij} is the deformation tensor[85].

Often, in multiphase flows the situation is turbulent. Turbulent flows are characterized by fluctuating velocity fields. The fluctuating fields also cause fluctuations in momentum, energy, and species concentration. These fluctuations can be of small scale and have high frequency, thus direct simulation is often too computationally expensive. To solve this problem, instantaneous governing equations can be time-averaged, ensemble-averaged, or otherwise manipulated to remove the resolution of small scales. The modified equations are less computationally expensive, but do contain additional unknown variables, for which turbulence models are needed to express the unknown variables in known quantities [86]. In the next sections, a selection of turbulence models will be reviewed.

2.5.3. Turbulence Models

Which turbulence model to choose highly depends on the situation to be simulated. The choice will depend among other things on the physics encompassed in the flow, the level of accuracy required, the available computational resources, and the amount of time available for the simulation. The simplest models of turbulence are the two-equation models in which the solution of two separate transport equations determines the turbulent velocity and lenght scales independently. One of the popular turbulence models is the $k-\epsilon$ model, because of its robustness, economy, and reasonable accuracy for a wide range of turbulent flows [86].

2.5.3.1. $k-\epsilon$ Models

The standard $k-\epsilon$ model is a semi-empirical model based on model transport equations for the turbulence kinetic energy, k, and its dissipation rate, ϵ. The model assumes that the flow is fully turbulent, and that the effects of molecular viscosity are negligible. The turbulence kinetic energy is obtained from the transport equation shown in Equation 2.70. The rate of dissipation of the turbulence kinetic energy is obtained from the transport equation shown in Equation 2.71.

$$\frac{\partial}{\partial t}(\rho k)+\frac{\partial}{\partial x_i}(\rho k u_i)=\frac{\partial}{\partial x_j}\left[\left(\eta+\frac{\eta_t}{\sigma_k}\right)\frac{\partial k}{\partial x_j}\right]+G_k+G_b-\rho\epsilon-Y_M+S_k \tag{2.70}$$

$$\frac{\partial}{\partial t}(\rho \epsilon)+\frac{\partial}{\partial x_i}(\rho \epsilon u_i)=\frac{\partial}{\partial x_j}\left[\left(\eta+\frac{\eta_t}{\sigma_\epsilon}\right)\frac{\partial \epsilon}{\partial x_j}\right]+C_{1\epsilon}\frac{\epsilon}{k}(G_k+C_{3\epsilon}G_b)-C_{2\epsilon}\rho\frac{\epsilon^2}{k}+S_\epsilon \tag{2.71}$$

In these equations, G_k represents the generation of turbulence kinetic energy due to the mean velocity gradients, G_b the generation of turbulence kinetic energy due to buoyancy, and Y_M the contribution of the fluctuating dilatation in compressible turbulence to the overall dissipation rate. Furthermore, σ_k and σ_ϵ represent the turbulent Prandtl numbers for k and ϵ, respectively. S_k and S_ϵ are source terms, and lastly, $C_{1\epsilon}$, $C_{2\epsilon}$, and $C_{3\epsilon}$ are constants. The turbulent viscosity, η_t, is computed by combining k and ϵ:

$$\eta_t=\rho C_\eta\frac{k^2}{\epsilon} \tag{2.72}$$

with C_η a constant.

Two improvements have been proposed to the standard $k-\epsilon$ model, namely the renormalization group, or RNG, and realizable $k-\epsilon$ models. The RNG model has an additional term in its ϵ equation that significantly improves the accuracy for rapidly strained flows, it includes the effect of swirl on turbulence, and it provides an analytical formula for turbulent Prandtl numbers. The improved equations for the RNG $k-\epsilon$ model are displayed in Equations 2.73 and 2.74.

$$\frac{\partial}{\partial t}(\rho k)+\frac{\partial}{\partial x_i}(\rho k u_i)=\frac{\partial}{\partial x_j}\left(\alpha_k\eta_{eff}+\frac{\partial k}{\partial x_j}\right)+G_k+G_b-\rho\epsilon-Y_M+S_k \tag{2.73}$$

$$\frac{\partial}{\partial t}(\rho \epsilon)+\frac{\partial}{\partial x_i}(\rho \epsilon u_i)=\frac{\partial}{\partial x_j}\left[\left(\eta+\frac{\eta_t}{\sigma_\epsilon}\right)\frac{\partial \epsilon}{\partial x_j}\right]+C_{1\epsilon}\frac{\epsilon}{k}(G_k+C_{3\epsilon}G_b)-C_{2\epsilon}\rho\frac{\epsilon^2}{k}-R_\epsilon+S_\epsilon \quad . \tag{2.74}$$

In these equations, α_k and α_ϵ are the inverse effect Prandtl numbers for k and ϵ.

The realizable $k-\epsilon$ model contains a new formulation for the turbulent viscosity, and a new transport equation for the dissipation rate that has been derived from an exact equation for the transport of the mean-square vorticity fluctuation. The two transport equations are shown in Equations 2.75 and 2.76.

$$\frac{\partial}{\partial t}(\rho k) + \frac{\partial}{\partial x_j}(\rho k u_j) = \frac{\partial}{\partial x_j}\left[\left(\eta + \frac{\eta_t}{\sigma_\epsilon}\right) + \frac{\partial k}{\partial x_j}\right] + G_k + G_b - \rho\epsilon - Y_M + S_k \tag{2.75}$$

$$\frac{\partial}{\partial t}(\rho \epsilon) + \frac{\partial}{\partial x_j}(\rho \epsilon u_j) = \frac{\partial}{\partial x_j}\left[\left(\eta + \frac{\eta_t}{\sigma_\epsilon}\right)\frac{\partial \epsilon}{\partial x_j}\right] + \rho C_1 S_\epsilon - \rho C_2 \frac{\epsilon^2}{k+\sqrt{\nu\epsilon}} + C_{1\epsilon}\frac{\epsilon}{k}C_{3\epsilon}G_b + S_\epsilon \quad . \tag{2.76}$$

Here, $C_1 = max\left[0.43\frac{\eta}{\eta+5}\right]$, $\eta = S\frac{k}{\epsilon}$, $S = \sqrt{2S_{ij}S_{ij}}$. Furthermore, in Equations 2.75 and 2.76, C_2 and $C_{1\epsilon}$ are constants [86].

Instead of the turbulent dissipation, you can also solve for the specific dissipation rate, which can be thought of as the ratio of ϵ to k. The model that includes the specific dissipation rate is called the $k-\omega$ model, and will be covered in the next section [86].

2.5.3.2. $k-\omega$ Models

The $k-\omega$ model also solves two differential equations. One for the turbulent kinetic energy, k, and one for the specific turbulent dissipation rate, ω. The turbulence kinetic energy, and the specific disspiation rate can be obtained from the transport equations shown in Equations 2.77 and 2.78.

$$\frac{\partial}{\partial t}(\rho k) + \frac{\partial}{\partial x_i}(\rho k u_i) = \frac{\partial}{\partial x_j}\left(\Gamma_k \frac{\partial k}{\partial x_j}\right) + G_k - Y_k + S_k \tag{2.77}$$

$$\frac{\partial}{\partial t}(\rho \omega) + \frac{\partial}{\partial x_i}(\rho \omega u_i) = \frac{\partial}{\partial x_j}\left(\Gamma_\omega \frac{\partial \omega}{\partial x_j}\right) + G_\omega - Y_\omega + S_\omega \quad . \tag{2.78}$$

Here, G_k represents the generation of turbulence kinetic energy due to mean velocity gradients. G_ω the generation of ω, Γ_k and Γ_ω the effective diffusivity of k and ω, respectively, Y_k and Y_ω the dissipation of k and ω due to turbulence, and S_k and S_ω are source terms. In the $k-\omega$ model, low Reynolds number corrections can be added. To this end, the coefficient α^* damps the turbulent viscosity. α^* is described by

$$\alpha^* = \alpha^*_\infty \left(\frac{\alpha^*_0 + Re_t/R_k}{1 + Re_t/R_k}\right) \quad , \tag{2.79}$$

with $Re_t = \frac{\rho k}{\eta\omega}$, $R_k = 6$, $\alpha^*_0 = \frac{\beta_i}{3}$, and $\beta_i = 0.072$. For high Reynolds numbers $\alpha^* = \alpha^*_\infty = 1$.

To be able to effectively blend the robust and accurate formulation of the $k-\omega$ model in the near wall region with the free stream independence of the $k-\epsilon$ model in the far field, the shear-stress transport, or SST, $k-\omega$ model was developed. The differences between the standard and the SST k-ω are that the SST uses the standard $k-\omega$ model in the inner region of the boundary layer and gradually changes to a high-Reynolds

version of the $k-\epsilon$ model in the outer part of the boundary layer. Furthermore, the SST k-$k-\omega$ uses a modified turbulent viscosity formulation to account for the transport effects of the principal turbulent shear stress. The two differential equations are shown in Equations 2.80 and 2.81.

$$\frac{\partial}{\partial t}(\rho k) + \frac{\partial}{\partial x_i}(\rho k u_i) = \frac{\partial}{\partial x_j}(\Gamma_k \frac{\partial k}{\partial x_j}) + \tilde{G}_k - Y_k + S_k \tag{2.80}$$

$$\frac{\partial}{\partial t}(\rho \omega) + \frac{\partial}{\partial x_i}(\rho \omega u_i) = \frac{\partial}{\partial x_j}(\Gamma_\omega \frac{\partial \omega}{\partial x_j}) + G_\omega - Y_\omega + D_\omega + S_\omega \tag{2.81}$$

With, D_ω the cross-diffusion term.

Both the $k-\epsilon$ and the $k-\omega$ models are based on the Boussinesq hypothesis. They assume that the turbulent viscosity is an isotropic scalar quantity, which is strictly not true. The alternative approach is to solve transport equations for each of the terms in the Reynolds stress tensor, and an additional scale-determining equation. This means that five additional transport equations are required in 2D, and seven in 3D to be solved. This alternative approach is the basis of the Reynolds Stress Model, or RSM, treated in the next section [86].

2.5.3.3. Reynolds Stress Model

The RSM accounts for the effects of streamline curvature, swirl, rotation, and rapid changes in strain rate in a more rigorous manner than the two-equations turbulence models. It has greater potential to give accurate predictions for complex flows. However, the accuracy of the RSM is still limited by assumptions in various terms of the exact transport equations for the Reynolds stresses. Especially the modeling of the pressure-strain and dissipation-rate terms is challenging [86].

The complete derivation of the RSM is outside the scope of this thesis, as the flow modeled does not require the use of a more complex model. Therefore, the equations used in the RSM are not considered here.

CHAPTER 3
METHODOLOGY

This thesis concerns an experimentally investigation of the entrainment process, data and image analysis, and numerical simulations. In this chapter first the different types of particles that have been utilized to investigate particle removal are examined. The materials will be followed by an overview of the experimental set-up of the bubble column. Subsequently, the experimental procedure, and analysis of the determination of bubble sizes, bubble rise velocity, and particle velocity will be covered. Lastly, the numerical method will be discussed. For the numerical method, first a model was derived that included an inlet for bubble formation, however, this resulted in divergence of the simulation and therefore, no results were obtained, and this model is excluded from this thesis. Due to divergence issues for a complete model, a simple model was created that determined the effect of the rise of a single bubble on particle recovery. The numerical method behind this simple model will be reviewed in the last section.

3.1. Materials

In the experiments hollow glass spheres manufactured by LaVision and zinc-oxide and nickel particles manufactured by US Research Nanomaterials, Inc. were utilized, and their velocity profiles were compared. The glass hollow spheres are neutrally buoyant, meaning that if there is no external field, the glass particles are stable and do not sink or rise in the fluid [87]. It is therefore expected that the glass hollow spheres follow the streamlines of the fluid induced by the bubbles. Zinc-oxide is a light particle, with a density of $5610\ kg \cdot m^{-3}$, and nickel has a much higher density of $8900\ kg \cdot m^{-3}$. The density difference between nickel and water is comparable to the density difference between molybdenum, which is $10200\ kg \cdot m^{-3}$, and molten salt. Therefore, the buoyancy of nickel in water is comparable to the buoyancy of molybdenum in molten salt. Molybdenum-99 is one of the major non-soluble fission products produced in the MSR [31]. Since Molybdenum particles were not available in a large size range, nickel particles were used as a substitute to molybdenum. Zinc-oxide particles were used to understand the influence of the particle density on the entrainment process and investigate the limits of ultra-fine particle recovery. The specifics of the materials em-

ployed in the experiments are outlined in Table 3.1. Additionally, in all experiments demineralized water was used as a liquid medium and air was utilized to form gas bubbles.

Table 3.1: All particles used in experimental work.

Material	Diameter	Purity
Glass hollow spheres	9-13 µm	-
ZnO	10 µm	99.5%
ZnO	5 µm	99.5 %
ZnO	1 µm	99.5 %
ZnO	500 nm	99.5 %
Ni	10 µm	99.5%
Ni	5 µm	99.5%
Ni	1 µm	99.5%
Ni	500 nm	99.5%

3.2. Experimental set-up

To investigate the limits of particle recovery using entrainment, two model columns are used. The columns and their parts are shown in Figure 3.2.1. Both columns are made of clear PMMA. The column labeled from now on as the small column has an inner diameter of $30\ mm$, and a total height of $450\ mm$. The column labeled as the large column, has an inner diameter of $50\ mm$, and also a total height of $450\ mm$. To be able to obtain accurate measurements from the LDA, the laser needs a flat surface, since the curved shape of the column can lead to distortions in the laser pathway. To this end, the small and large column have three polished edges of a width of 16 and $21\ mm$, respectively. One of the polished edges lies perpendicular to the laser, while the other two edges are parallel to the laser beam and positioned opposite of each other. In all experiment the water level was kept at the same level for consistency, namely $3\ cm$ underneath the opening of the column. The inlet and collector conditions were varied and will be specified at each obtained result. For the small column, an inlet diameter of 1, 1.5 and $2.5\ mm$ was used, whereas for the large column only an inlet diameter of $1\ mm$ was used. For the small column, two collectors were used, one with an opening diameter of $7.5\ mm$ and an angle of $60°$, another with an opening diameter of $10\ mm$ and an angle of $64.7°$, ensuring equal cone heights. For the large column, only the collector was used that has an opening diameter of $10\ mm$ and an angle of $61.9°$. All collectors, and inlets are 3D printed and made of PLA. To the inlet a gas line was attached, with a continuous flow condition. The volume flow ($\dot{V}$), was varied between experiments, and will be denoted at each experiment. To regulate the volume flow, a Bronkhorst flow regulator was used. The flow regulator can operate between 1 and $1.5\ bar$, with a maximum volume flow of $500\ \ cm^3 \cdot min^{-1}$. Lastly, most experiments were carried out with an operation time of one hour. However, alternate separation times in between the start of the experiment and operation time of particle collection were conducted to measure the progress of the particle separation.

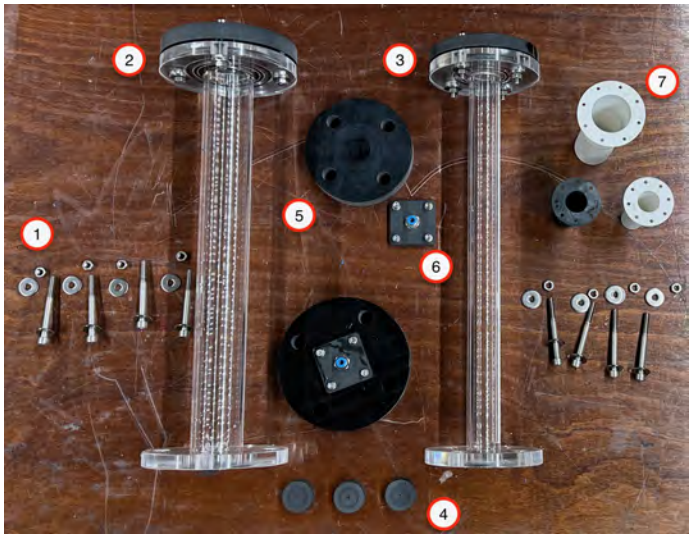

(a)

(b)

Figure 3.2.1: Dissembled experimental setup (a) and schematic (b) consisting of 1: screws to assemble lower part of column set-up, 2: Column with diameter 50 mm, 3: column with diameter 30 mm, 4: inlets with different diameters, options are 1, 1.5, 2, and 2.5 mm, 5: lower part of column, where the inlet diameter can be switched, 6: gas inlet, 7: collectors, options are for the 50 mm column an opening diameter of 10 mm with angle 61.9° and for the 30 mm column an opening diameter of 10 mm with angle 64.7 ° or an opening diameter of 7.5 mm with angle 60°.

Depending on the column and particle, a certain mass of particles was used in the experiments. In the small column the concentration of the zinc-oxide particles was $\sim 3.1 \cdot 10^{-4}\ g \cdot cm^{-3}$, and the nickel particles was $\sim 6.29 \cdot 10^{-4}\ g \cdot cm^{-3}$. In the large column the concentration of the nickel particles was $\sim 6.79 \cdot 10^{-4}\ g \cdot cm^{-3}$.

3.3. Experimental Procedure

In this section a step-by-step guide of the experimental procedure will be covered.

First, the column was assembled with the desired inlet. Then the column was attached to two hooks fixed to a pole, so that the column was secured vertically. Next, the gas line was connected to the column, and set to the desired volume flow. The column was filled with demineralised water until a few centimeters underneath the defined liquid height. The particles were then dispersed into the column. After a few minutes the collector was placed into the column, and the column was filled until the required liquid height was reached. Following this step, LDA measurements were conducted at intervals of 5, 20, 35, and 50 minutes under the various conditions. In the meantime, a vacuum filtration setup consisting of a Büchner funnel and flask was prepared for particle recovery measurement. This was done by placing a Durapore $0.1\ \mu m,\ 25\ mm$ PVDF membrane of known mass into the funnel, and using the available vacuum line, a vacuum was created in the flask. After the required operation time passed, the volume flow of the gas was put to zero, so that no new bubbles were formed in the column. The collector was removed, and using demineralised water, the particles were

flushed out of the collector into the Büchner funnel. After the water was sucked out of the funnel into the flask, the membrane was taken out of the funnel. At least three days passed for drying under ambient conditions to weigh the mass of the membrane including the particles to ensure that all water had vaporized from the membrane and only the particles were left. The recovery was then calculated as

$$R = \frac{m_{membrane,out} - m_{membrane,in}}{m_{particles,in}} \quad . \tag{3.1}$$

Here, $m_{membrane,out}$ is the mass of the membrane plus the filtered particles after particle recovery, $m_{membrane,in}$ the mass of the membrane before particle recovery, and $m_{particles,in}$ the mass of the particles deposited into the column.

3.4. Characterization

To quantify the data gathered from experiments, several procedures have been implemented. Initially, the bubble quantities of bubbles within the column were assessed, followed by the determination of particle velocity and recovery. This section describes all the procedures undertaken during image and data analysis.

3.4.1. Bubble Size

Bubble size might influence the flow regime inside the column, which in turn could influence particle entrainment. Therefore, it is important to know the sizes of the bubbles that are being formed in the column. To characterize the bubble size inside the column under different conditions, images were taken using a Nikon Z50 camera, equipped with a Nikkor MC 105/2.8 S lens and a HB-99 suncap. The shuttertime was 1/1000, aperture 5.6 and iso 6400. The images taken contained a number of bubbles. These images were then manually cut into single-bubble images, based on the criteria that the bubbles were in-focus, fully in the picture, and not in contact with other bubbles. The background removal tool within macOS Sonoma version 14.1.2 was used to remove the background of the single bubble images. These images were then loaded one by one into a handwritten Python code, which can be found in the Appendix. In the Python code the image was first converted to a gray image. Then the total length of the image in pixels was determined in both the horizontal and the vertical direction. Next, a grid of 50 points in the horizontal direction and 50 points in the vertical direction was drawn in the image. The intensity of the background of the images was equal to one, and the bubble itself has an intensity lower than one. Thus, based on the intensity of the location of the grid, points were determined at the outer radius of the bubble, see Figure 3.4.1a. Subsequently, through these points an ellipse was fitted (Figure 3.4.1b), using

$$\frac{((x-h)cos(A) + (y-k)sin(A))^2}{d_h^2} + \frac{((x-h)sin(A) - (y-k)cos(A))^2}{d_v^2} = 1 \quad . \tag{3.2}$$

From the fitted ellipse the minor and major axis of the ellipse was extracted as a number of pixels. The fitting algorithm used was a least squares dogbox method. Least

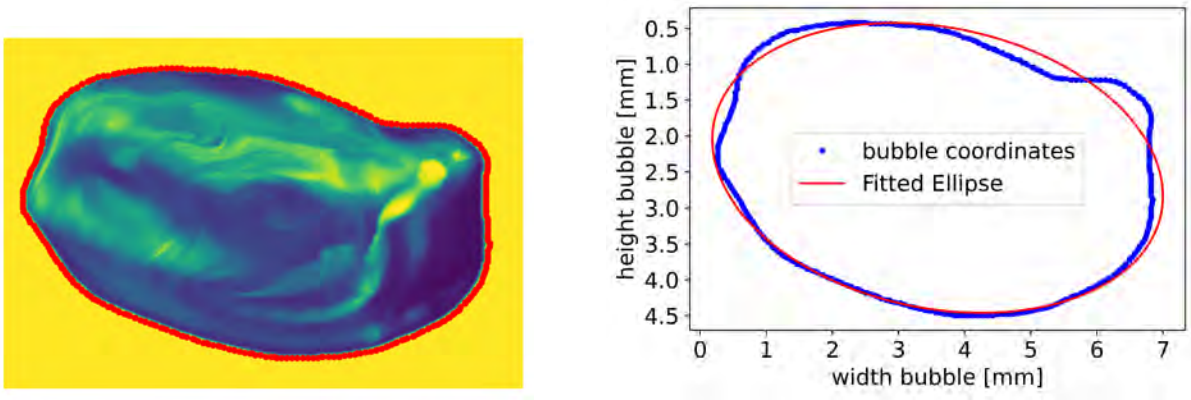

(a) *(b)*

Figure 3.4.1: x and y coordinates obtained from python code (a) and ellipse fitted to x and y coordinates found from python code (b). Example displayed from a single bubble in the small column with a volume flow of $150\ \ cm^3 \cdot min^{-1}$ *and inlet diameter of* $1\ mm$.

squares fitting uses regression analysis based on minimizing the sum of the squares of the residuals. The dogbox algorithm uses rectangular trust regions, and is typically used in small problems with bounds [88]. The minor and major axis of the fitted ellipse were used for further analysis. To convert the minor and major axis from a number of pixels to a metric size, Equation 3.3 was used.

$$H_{object} = D\frac{h_{object}[pixels]}{h_{sensor}[pixels]}\frac{h_{sensor}[mm]}{f_{eff}[mm]} \tag{3.3}$$

Here H_{object} is the size of the object, D the distance of the lens to the middle of the column, h_{object} the size of the object in pixels, h_{sensor} the image sensor size in pixels or millimeters, and f_{eff} the effective focal length of the camera. The effective focal length is calculated by multiplying the focal length of the camera with the crop factor [89]. Table 3.2 shows the constants used in Equation 3.3.

Table 3.2: Constants used to scale pixels to metric size.

	Scaling Images	Scaling Videos
Distance camera [mm]	305	1000
Total image size [pixels]	5568x3712 [90]	3840x2160 [90]
Image sensor size [mm]	24x16 [90]	24x14 [90]
Focal length [mm]	105 [90]	105[90]
Crop Factor	1.5 [91]	1.5 [91]

Additionally, the reasoning behind a 50x50 grid over the image becomes evident from Figure 3.4.2. When less than 50 points were taken, a large error occurred when determining a fit through the data points, whereas for more than 50 data points, the computational cost of the fitting became significantly higher, without a profound improvement in the error of the fit.

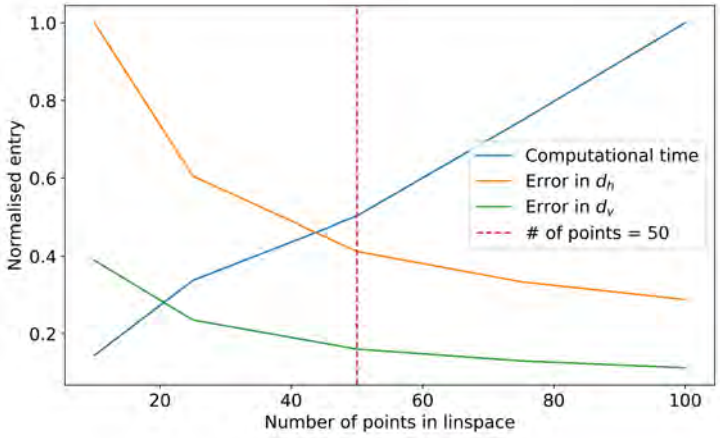

Figure 3.4.2: Comparison between computational time and mean error in long and small axis of fitted ellipse.

To characterize the bubble sizes in the column the assumption was made that the bubbles are well approximated as ellipsoids. From the minor and major axis determined from the images, a bubble chord length was calculated as described by Mohagheghian and Elbing (2018) [46] in Equation 3.4.

$$d_b = \sqrt{\frac{4\chi A_{proj}}{\pi}} \tag{3.4}$$

Here χ is the ratio between the major and the minor axis, i.e. the aspect ratio, and A_{proj} the bubble cross sectional area, which was determined by

$$A_{proj} = \frac{\pi}{4} d_h d_v \quad . \tag{3.5}$$

Then, the bubble chord length was rounded to zero decimals, and the bubble size distribution determined by counting the number of times a bubble size is present in the population. The bubble size distribution has been determined for the small column, including the three different inlet conditions, and the big column with an inlet diameter of one millimeter. Each population consisted of between 82 and 164 bubbles. Often a bubble size distribution is described using a log-normal distribution [47, 48, 92, 93]. Therefore, a log-normal curve described by

$$f(d_b) = \frac{1}{\sqrt{2\pi}\sigma d_b} e^{-\frac{1}{2}\left(\frac{ln(d_b - m)}{\sigma}\right)^2} \tag{3.6}$$

was fitted through the bubble size distributions. From this fit a R^2-value was determined to find the correlation between the bubble size distribution and the fitted curve. The R^2 of a fit is expressed as

$$R^2 = 1 - \frac{SS_{res}}{SS_{tot}} \quad . \tag{3.7}$$

Here SS_{res} is the residual sum of squares, and can be calcaluted by $SS_{res} = \sum_i^n (y_i - f_i)^2$, with f_i the calculated i^{th} dependent variable based on the fitting equation. SS_{tot} is the

total sum of squares, given by $SS_{tot} = \sum_i^n (y_i - \overline{y})^2$, with y_i the i-dependent variable in a data set of size n, and $\overline{y}$ the average value calculated by $\overline{y} = \frac{1}{n}\sum_i^n y_i$ [94].

The Sauter Mean diameter is the most widely used characteristic length in bubble column studies [46, 47, 48, 49], therefore the Sauter mean diameter was calculated as described in Equation 2.1. In this thesis, the number population of bubble chord lengths were used to determine the Sauter mean diameter, with n_i the number of bubbles with bubble chord length d_i.

Additionally, the volume equivalent diameter was determined using Equation 2.5 [43, 52]. The average bubble equivalent diameter was used to compare the average bubble rise velocity, with the average volume equivalent diameter to different models relating the bubble rise velocity to the bubble size. The procedure to determine the bubble rise velocity experimentally will be the subject of the next section.

3.4.2. Bubble Rise Velocity

To experimentally determine the bubble rise velocity, twelve videos were taken of approximately five seconds of the conditions shown in Table 3.3. The videos were taken using the same Nikon Z50 camera as used for taking pictures. The video-resolution of the camera was 3840 by 2160 pixels, and the framerate was 30 frames per second. The videos were then extracted into single images and exported to ImageJ, FIJI. In FIJI the MTrackJ plugin was used to track the motion of the bubbles. This was done by clicking approximately in the middle of the bubble during its trajectory. Each condition concerns trajectories from at least 37 and maximum 93 bubbles. Then the trajectories were measured by the MTrackJ plugin and for each trajectory the x-, y-, and t-coordinates were extracted. To determine the deviation in bubble rise velocity, the trajectory of one bubble was established ten times for the small column with inlet diameter of $1\ mm$ for the different volume flows. The x-, y-, and t-coordinates were then also extracted from the MTrackJ plugin.

Table 3.3: Conditions differed in videos to determine bubble rise velocity.

Column width $[mm]$	Inlet	Volume Flow $[cm^2.min^{-1}]$
30	1	100, 300 500
30	1.5	100, 300, 500
30	2.5	100, 300, 500
50	1	300, 400, 500

The coordinates were then converted from pixels to millimeters using Equation 3.3, with constants given in Table 3.2. The total displacement in the x-, and y-direction were determined over the total time. The x- and y-velocities were then determined by

$$v_n = \frac{dn}{dt}; \quad n = x, y \quad . \tag{3.8}$$

The total velocity for each trajectory was then calculated as

$$v_{tot} = \sqrt{v_x^2 + v_y^2} \tag{3.9}$$

Then the average of all the trajectories per condition was determined and used to compare the velocities measured with existing models for the bubble rise velocity. The models that were compared to the experimental data were described by Park et al. (2017) (Equation 2.19) [53], Chavez et al. (2021) (Equation 2.26) [19], Clift, Grace, and Weber (1978) (Equation 2.27) [59], Islam et al. (2013) (Equation 2.20) [54], and Krishna et al. (1999) (Equation 2.23) [55]. The error in average velocity was assumed to be equal to the standard deviation from the repeated measurement of the single bubble.

The velocity distributions of the particles induced by the bubbles were examined using a LDA set-up. The characterization of the LDA measurements will be the subject of the next section.

3.4.3. LDA output

The measurement device used to perform the LDA is a Dantec Dynamics Flowexplorer DPSS, equipped with a dual laser setup with a backscatter type receiver. The device is placed upon a 3D traverse system, see Figure 3.4.3a. The dual lasers can output up to 500 mW with a wavelength of 532 nm and 561 nm. In the experiments, the power of both laserbeams was set to $40\ mW$.

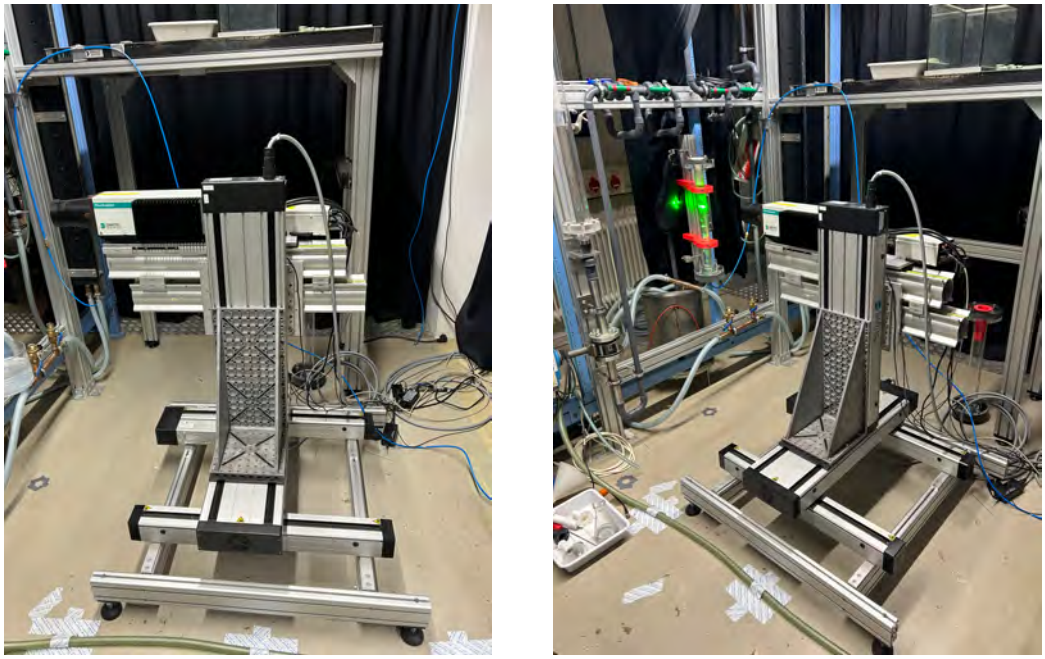

(a) *(b)*

Figure 3.4.3: The Dantec laser placed upon a 3D traverse system (a) and measurement position of the laser beams (b).

For consistency, the LDA measurements were performed at the same location in the middle of the column, see Figure 3.4.3b, three times for three minutes. Hence, the output comprised of three data files that all consists among other things of the number of particles counted in the measurement window, and their vertical and horizontal velocity. Since the interest lies solely in the vertical direction, denoting the lift of the

particles by the bubbles, only the vertical velocity was extracted from the LDA data. These datasets contained a normal distribution with a fat tail towards the positive vertical direction. Therefore, for easier visualization, a double Gaussian distribution was fitted through the datasets, see Equation 3.10.

$$f(x) = \frac{1}{\sigma_1\sqrt{2\pi}} e^{-\frac{1}{2}\left(\frac{x-\mu_1}{\sigma_1}\right)^2} + \frac{1}{\sigma_2\sqrt{2\pi}} e^{-\frac{1}{2}\left(\frac{x-\mu_2}{\sigma_2}\right)^2} \tag{3.10}$$

Since in a single measurement, three datasets were obtained, to determine a fit through the data points, it is useful to know whether all three data files can be combined, or that they have to be analyzed separately. To this end, statistical tests were performed that will be considered in the next paragraph.

To determine a single fit through all three data files, it was assumed that there is no significant difference between the measured data sets, thus assuming that the datasets are identical. If the data is identical, a single fit applied to all data sets can be obtained, as opposed to employing three fits across the three distinct data sets. In order to assess the validity of the assumption of identical data the following procedure was conducted. It is known that the data sets are independent, normally distributed, and of 'ratio' scale. Therefore, a parametric test can be performed if the variances of the data sets are equal. To this end, Levene's test for equal variances was executed, using a median center, since a median center is recommended for skewed distributions [95]. If Levene's test is valid, the assumption was made that the data sets have equal variance, and therefore a parametric test could be performed. The parametric test executed was a one-way Analysis Of Variance (ANOVA) test. If the ANOVA test was valid, all data sets were merged and one fit was determined through all the data points. If the ANOVA test was not valid, a two sample t-test was used between datasets one and two, one and three, and two and three, to determine whether two data sets could be merged together. If the two sample t-test was not valid for any of the combinations, the fit was determined through the second data set. If Levene's test was not valid, a non-parametric test was used. To this end the Kruskal-Wallis test was executed to determine the difference between the data sets. If the Kruskal-Wallis test was valid, all data sets were merged and a fit was determined through all the data points. If the Kruskal-Wallis test was not valid, a Welch's t-test for unequal variances was performed between datasets one and two, one and three, and two and three, to determine whether two data sets could be merged together. Again, if the t-test did not hold for any of the combinations, the fit was determined through the second data set, see Figure 3.4.4. The theory behind the above mentioned tests have been discussed in section 2.4.

To test the validity of the fit through the data, a R^2 value was obtained as described in Equation 3.7. Furthermore, the Full Width at Half Maximum, or FWHM, and the velocity that occurred most often was determined. The FWHM is defined as the width of a line shape at half its maximum amplitude. For Gaussian distributions, the FWHM is about 2.4 times the standard deviation [96].

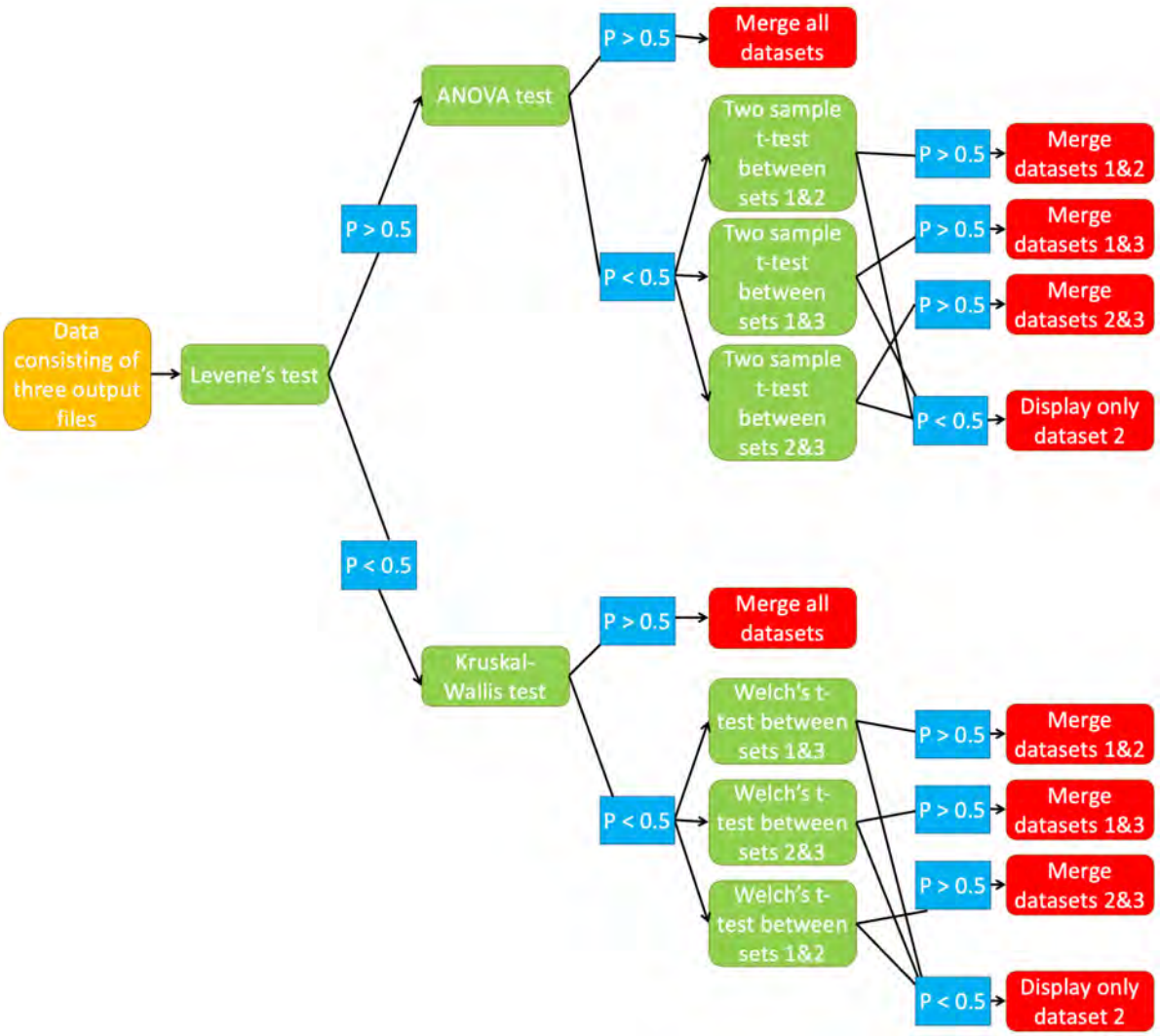

Figure 3.4.4: Decision making flowchart to determine which datasets obtained from LDA experiments could be taken together. The colors depict the following: yellow: input, green: tests performed, blue: output test, and red: output data.

3.4.4. Recovery over Time

Since theory and experiments indicate that flotation is first order with respect to the number of particles N [63], this was examined for entrainment as well. The rate equation for the removal of particles in a batch process is of the form

$$\frac{dN}{dt} = -kN \quad . \tag{3.11}$$

Here, k is the flotation rate constant, and t the flotation time. If the initial number of particles is N_0 at $t = 0$, Equation 3.11 can be integrated to yield

$$N = N_0 e^{-kt} \quad . \tag{3.12}$$

The recovery of the particles, R, is defined by

$$R = \frac{N_0 - N}{N_0} \quad , \tag{3.13}$$

so that Equation 3.12 can be rewritten to

$$R = R_{max}(1 - e^{-kt}) \tag{3.14}$$

as described by Miettinen, Ralston, and Fornasiero (2010) [63]. To test the validity of Equation 3.14 for entrainment instead of flotation, for different conditions the recovery after a certain period of time was measured. Equation 3.14 was then fitted through these measurement points, and an R^2-value using Equation 3.7 was determined.

3.5. Numerical Simulations in Ansys Fluent

This section describes the set-up of the simple numerical model used in the simulations for single bubble particle recovery inside the bubble column.

For the simulations the geometries were created using Ansys ICEM CFD. In Ansys ICEM CFD structured quadrilateral mesh elements were selected. The size of the geometries are shown in Table 3.4, and a schematic overview of all the meshes used is shown in Figure 3.5.1.

Table 3.4: All sizes of the meshes used.

Dimension	Mesh size (nodes×quads)	H_{column} [mm]	d_{column} [mm]	$d_{collector}$ [mm]	$\alpha_{collector}$ [°]	$H_{collector}$ [mm]
2D	68392×67486	300	30	n/a	n/a	n/a
3D	252250×244020	300	30	n/a	n/a	n/a
2D	58880×58123	210	30	10	60	17.32
2D	59315×58578	215	30	10	64.7	21.16
2D	59084×58335	212	30	7.5	60	19.49
2D	60812×60179	215	30	10	64.7	21.16 *
2D	111060×110043	250	50	10	61.9	37.46
2D	105732×104869	250	50	10	61.9	37.46 *

* different shape of column, see Figure 3.5.1 for the difference in shape.

After creating the mesh in Ansys ICEM CFD, the mesh was imported into an Ansys Fluent 2D or 3D double precision simulation. In all numerical simulations, the same model was used, only the geometries, and bubble sizes were differed. The general settings contained a transient model, since time plays a key role in the simulations and cannot be neglected. Furthermore, the velocity formulation was set to absolute and to be pressure based. The 2d space was planar, and constant gravity with a value of $-9.81\ kg \cdot m^{-2}$ was included in the axial direction.

The models used in Ansys Fluent included a Multiphase model, a Viscous model, and a Discrete Phase Model. For the multiphase model, an inhomogeneous Eulerian model was implemented. For the Eulerian parameters a Multi-Fluid VOF Model was

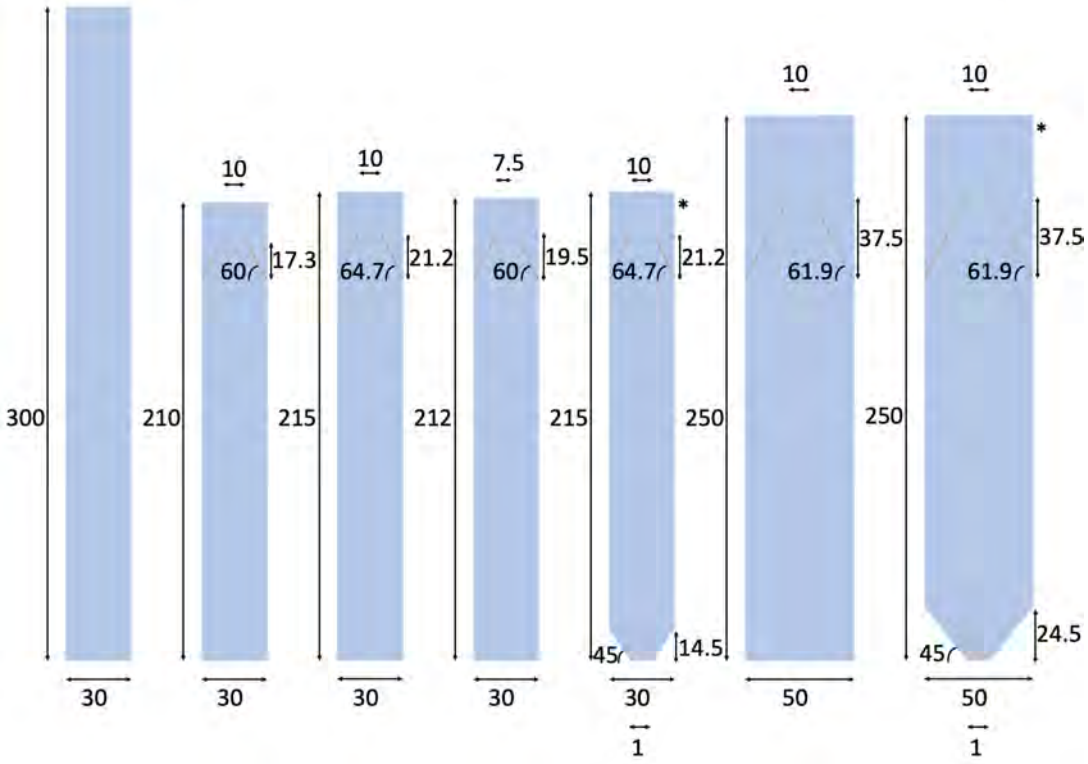

Figure 3.5.1: Dimensions of the 50 mm column, including full shape of column.

selected. The volume fraction parameters included an explicit formulation and default settings for both the volume fraction cutoff and the Courant number. For the interface modelling a sharp type was selected. The simulations included two phases. As the primary phase water was chosen with a density of $998\ kg \cdot m^{-3}$, and a viscosity of $0.001003\ kg \cdot (m \cdot s)^{-1}$. The secondary phase was air with a density of $1.225\ kg \cdot m^{-3}$, and a viscosity of $1.7894e-5\ kg \cdot (m \cdot s)^{-1}$. To model the surface tension, a Surface Tension Force Modeling with Continuum Surface Force model was selected. There was no adhesion to the wall, and the surface tension coefficient was $0.0728\ N \cdot m^{-1}$. There were no mass transfer mechanisms, the interfacial area was ia-symmetric, and the population balance model was off. When changing the model to molten salt and helium, only the properties of the constants were changed, not the model itself. For molten salt a $NaCl(59.66\ mol\%)-MgCl_2(35.06\ mol\%)-PuCl_3$ was utilized at a temperature of $700°\mathrm{C}$. Both the density and viscosity were set to constant, and the values were $1847.6\ kg \cdot m^{-3}$, and $0.00173\ kg \cdot (m \cdot s)^{-1}$, respectively. For helium the density and viscosity were set to $0.1625\ kg \cdot m^{-3}$ and $1.99e-5\ kg \cdot (m \cdot s)^{-1}$, respectively. The surface tension between the helium and the molten salt was calculated by

$$e^{\frac{-\sigma a}{RT}} = X_1 e^{\frac{-\sigma_1 a}{RT}} + X_2 e^{\frac{-\sigma_2 a}{RT}} \quad . \tag{3.15}$$

Here X is the fraction of the compound, R the gas constant, and a the area of the particle. Since R and a are assumed to be equal, the surface tension of the molten salt was calculated as

$$\sigma_{MS} = ln\left(0.6e^{\sigma_{NaCl}} + 0.4e^{\sigma_{MgCl_2}}\right) \quad . \tag{3.16}$$

Since $\sigma_{NaCl} = 0.116\ N \cdot m^{-1}$, and $\sigma_{MgCl_2} = 0.0621\ N \cdot m^{-1}$, $\sigma_{MS} = 0.116\ N \cdot m^{-1}$ [97]. Here the assumption was made that the surface tension would not change significantly between $700°\mathrm{C}$ and $800°\mathrm{C}$ and that $PuCl_3$ would not alter the surface tension notably.

As a viscous model, a turbulence model, namely the SST k-omega model, with low Reynolds number corrections was used. The low Reynolds number corrections improve the accuracy in predicting low Reynolds number flows. This was selected because in the case of a single bubble rising, the Reynolds numbers could be in the laminar flow range, instead of a turbulent flow range. The model constants were kept at default. Furthermore, the Production Limiter was on, the turbulence multiphase model was mixture based, and there was no turbulence damping.

For the discrete phase model there was no interaction with the continuous phase. The particles treatment included unsteady particle tracking, track with fluid flow time step and inject particles at fluid flow time step. The tracking parameters included a maximum number of steps of 500, with a step length factor of 5. Furthermore, high-res tracking was enabled. The physical models used were the Saffman lift force, and the virtual mass force with a virtual mass factor of 0.5. For the numerics the default settings were used, namely tracking options with accuracy control and a tolerance of $1 \cdot 10^{-5}$, and refinements at 20. The tracking scheme selection was automated, with as high order scheme trapezoidal and as a low order scheme an implicit scheme. The parallel methods were put to hybrid, and the dpm domain was not used. To inject the particles a surface was created by iso-clipping a surface to the mesh. In all simulations the particles were injected at a rectangle located at an y-coordinate from 140 till $150\ mm$. The injection type of the particles was thus a surface. The particle type was an inert particle, and the material either zinc-oxide with a density of $5610\ kg \cdot m^3$ or nickel with a density of $8900\ kg \cdot m^3$. The particles contained a uniform diameter distribution, and no discrete phase domain. The drag law was spherical, there was no particle rotation and no rough wall model. In all simulations the particles were injected for one time step, so for $0.0001\ s$, with zero velocity.

For the outlet boundary conditions, the gauge pressure was put to zero, and the pressure profile multiplier to one. The backflow direction specification method was normal to boundary, the turbulence specification model was intensity and viscosity ratio, with backflow turbulent intensity of 5%, and backflow turbulent viscosity ratio of 10. The dpm boundary condition was set to trap. The volume fraction specification method for air was put to backflow volume fraction with zero backflow volume fraction.

For the wall boundary conditions a distinction was made for two wall types. For both boundary conditions, the wall motion was put to stationary, with a standard roughness model with roughness height of $0\ mm$ and roughness constant of 0.5. For both water and air, the wall contained a no slip boundary condition. The boundary condition for the dpm-injection was varied. For the top part of the collector the boundary condition included a trap. Whereas for all other walls the boundary condition for the dpm-injection was put to a reflecting condition, with discrete phase reflection coefficients normal polynomial and tangent polynomial.

To indicate the starting location of the bubble, a region was created in the cell registers of the simulation. A circle was then drawn with varying x-, y- coordinates and radii.

To initialize the simulation, the standard initialization conditions were used. The gauge pressure was 0, the turbulent kinetic energy $1\ m^2 \cdot s^{-2}$, the specific dissipation rate $1\ s^{-1}$, the water x- and y velocities $0\ m \cdot s^{-1}$, the air x- and y-velocities $0\ m \cdot s^{-1}$, and the air volume fraction 0. Then to create the bubble, the patch option was used to assign a volume fraction of 1 to the assigned region of the bubble.

The calculation was then run with a fixed time step, a user-specified method, number of time steps at 25000, a time step size 0.0001, the reporting interval at 1, max iterations per time step of 50, and a profile update interval of 1.

After the simulations finished running, at specific points of flow-time the velocity of water in the vertical direction was extracted at specific points in the column. Depending on the column, either profile plots were extracted at 0.9, 1.1, 1.3, 1.5, 1.7, 1.9, and 2.1 seconds or at 2.3, 2.5, 2.7, 2.9, 3.0, 3.1, and 3.3 seconds. The positions from which the profile plots were extracted were dependent on whether there was a collector present or not. For the simulations without a collector, the positions were at 100, 150, 200, and $250\ mm$. If there was a collector present, the positions were at 100, 150, $175\ mm$ and at the opening of the collector and $5\ mm$ before the top of the column.

CHAPTER 4
RESULTS AND DISCUSSION

4.1. Quantification of Bubble Characteristics

To investigate whether there is a trade-off between particle recovery and bubble quantities in the column, these quantities need to be quantified. This section aims to quantify the bubbles formed in the bubble column, by looking at the bubble size distribution, the trajectories of the bubbles, and the bubble rise velocity. The most important discoveries are highlighted and discussed.

4.1.1. Bubble Size Distribution

Inside the bubble column, three flow regimes occur depending on the superficial gas velocities and the uniformity of the gas distribution [98]. Moreover, the interaction between the rising bubbles and particles influences the flotation, and thus the entrainment process [92]. As the regimes are determined by the gas holdup, which in turn is influenced by the bubble size distributions, and the bubble sizes, the establishment of these two quantities is of great importance to investigate the effect of the bubble size on particle recovery. In the next sections the bubble size distributions, and the Sauter mean diameters of the bubbles at different volume flows, and the influence of different inlet diameters and column diameters will be reviewed.

4.1.1.1. Bubble Sizes in Small Column

Figure 4.1.1 visualizes the bubble size distribution within the small column at different volume flows and different inlet diameters. The R^2-values for the fitted log-normal distributions, and the number of bubbles analyzed can be found in the Appendix. Figure 4.1.1a, 4.1.1b, 4.1.1c display the bubble size distributions inside the column with inlet diameters of 1, 1.5, and 2.5 mm, respectively, at different volume flows. Figure 4.1.1d presents a comparison of the three different inlets at selected volume flows. Depending on the inlet gas volume flow, it is expected that three different regimes occur inside the bubble column. For low volume flows a homogeneous regime characterized by small bubbles and a narrow bubble size distribution is anticipated. At

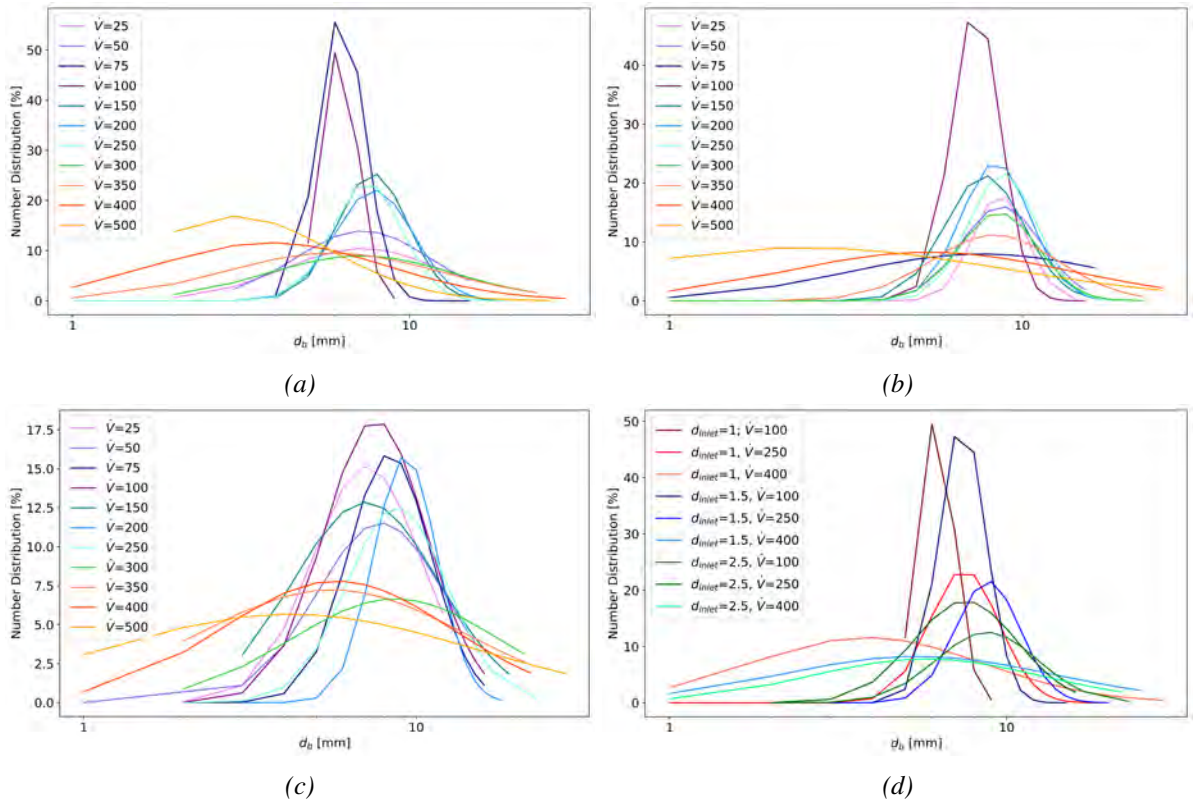

Figure 4.1.1: Log-normal distribution fitted through experimentally obtained bubble chord lengths at different volume flows for the small column for inlet diameters 1 mm (a), 1.5 mm (b), and 2.5 mm (c), and a comparison for selected volume flows at the three different inlet sizes (d). The unit of the volume flow is $cm^3 \cdot min^{-1}$. The R^2 values of the fits can be found in Table A2 in the Appendix.

high volume flows, a heterogeneous regime occurs in which the bubbles can be characterized by larger bubble sizes and broad bubble size distributions. Additionally, a transitional regime is observed between the homogeneous and heterogeneous regime [36, 37, 38].

From Figure 4.1.1a it can be noted that the bubble size distributions at a volume flow of 75 and 100 $cm^3 \cdot min^{-1}$ exhibit similarities. These volume flows yield narrow distributions at roughly equal bubble size. Additionally, the bubble sizes are relatively small. The bubble size distributions at 150, 200, and 250 $cm^3 \cdot min^{-1}$ exhibit similarities to each other as well. However broader distributions are obtained compared to volume flows of 75 and 100 $cm^3 \cdot min^{-1}$. This might suggest that indeed for low volume flows a homogeneous regime is observed with small uniform bubbles. In contradiction, it is notable that at volume flows of 25 and 50 $cm^3 \cdot min^{-1}$ the bubble size distributions display very broad distributions. If the R^2 values of the fits obtained for volume flows smaller than 100 $cm^3 \cdot min^{-1}$ are compared, it is noticed that the R^2 values are above 0.9 for 75 and 100 $cm^3 \cdot min^{-1}$, but smaller than 0.45 for 25 and 50 $cm^3 \cdot min^{-1}$. This indicates that the obtained fit does not describe the bubble size distribution adequately for volume flows 25 and 50 $cm^3 \cdot min^{-1}$. This could indicate that either the dataset of bubbles is not sufficiently large to accurately determine the bubble size distribution, or that at these low volume flows, a homogeneous regime is not observed.

In Figure 4.1.1b again the distribution for a volume flow of 100 is relatively narrow. The distributions at 150, 200, and 250 $cm^3 \cdot min^{-1}$ are again similar, however, you can see a shift to the right, where the bubbles at a volume flow 250 $cm^3 \cdot min^{-1}$ are larger than bubbles at a volume flow of 200 $cm^3 \cdot min^{-1}$, which are again larger than for 150 $cm^3 \cdot min^{-1}$. Here the bubble size distribution at 25 and 50 is noticed to be similar to the bubble size distribution at 300 $cm^3 \cdot min^{-1}$. When increasing the volume flow to 350 $cm^3 \cdot min^{-1}$, the bubble size distribution becomes broader compared to 300 $cm^3 \cdot min^{-1}$. For volume flow of 75 $cm^3 \cdot min^{-1}$ and volume flows exceeding 350 $cm^3 \cdot min^{-1}$ the bubble size distribution displays a very broad distribution, making it nearly impossible to discern a distinct peak.

For Figure 4.1.1c it is evident that all bubble size distributions display a notably broad behavior across various volume flows. However, for volume flows exceeding 300 $cm^3 \cdot min^{-1}$, the bubbles tend to obtain a broader distribution than for lower volume flows.

From Figure 4.1.1d it can be noticed that at equal volume flows, the bubble size increases for larger inlet diameters. Additionally, no clear difference in broadness of bubble size distributions related to the inlet diameter at a given volume flow is noticed.

In Figure 4.1.2 the Sauter mean diameter for different volume flows at different inlet sizes is visualized. For an inlet diameter of 1 mm, almost no change in d_{32} is observed when increasing the volume flow from 25 to 50 $cm^3 \cdot min^{-1}$. Furthermore, an almost linearly decreasing bubble d_{32} can be noticed when increasing the volume flow from 50 to 75, and from 75 to 100 $cm^3 \cdot min^{-1}$. Jamialahmadi et al. (2001) argued that at high volume flows, and low viscosity the effect of surface tension is negligible [41]. Additionally, Kováts, Thévenin, and Zähringer 2020 argued that the bubble size increases with increasing surface tension [56]. The decrease in bubble size from 25 to 100 $cm^3 \cdot min^{-1}$ could therefore indicate that surface tension becomes less important, therefore the bubble size decreases with increasing volume flow. When increasing the volume flow from 150 to 200, and from 200 to 250 $cm^3 \cdot min^{-1}$ there is relatively few change in bubble size. From 250 to 300 $cm^3 \cdot min^{-1}$ the d_{32} increases significantly, and from 300 to 350, from 350 to 400, and from 400 to 500 $cm^3 \cdot min^{-1}$ the size increases little, with increasing the volume flow to 400 $cm^3 \cdot min^{-1}$ having almost no effect on bubble size.

When increasing the volume flow, it is expected that after the homogeneous regime first a transitional regime, and then a heterogeneous regime occurs. Often, two regions are attributed in the transitional regime. In the first region, T1, the global gas hold-up increases more slowly, indicating a change in the flow regime. In the second region, T2, the gas holdup attains a plateau [98]. In Figure 4.1.2 it can be noticed that between 150 and 250 $cm^3 \cdot min^{-1}$ the Sauter mean diameter increases quite slowly, and that between 300 and 400 $cm^3 \cdot min^{-1}$ the Sauter mean diameter remains roughly constant. This suggests that between 150 and 400 $cm^3 \cdot min^{-1}$ the transitional regime occurs, in which bubble size is dependent on coalescence and breakup mechanisms of bubbles. Furthermore, when increasing the volume flow from 400 to 500 $cm^3 \cdot min^{-1}$, an increase in bubble size is observed, which could indicate the transition from a transitional to a heterogeneous regime. The occurrence of a heterogeneous regime is con-

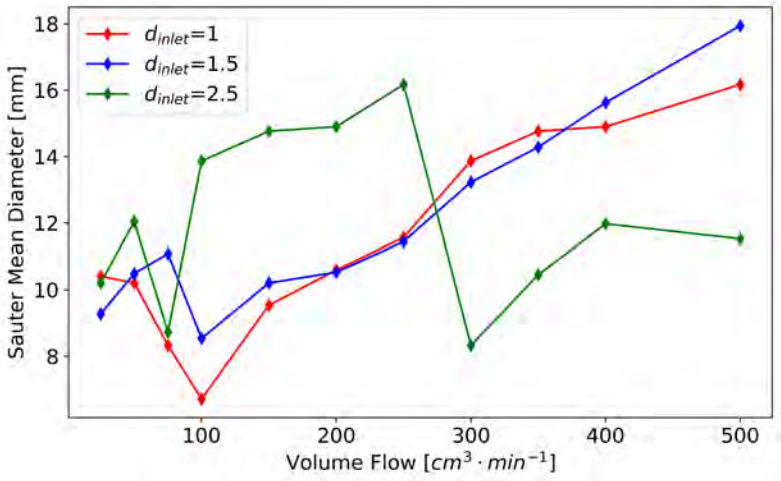

Figure 4.1.2: Sauter mean diameter for bubble size distribution at the middle of the small column for different volume flows, d_{inlet} in mm.

firmed by the broad bubble size distributions found in Figure 4.1.1a. In the heterogeneous regime the bubble size distribution is dominated by coalescence and breakup processes [44]. Large and small bubbles co-exist, resulting in the broad distribution that is obtained. This is confirmed by Hur et al. (2013). They argued that a high gas flow rate influenced the fluid behavior around the orifice, by often generating a turbulent flow around the orifice which affects bubble detachment, coalescence and breakup [39]. Increasing the volume flow, thus transforms the flow regime in the column from a homogeneous towards a heterogeneous regime.

For an inlet diameter of 1.5 mm, an increase in d_{32} is seen when increasing the volume from from 25 to 75 $cm^3 \cdot min^{-1}$, and again a decrease in d_{32} for a volume flow of 100 $cm^3 \cdot min^{-1}$. Furthermore, when increasing the volume flow from 100 until 500 $cm^3 \cdot min^{-1}$, an almost linear relation between flow rate and Sauter mean diameter is noticed.

For an inlet diameter of 2.5 mm, a profound increase in d_{32} is noticed when increasing the volume flow from 25 to 50 $cm^3 \cdot min^{-1}$, a large decrease going from 50 to 75 $cm^3 \cdot min^{-1}$, and again a large increase from 75 to 100 $cm^3 \cdot min^{-1}$. Then between 100 and 200 $cm^3 \cdot min^{-1}$ the bubble size is relatively constant, before increasing again when increasing the volume flow to 250 $cm^3 \cdot min^{-1}$. A large decrease in bubble diameter is then observed when increasing the volume flow to 300 $cm^3 \cdot min^{-1}$, before the bubble size increases again when increasing the volume flow further.

When comparing the bubble sizes for the different inlet sizes, it is observed that a larger inlet diameter generally results in a larger bubble size. Jian, Zhu, and Li (2017) argued that when a bubble is formed, a gas neck occurs that continuously thins to a thread that pinces off into two parts due to the Kelvin-Helmholtz instability [42]. If it is assumed that the neck has to be thinned to a critical diameter d_c that is independent of inlet diameter. Then the time of thinning would increase for a larger inlet size, since it would take longer to thin from a larger inlet diameter towards the critical diameter. While the thinning occurs, gas is continuously injected into the bubble, resulting in a

larger bubble size. This is confirmed by research done by Hur et al. (2013), who noticed an increase in bubble size with an increase in orifice size. They argued that larger orifice sizes increased the detachment period based on the changes in gas momentum transfer and surface tension [39].

Additionally, Hur et al. (2013) showed that the transitional regime is induced by the orifice diameter [39]. In Figure 4.1.1b it can be observed that the distribution of bubble sizes broadens quicker with volume flow compared to Figure 4.1.1a. This could indicate that increasing the inlet diameter increases turbulence in the bubble column. This will in turn decrease the volume flow at which the transitional and heterogeneous regime occur. Figure 4.1.1c confirms this suggestion, since the bubble size distributions tend to be much broader for each volume flow compared to the bubble size distributions in Figure 4.1.1a.

4.1.1.2. Bubble Sizes in Large Column

It is expected that the wall of the column will have impact the bubble size and bubble size distributions. Therefore, a bubble size distribution was obtained in the large column that can be compared to the bubble size distribution in the small column. Figure 4.1.3 depicts the bubble size distribution in the large column. Figure 4.1.3a displays the bubble size at different volume flows, and in Figure 4.1.3b bubble size distributions in the large and the small column can be compared for selected volume flows.

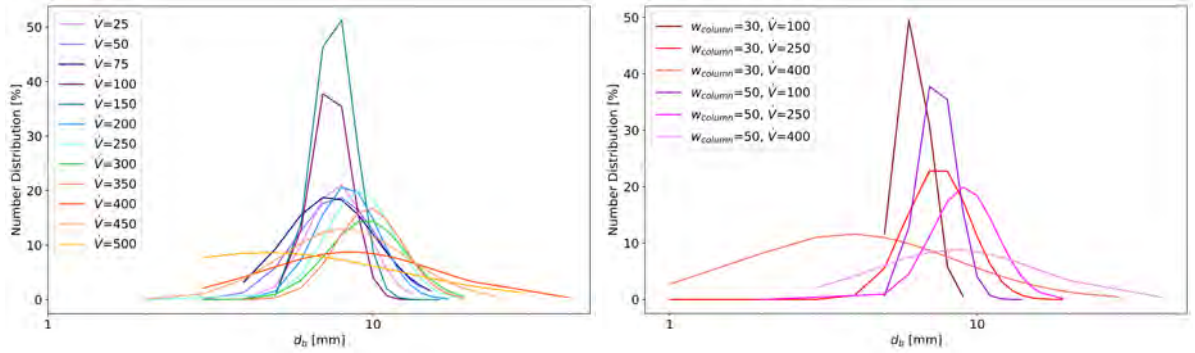

(a) *(b)*

Figure 4.1.3: Log-normal distribution fitted through experimentally obtained bubble chord lengths at different volume flows for the large column with an inlet diameter of $1\ mm$ *(a), and for selected volume flows for the large and the small column ith an inlet diameter of* $1\ mm$ *(b). The unit of the volume flow is* $cm^3 \cdot min^{-1}$*. The* R^2 *values of the fits can be found in the Appendix.*

In Figure 4.1.3a it is notable that for volume flows of 25, 50, and $75\ cm^3 \cdot min^{-1}$ a similar shape in bubble size distribution is obtained. Furthermore, when increasing the volume flow to 100 or $150\ cm^3 \cdot min^{-1}$ the bubble size distribution becomes much narrower. At 100 and $150\ cm^3 \cdot min^{-1}$ the distributions are of similar shape, and a peak around $d_b = 8\ mm$ is observed. Furthermore, for volume flows of 200 and $250\ cm^3 \cdot min^{-1}$ the distribution is similar, and comparable to distributions at a volume flow of 25, 50, and $75\ cm^3 \cdot min^{-1}$. However, a shift to the right for $250\ cm^3 \cdot min^{-1}$ compared to $200\ cm^3 \cdot min^{-1}$ can be noticed. When increasing the volume flow to 300

and $350\ cm^3 \cdot min^{-1}$, distributions that have a similar shape are obtained.Iincreasing the volume flow further to 400, 450, and $500\ cm^3 \cdot min^{-1}$, the bubble size distribution becomes much broader.

In Figure 4.1.3b it becomes evident that generally smaller bubble sizes are obtained when increasing the column diameter. For lower volume flows again a narrower distribution is derived compared to higher volume flows. For all selected volume flows, a clear decrease in bubble size when increasing the width of the bubble column is seen.

The decrease in bubble size is confirmed by the Sauter mean diameter displayed in Figure 4.1.4 for different volume flows in the middle of the column for the large column with an inlet diameter of 1 mm. Here again the decrease in bubble size is noticed when decreasing the volume flow from 75 to $100\ \ cm^3 \cdot min^{-1}$. Furthermore, there is no profound change in bubble size when increasing the volume flow from 100 to $150\ \ cm^3 \cdot min^{-1}$. Between 150 to $300\ \ cm^3 \cdot min^{-1}$ again an almost linear increase of bubble size to volume flow is observed. Then, from 300 to $350\ \ cm^3 \cdot min^{-1}$ no big change is noticed in bubble size, however, from 350 to $400\ \ cm^3 \cdot min^{-1}$ the bubble size increases significantly, before decreasing again when increasing the volume flow to $450\ \ cm^3 \cdot min^{-1}$, and increasing again when increasing the volume flow to $500\ \ cm^3 \cdot min^{-1}$.

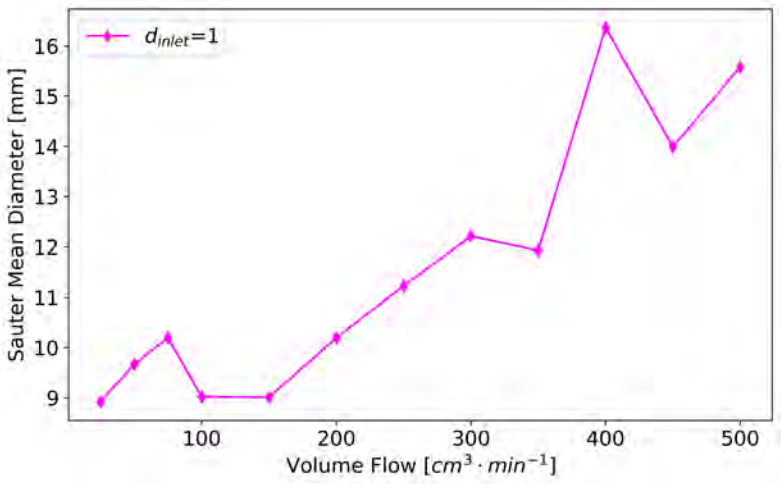

Figure 4.1.4: Sauter mean diameter for bubble size distribution at the middle of the large column for different volume flows, d_{inlet} in mm.

The decrease in bubble size in Figure 4.1.4 in the large column can be explained due to vigorous liquid motions and turbulent circulations that are developed in the large column [36]. This might influence bubble break-up mechanisms, resulting in smaller bubbles in the large column. Additionally, the volume fraction of the gas is smaller in the large column, hence the number density of bubbles in the large column is smaller than in the small column. This would mean that less bubbles encounter each other, which would decrease the number of times coalescence of bubbles occurs, therefore decreasing the bubble size.

Ruzicka et al. (2001) argued that the column size has an adverse effect on the homogeneous regime stability, and thus advances the flow regime transition [36]. In Fig-

ure 4.1.3a it can be recognized that at a volume flow of 100 and $150\ cm^3 \cdot min^{-1}$ a narrower distribution is obtained compared to 75 and $100\ cm^3 \cdot min^{-1}$. This would contradict the findings of Ruzicka et al. (2001), since this would result in a more stable homogeneous regime for higher volume flows when increasing the column diameter. However from Figure 4.1.4, it can be argued that three transitional regimes occur. The first transitional regime occurs between 75 and $150\ cm^3 \cdot min^{-1}$, the second transitional regime from 150 to $300\ cm^3 \cdot min^{-1}$, and the third transitional regime for volume flows larger than $300\ cm^3 \cdot min^{-1}$.

Inaccuracies between the obtained Sauter mean diameter and the bubble size distributions could be caused by the log-normal distribution used to describe the bubble size distribution. From the R^2 values in the Appendix, it can be noticed that the R^2 value is not adequately high for each fit that is obtained. This would suggest that the log-normal distribution does not describe the bubble sizes accurately for each condition tested. This is confirmed in Figure A5 in the Appendix, in this case, the distribution shows a two-peaked distribution rather than a one-peak distribution. A similar observation was done for other, but not all conditions. This suggests either random variation in bubble size distributions that are not a function of the volume flow, or that the datasets of bubbles measured should be increased to accurately determine the bubble size distributions.

There are some drawbacks that should be noted for the bubble size analysis. Firstly, the bubble sizes for a single bubble are much more difficult to determine for high volume flows. At higher volume flows the bubbles are affected more by the wake of preceding bubbles, which could result in bubbles accelerating and colliding into the preceding bubbles. This collision then results in bubble aggregates, which may be segregated in a short time if the collision momentum energy is not sufficient for bubble coalescence [39]. If these aggregates of bubbles are captured in the image, it is very difficult to analyze the bubble sizes separately. Furthermore, the clustering of bubbles might have an effect on the flow inside the column, since they could behave as one big bubble, or they could experience negative forces when moving, altering their shape and velocity. Additionally, in the bubble size analysis it was assumed that the bubble could be assumed to be an ellipsoid. This might not be the best analogy for all bubbles, since the bubbles in the bubble column experience deformations due to the forces acting on the bubbles. Lastly, for each condition between 82 and 164 bubbles have been analyzed. For a more accurate prediction of the bubble sizes in the column, this should be increased, to make sure an accurate distribution of bubbles have been analyzed.

It should be noted that particles might influence the bubble size distribution inside the column. Orvalho et al. (2018) showed that for low concentrations of particles the homogeneous regime might be stabilized, whereas for higher concentrations of particles the homogeneous regime was destabilized [37]. The bubble size distributions were determined when no particles were present in the bubble column. Therefore, the effect of particles on the bubble size distribution should be investigated further.

4.1.1.3. Bubble sizes at Formation

To compare the bubble size distribution of the bubbles at formation with the middle of the column, images were analyzed at the bottom of the column. The graphs displaying bubble size distribution and the Sauter mean diameter can be found in the Appendix. From these graphs it can be noticed that generally the bubble size distribution is much broader at formation than after some displacement, and there is no correlation between Sauter mean diameter and volume flow. However, the analysis has been done for in between 12 and 66 bubbles, so the analysis of more bubbles is needed for an accurate prediction.

4.1.2. Bubble Trajectories

The trajectory of the bubble is dependent on the size of the bubble. In Figure 4.1.5 the trajectories of ten bubbles at different conditions is displayed. Figures 4.1.5a, 4.1.5b, and 4.1.5c represent the bubble trajectories for the small column with inlet diameter of $1\ mm$ for volume flows of 100, 300, and $500\ cm^3 \cdot min^{-1}$, respectively. From these figures it can be noticed that for higher volume flows, the path of the bubbles experiences more deviation than for lower volume flows. The trajectories of the bubbles at $100\ \ cm^3 \cdot min^{-1}$ are more straight, but still experience a zigzag motion. At $300\ \ cm^3 \cdot min^{-1}$ the bubbles tend to move to the right-hand side, with a zigzag motion. For $500\ \ cm^3 \cdot min^{-1}$ the bubbles experience a motion to the left-hand side, while experiencing a zigzag motion.

Figures 4.1.5d, 4.1.5e, and 4.1.5f display the trajectories of the bubbles in the small column with an inlet diameter of $1.5\ mm$ for volume flows of 100, 300, and $500\ \ cm^3 \cdot min^{-1}$ respectively. Again a zigzag motion of the bubbles is seen, for which the path deviates the most for higher volume flows. Additionally, the same pattern can be observed for an inlet diameter of $2.5\ mm$, which are displayed in Figures 4.1.5g, 4.1.5h, and 4.1.5i.

The trajectories of ten bubbles for a volume flow of 300, 400, and $500\ \ cm^3 \cdot min^{-1}$ in the large column are visualized in Figures 4.1.5j, 4.1.5k, and 4.1.5l respectively. Here it can be recognized that the trajectories deviate more on the horizontal axis for the bubbles at a volume flow of 100 and 500 than for $400\ \ cm^3 \cdot min^{-1}$.

When comparing the trajectories of the large and the small column, the bubbles deviate more in the large column than in the small column. This is probably due to the bubbles traveling between the walls, and since the large column is wider, the bubbles deviate more from their point of formation than for the small column.

From literature, it is expected that small bubbles move in a straight line, whereas bigger bubbles experience a zigzag, helical or spherical motion, depending on their size. Overall, all bubbles experience a kind of zigzag pattern. The motion of the bubbles could be helical or spherical, but since videos were taken in 2D this is not visible using this tracking technique. To really understand the motion of the bubbles, different techniques need to be used to visualize the exact shape of their motion.

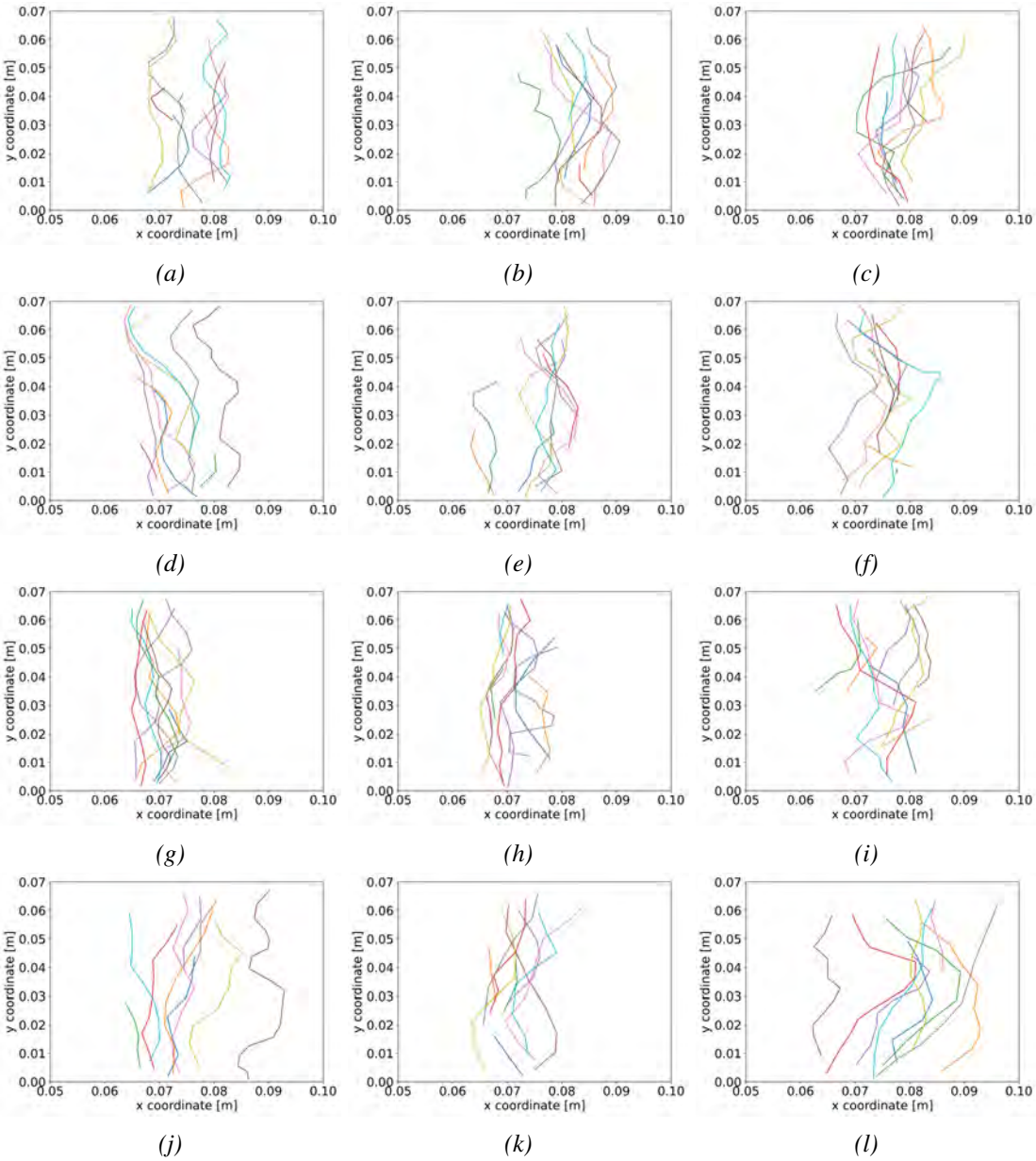

Figure 4.1.5: Trajectories of ten bubbles in the small column with inlet diameter $1\ mm$ *at volume flow* 100 *(a),* 300 *(b), and* $500\ cm^3 \cdot min^{-1}$ *(c), small column with inlet diameter* $1.5\ mm$ *at volume flow* 100 *(d),* 300 *(e), and* $500\ cm^3 \cdot min^{-1}$ *(f), small column with inlet diameter* $2.5\ mm$ *at volume flow* 100 *(g),* 300 *(h), and* $500\ cm^3 \cdot min^{-1}$ *(i), and large column with inlet diameter* $1\ mm$ *at volume flow* 300 *(j),* 400 *(k), and* $500\ cm^3 \cdot min^{-1}$ *(l).*

4.1.3. Bubble Rise Velocity

To further characterize the flow conditions inside the bubble column, the bubble rise velocity was experimentally determined and compared with different models. The average velocity determined in the small and the large column with their corresponding Reynolds' numbers is shown in Figure 4.1.6. Here it can be noticed that the velocity is highest for bubbles in the large column, then for bubbles in the small column with an inlet of $1.5\ mm$, then for bubbles with an inlet of $2.5\ mm$, and slowest for bubbles in the

small column with an inlet of $1\ mm$. One reason why the bubble rise velocity is higher in the large column compared to the small column might be due to the bubbles in the small column experiencing a downward force due to shear stress at the wall. Another reason could be due to turbulent circulations in the large column [36]. The turbulent circulations could accelerate the bubble rise velocity of the bubbles in the large column compared to the small column. For each condition, the bubble rise velocity increases with increase of volumetric gas rate. When increasing the volumetric gas rate, the flow in the bubble column transitions from the homogeneous to the heterogeneous regime. In the homogeneous regime, the bubble rise velocity solely depends on the small bubbles encountered in the homogeneous regime, whereas in the heterogeneous regime both small and large bubbles account for the average bubble rise velocity [44]. Additionally, small bubbles in the heterogeneous regime can be entrained in the wake of the larger bubbles, resulting in an acceleration of its bubble rise velocity [55], which in turn increases the average bubble rise velocity in the column.

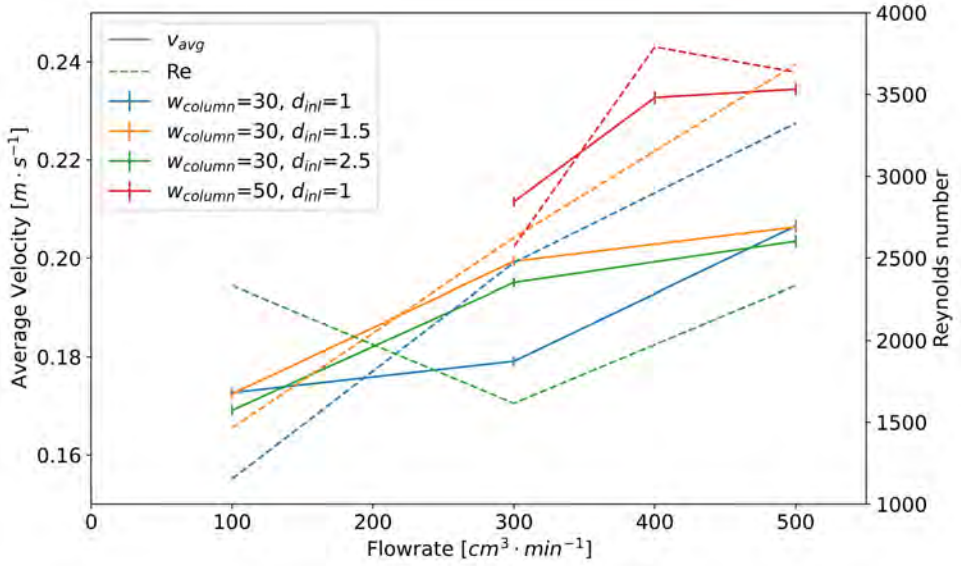

Figure 4.1.6: Experimentally determined velocity and Reynolds number for small and large column at different volume flows.

The Reynolds number is dependent on the bubble size and the bubble velocity. As was noticed previously, the bubble size is not linearly dependent on the gas flow rate. Therefore, the Reynolds number does not follow the exact trend as the bubble rise velocity. The Reynolds numbers for each condition are between 1000 and 4000, suggesting that the motion of the bubbles is dominated by inertial forces and that viscous forces can be neglected. For Reynolds numbers between 20 and 4700, it is expected that the bubbles move in an ellipsoidal regime [52].

From Figure 4.1.6 it can be noticed that the uncertainty in the experimentally determined velocity is expected to be small. However, the uncertainty was determined for a single bubble, differently sized and shaped bubbles could result in a higher deviation in bubble rise velocity. Additionally, for the determination of the Reynolds number, the Sauter mean diameter was used. The uncertainty in bubble size was therefore not

included, since there is no straightforward way to determine the uncertainty in the Sauter mean diameter. However, especially at larger volume flows the bubble size distribution obrained was very broad. So it is expected that the uncertainty is quite large.

Figure 4.1.7 shows a comparison of the experimentally determined average bubble rise velocity in the small and the large column for different inlet diameters and different volume flows with existing models. The models used are displayed in Equations 2.19, 2.27, 2.26, 2.20, and 2.23. It can be noticed that the models developed by Park et al. (2017) [53], and Chavez et al. (2021) [19], highly overestimate the bubble rise velocity. The overestimation of Park et al. (2017) can be explained since they investigated the bubble rise velocity of bubbles in a liquid pool and thus did not include the effect of the wall [53]. Friction at the wall could result in a decrease in the bubble rise velocity. The correlation proposed by Chavez et al. (2021) was originally developed for Reynolds numbers between 455 and 598 [19]. The Reynolds numbers encountered in the bubble column exceed this value significantly, which could result in the deviation of bubble rise velocity from the correlation. The correlations proposed by Clift, Grace, and Weber (1978) [59], Islam et al. (2013) [54] and Krishna et al. (1999) [55] describe the experimentally determined bubble rise velocity reasonably well. The correlation proposed by Clift, Grace, and Weber (1978) again does not take into account the effect of the wall, which could result in the noticed deviation [59]. The correlation proposed by Islam et al. (2013) was tested for bubbles in a size range of $3 - 5\ mm$ [54], whereas in this study most bubbles are much larger than that. Therefore, this could explain the decrease in bubble rise velocity for larger bubbles compared to small bubbles, as this correlation does not accurately describe the bubble rise velocity for large bubbles. Lastly, the correlation proposed by Krishna et al. (1999) shows the best estimation of the bubble rise velocity in both the small column as the large column. However, Krishna et al. (1999) proposed an additional factor that accounts for the acceleration in bubble rise velocity due to the interaction of the bubble with the wake of the bubble preceding it [55]. When adding this factor into the model, the model again highly overestimates the bubble rise velocity. This would suggest either that the bubbles do not experience the effect of the wake of the preceding bubble, or that the correlation needs to be altered, since it was not developed for the exact conditions found in this column.

From the different models used for comparison, it is generally the case that bubble rise velocity increases with bubble size. If Figure 4.1.7 and Figures 4.1.2, and 4.1.4 are compared, it can be noticed that only for an inlet of 1.5 mm this pattern is observed. However, the experimentally determined bubble rise velocity and bubble equivalent diameter are averages. Hence, this could result in loss of information, and therefore the dependency of the bubble rise velocity on the bubble diameter is not accurately depicted. Therefore, to determine the bubble rise velocity with the bubble size, an experiment should be carried out where the bubble size can be linked to the bubble rise velocity in a more explicit manner.

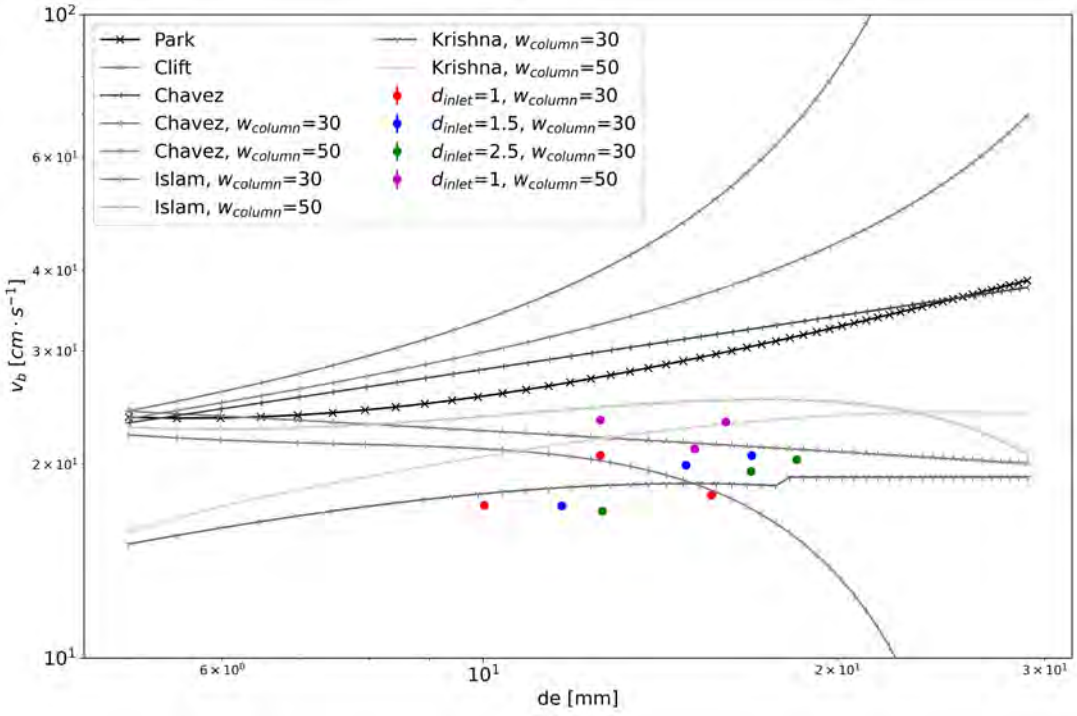

Figure 4.1.7: Experimentally determined average bubble rise velocity compared to different developed models.

4.1.4. Dimensionless numbers

To characterize the flow in the bubble column, some dimensionless numbers have been defined from the experimentally determined bubble rise velocity. These numbers are depicted in Table 4.1.

Table 4.1: Dimensionless numbers for bubbles under different conditions.

$\dot{V}$ $[cm^3 \cdot min^{-1}]$	w_{column} $[mm]$	d_{inlet} $[mm]$	d_e $[m]$	v_b $[m \cdot s^{-1}]$	Re	Eo	We	Mo	Ar
100	30	1	0.0100	0.173	1723.2	13.48	4.090	$2.563 \cdot 10^{-11}$	$9.776 \cdot 10^{6}$
300	30	1	0.0156	0.179	2786.8	32.78	6.859	$2.563 \cdot 10^{-11}$	$3.707 \cdot 10^{7}$
500	30	1	0.0126	0.207	2585.7	21.22	7.338	$2.563 \cdot 10^{-11}$	$1.931 \cdot 10^{7}$
100	30	1.5	0.0117	0.172	2003.3	18.27	4.747	$2.563 \cdot 10^{-11}$	$1.543 \cdot 10^{7}$
300	30	1.5	0.0149	0.199	2951.6	29.68	8.085	$2.563 \cdot 10^{-11}$	$3.194 \cdot 10^{7}$
500	30	1.5	0.0169	0.206	3474.1	38.39	9.850	$2.563 \cdot 10^{-11}$	$4.698 \cdot 10^{7}$
100	30	2.5	0.0126	0.169	2125.9	21.40	4.940	$2.563 \cdot 10^{-11}$	$1.955 \cdot 10^{7}$
300	30	2.5	0.0169	0.195	3279.5	38.28	8.790	$2.563 \cdot 10^{-11}$	$4.678 \cdot 10^{7}$
500	30	2.5	0.0185	0.203	3740.5	45.78	10.46	$2.563 \cdot 10^{-11}$	$6.117 \cdot 10^{7}$
300	50	1	0.0151	0.211	3184.7	30.71	9.254	$2.563 \cdot 10^{-11}$	$3.361 \cdot 10^{7}$
400	50	1	0.0161	0.233	3725.9	34.71	11.91	$2.563 \cdot 10^{-11}$	$4.039 \cdot 10^{7}$
500	50	1	0.0126	0.234	2934.7	21.22	9.453	$2.563 \cdot 10^{-11}$	$1.931 \cdot 10^{7}$

As mentioned above, inside the column high Reynolds numbers occur, indicating the

dominance of inertial forces over viscous forces. The Reynolds number, together with the Eotvos and Morton numbers, can be used to characterize the hydrodynamic conditions of the body motion in a fluid. Here, the Eotvos and Morton number describe the shape of the bubble moving in the surrounding fluid. Since the Eotvos number is quite high, this indicates a slight dominance of gravitational forces compared to surface tension [19]. As indicated in yellow in Figure 4.1.8, the Reynolds, Eotvos, and Morton number indicate that the bubbles experience a wobbling to spherical-cap shape.

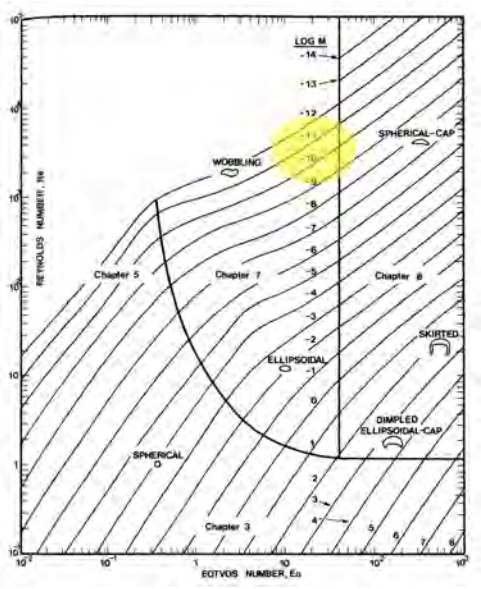

Figure 4.1.8: Dimensionless numbers with respect to Clift regime map [59].

The Weber number is the ratio between the inertial forces and the surface tension [19]. Since the Weber number is quite high, this indicates a slight dominance of inertial forces over surface tension. Jamialahmadi et al. (2001) argued that at high volume flows surface tension is negligible [41]. However, dimensionless analysis suggests that in the bubble column used in the experiments, surface tension can be neglected even for low volume flows. Lastly, the Archimedes number describes the ratio between the gravitational and viscous forces. Since $Ar \gg 1$, natural convection dominates in the bubble column. This is as anticipated, as the rising of the bubbles is expected to occur due to density differences, rather than any form of external mechanism.

4.2. Particle Behavior in Bubble Column

To investigate the bubble-induced particle behavior, velocity profiles of glass hollow spheres, zinc-oxide and nickel particles are compared. First, the velocity distribution of the glass hollow spheres is discussed. Afterwards, the velocity profiles in the small and the large column. Lastly, dimensionless analysis of the particles inside the bubble column is considered.

4.2.1. Bubble Induced Velocity Profiles in Water

To be able to compare the particle behavior of zinc-oxide and nickel particles, the velocity profiles induced by the bubbles were investigated by using glass beads. The obtained velocity profiles of the glass beads are depicted in Figure 4.2.1.

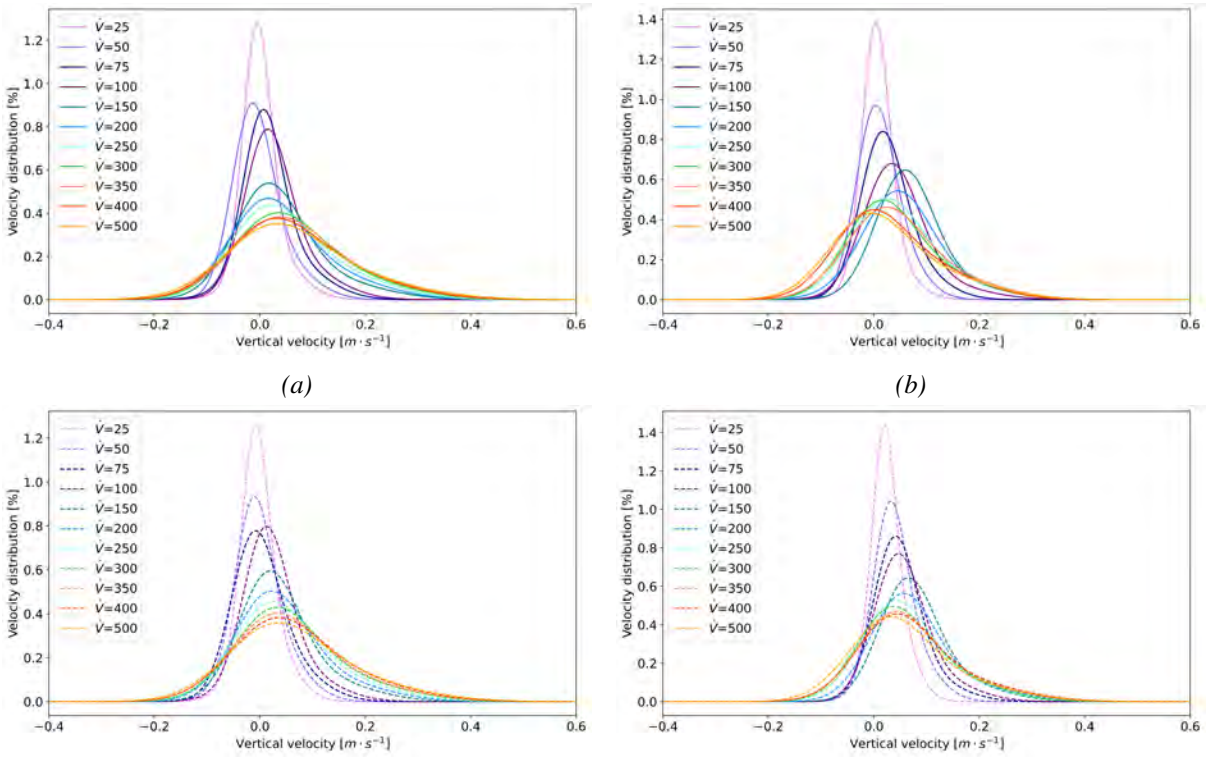

Figure 4.2.1: Velocity profiles in vertical direction for glass hollow spheres with inlet size of 1 mm in diameter, for small column (a), and large column (b) with no collector, and with collector with opening diameter of $7.5\ mm$ *and angle* $60°$ *for the small column (c) and the large column with collector with opening diameter* $10\ mm$ *and angle* $61.9°$ *(d).*

Figures 4.2.1a and 4.2.1c show velocity profiles of glass beads in the small column for different volume rates with no collector, and the collector with a $7.5\ mm$ opening and angle of $60°$, respectively. It can be seen that for higher volume flows a broader velocity distribution is obtained, which is confirmed by the increase in FWHM for increasing volume flows, see Figure 4.2.2a. This could again indicate the transition

from a homogeneous to a heterogeneous regime. At low volume flows, a homogeneous regime occurs, for which bubbles are of equal size. Therefore, the glass beads experience a narrow distribution of velocity of the fluid induced by the bubbles. The lift of the glass beads is therefore uniform, which results in a narrow distribution. When increasing the volume flow the homogeneous regime transitions to a heterogeneous regime. In the heterogeneous regime the bubbles can be characterized by a churn-turbulent regime and both large and small particles coexist. The bubble rise velocity is thus much broader, which results in a much broader glass bead velocity distribution. It is noticed that for the small column for volume flows of 25, 50, 75, and $100\ cm^3 \cdot min^{-1}$ the velocity distribution is narrow, which could indicate the homogeneous regime. For the velocity distributions for volume flows of 150, 200, and $250\ cm^3 \cdot min^{-1}$ the velocity profiles are quite similar, but much broader than for the lower volume flows. When increasing the volume flow from 300 until $500\ cm^3 \cdot min^{-1}$ the velocity distribution broadens again further. This could indicate that the transitional regime occurs between 150 and $250\ \ cm^3 \cdot min^{-1}$ and the heterogeneous regime from $300\ \ cm^3 \cdot min^{-1}$ onward. For the large column, the velocity distributions of the glass beads are depicted in Figures 4.2.1b and 4.2.1d. In Figure 4.2.1b no collector was present in the column, whereas in Figure 4.2.1d a collector with opening diameter of $10\ mm$ and angle of $61.9°$, was placed into the column. The velocity distributions are similar for volume flows of 25 and $50\ cm^3 \cdot min^{-1}$, for 250 and $300\ cm^3 \cdot min^{-1}$, and for 400 and $500\ cm^3 \cdot min^{-1}$. The reason that the three regions cannot be as easily distinguished could be because of turbulent flow induced in the large column. Therefore, the transitional region could be encompassed of multiple regions, resulting in varying velocity distributions.

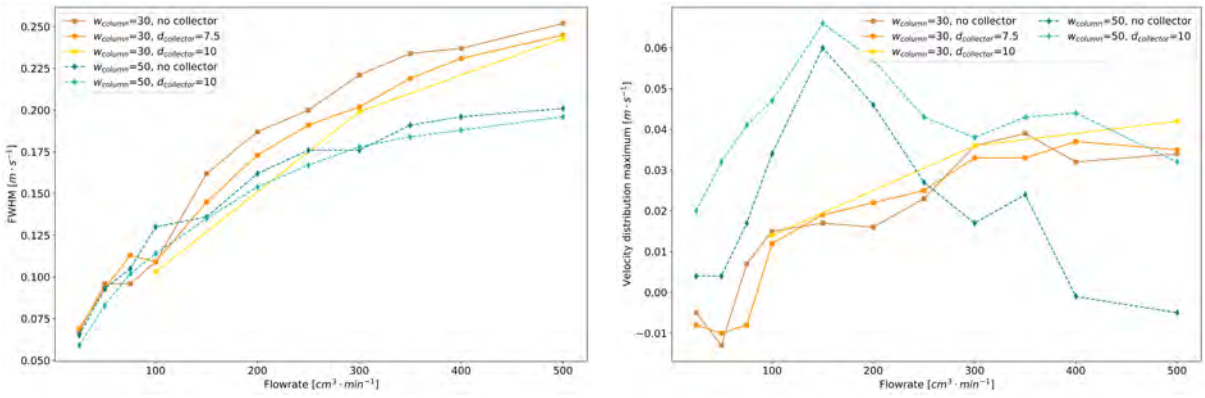

(a) *(b)*

Figure 4.2.2: FWHM of velocity distributions for glass hollow spheres (a) and velocity distribution maximum for LDA velocity profiles (b) in Figure 4.2.1.

When increasing the volume flow, the velocity distribution is noticed to shift to the right for the small column, resulting in a higher velocity at the maximum of the distribution. This indicates that for higher volume flows, a higher bubble rise velocity in the bubble column is obtained. Additionally, at the velocity distribution maximum it can be noticed that different transitions might occur, since the velocity does not increase linearly when increasing the volume flow, but rather experiences regions of constant

velocity. For the large column it can be noticed that when increasing the volume flow, the velocity at the peak decreases. This could be due to the increased bubble rise velocity. When two bubbles approach each other with a too high velocity, they bounce off of each other rather than coalesce into a single bubble [58]. The bouncing off of the bubbles could result in a negative velocity, which could in turn influence the particles.

For the small column no significant difference in velocity distributions when adding the collector on the top of the column is noticed. This is also true for the collector with opening diameter of 10 mm, and angle 64.7°, see Figure A6 in the Appendix. Furthermore, in Figures 4.2.2a and 4.2.2b the FWHM and velocity at the peak for the different conditions are depicted. Here it can be seen that there is no significant difference between the FWHM and the velocity at the peak for the different flow profiles.

From Figure 4.2.2a it can be observed that the FWHM does not differ significantly when adding the collector to the large column. However, from Figure 4.2.2b it is noticed that adding the collector does shift the velocity at the peak quite a bit. For higher volume flows, adding the collector results in a shift from a negative velocity towards an upwards velocity. This could suggest that the collector stabilizes the fluid streamlines, resulting in the particles experiencing an upwards movement rather than a downwards movement.

4.2.2. Vertical Velocity Zinc-oxide and Nickel Particles

To compare particle lift between zinc-oxide and nickel particles, experiments were carried out in the small column at a volume flow of $100\ cm^3 \cdot min^{-1}$. Particle recovery at higher volume flows have been carried out by Dr. Ir. Ruben Dewes, from which additional information was obtained. Furthermore, particle lift in the large column was compared for differently sized nickel particles at high volume flows. The next sections will discuss the results obtained from these experiments.

4.2.2.1. Small Column

To test the limits of particle lift, the velocity profiles of both zinc-oxide and nickel particles with a size range of $500\ nm$ up to $10\ \mu m$ were measured in the small column for three inlet diameters. The results for an inlet diameter of $1\ mm$ are depicted in Figure 4.2.3. From this Figure it can be seen that there are no significant differences in the velocity profiles of the different particles. This is highlighted by Figure 4.2.4. Here Figure 4.2.4a depicts the FWHM of the velocity profiles for the different particles, and 4.2.4b the velocity at the maximum of the velocity distribution. The standard deviation of the FWHM is around 0.4%, which indicates that there is indeed no big difference between the FWHM values. Furthermore, the velocity at the maximum does not deviate much. Additionally, the velocity distributions in Figure 4.2.3 of the different particles do not show significant difference from the velocity distribution of the glass beads. This indicates that all particles follow the fluid streamlines that are induced by the bubbles. This would suggest that particle lift is independent of particle size and density.

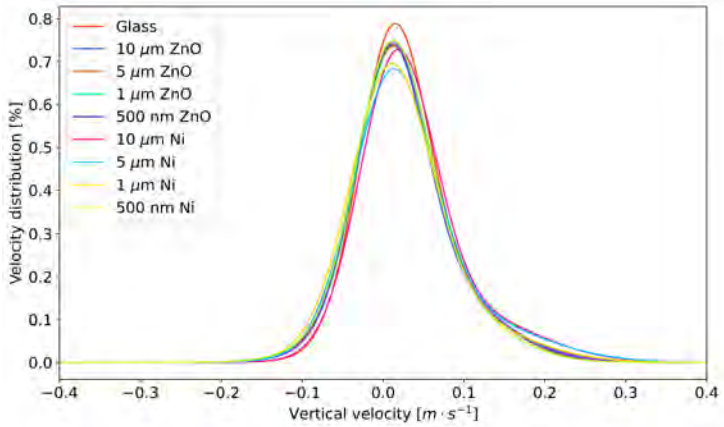

Figure 4.2.3: Velocity profiles in vertical direction in small column with inlet diameter of $1\ mm$ *for different particles with volume flow of* $100\ \ cm^3 \cdot min^{-1}$.

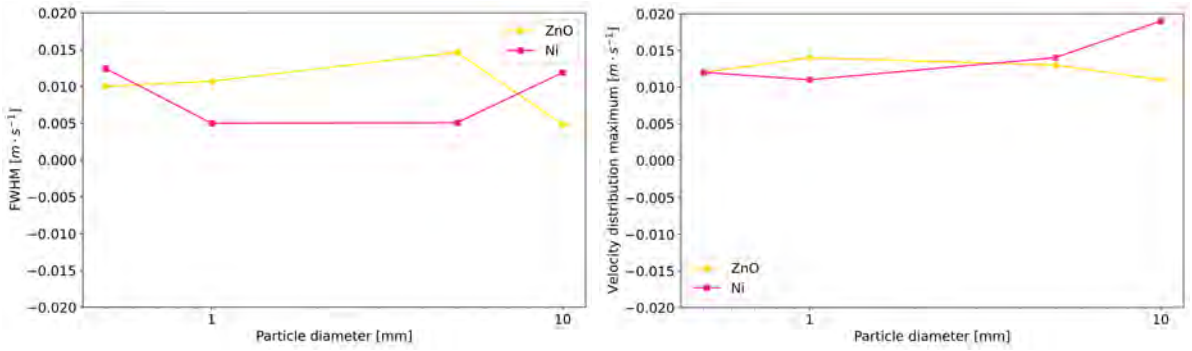

(a) *(b)*

Figure 4.2.4: FWHM (a) and velocity at maximum of velocity distribution (b) at a volume flow of $100\ \ cm^3 \cdot min^{-1}$ *for an inlet of* $1\ mm$ *in Figure 4.2.3.*

When increasing the inlet diameter to 1.5 and $2.5\ mm$, there is again no big difference between the velocity distributions obtained for the different particles and the glass beads. The Figures A7a for $1.5\ mm$ and A7b for $2.5\ mm$ can be found in the Appendix. It is noticed that for a bigger inlet diameter, the FWHM decreases slightly. This indicates a narrower velocity distribution for larger inlet sizes. In addition, the velocity at the peak decreases for larger inlet sizes as well. An increase in bubble size for the larger inlet diameter is observed. This might suggest that less bubbles are formed for larger inletsizes. When less bubbles are formed, there are less bubbles that affect the particles. This could result in a more uniform velocity distribution of the particles, and a lower velocity at the maximum of the distribution, since the particles experience less difference in fluid streamlines. Therefore, a smaller inlet size has a bigger impact on particle lift, which could result in higher particle recovery.

To investigate whether particle behavior changes over time during particle recovery, measurements were done after 5, 20, 35, and 50 minutes of operation time. The results are depicted in Figure 4.2.5. In Figure 4.2.5a you see the velocity profiles for a volume flow of 100 and $200\ \ cm^3 \cdot min^{-1}$ for $1\ \mu m$ of Nickel particles in the small column with an inlet diameter of $1\ mm$. Together with the FWHM in Figure 4.2.5b and velocity at

the peak in Figure 4.2.5c, it is evident that the velocity profile does not change significantly over time. Furthermore, it can be noticed that again for higher volume flows, the velocity distribution broadens and that the velocity at the peak increases.

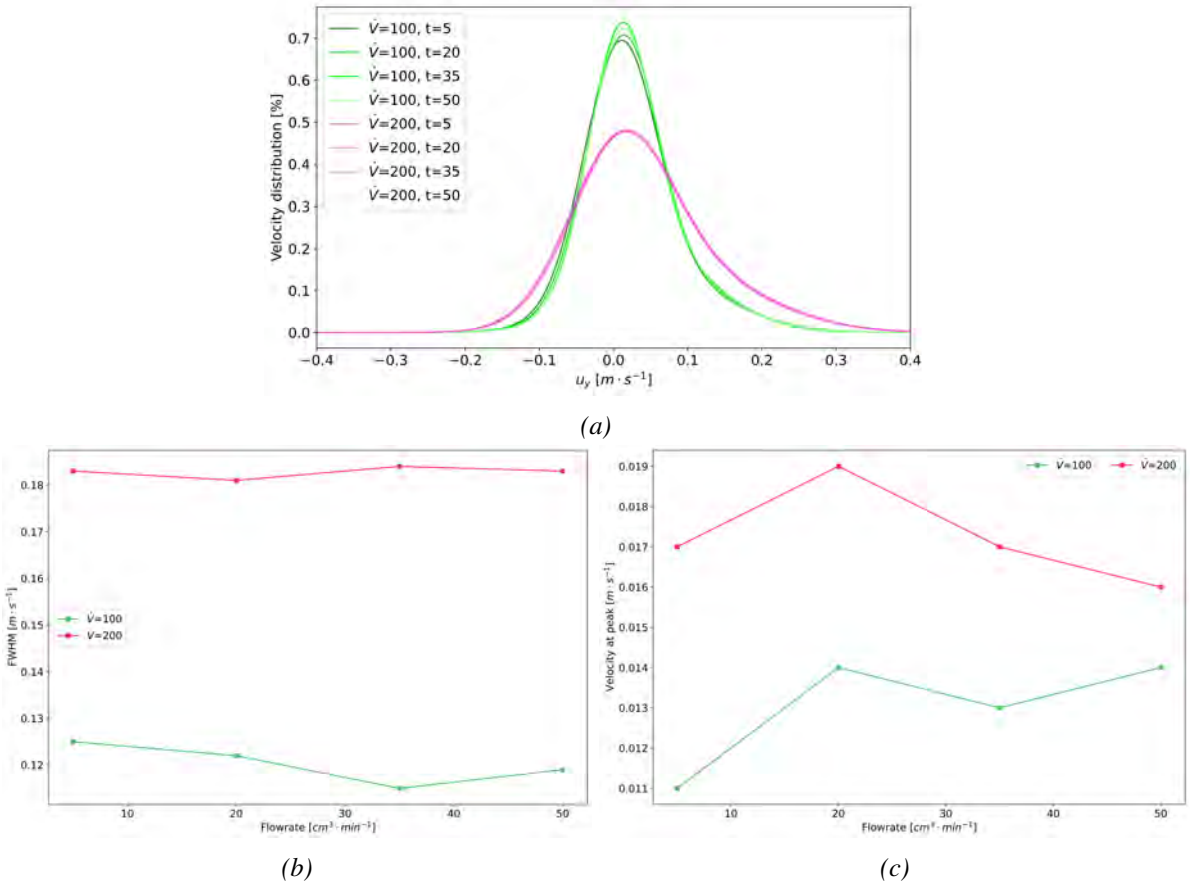

Figure 4.2.5: Velocity distribution in vertical direction (a) and corresponding FWHM (b) and maximum of velocity distribution (c) with inlet diameter of $1\ mm$ *for* $1\ \mu m$ *nickel particles with volume flow of* $100\ \ cm^3 \cdot min^{-1}$ *and* $200\ \ cm^3 \cdot min^{-1}$ *over time.*

4.2.2.2. Large Column

To investigate particle behavior in the large column, LDA profiles were obtained at different volume flows. Figure 4.2.6 depicts the velocity profiles of nickel particles with different diameter for a volume flow of $400\ \ cm^3 \cdot min^{-1}$. Here the larger particles follow the profile of the glass beads when the collector is included, whereas the smaller particles experience a shift to the left that results in a velocity profiles that is in between the glass beads with and without collector. When looking at the FWHM in Figure 4.2.7a no significant change in the broadness of the velocity distributions is noticed. When examining the velocity at the peak in Figure 4.2.7b, indeed a slight increase in velocity is observed. The particles might behave differently due to more turbulence induced flow patterns present in the large column. The smaller particles could experience a higher influence of these turbulent flow patterns, which would then result in the deviation noticed in Figure 4.2.6.

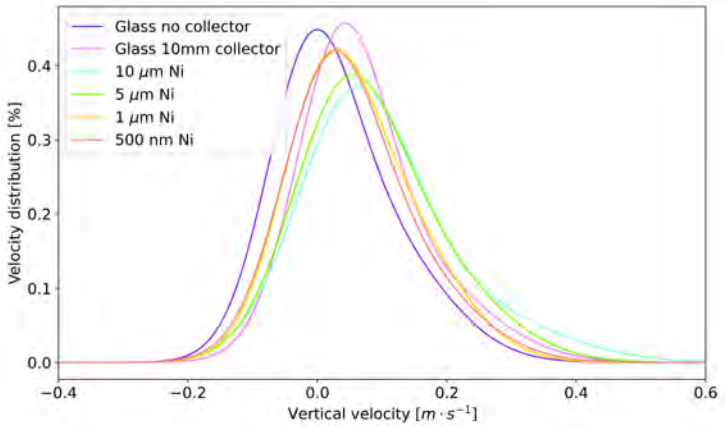

Figure 4.2.6: Velocity profiles in vertical direction in large column with inlet diameter of $1\ mm$ *for nickel particles with volume flow of* $400\ \ cm^3 \cdot min^{-1}$*, velocity profile of* $500\ nm$ *particles obtained at power of* $210\ mW$*.*

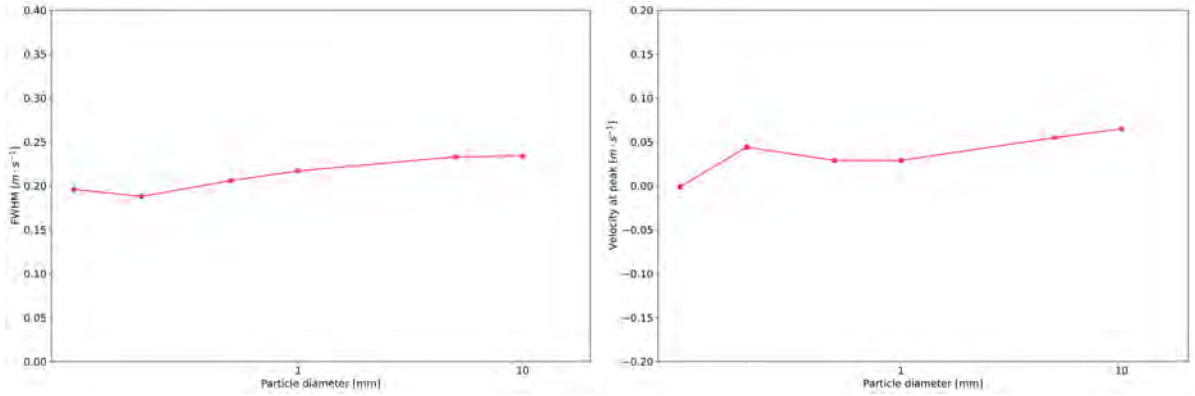

(a) *(b)*

Figure 4.2.7: FWHM (a) and velocity at maximum of velocity distribution (b) at a volume flow of $400\ \ cm^3 \cdot min^{-1}$*, and inlet diameter of* $1\ mm$ *corresponding to Figure 4.2.6.*

The velocity profiles for 350, 450, and $500\ \ cm^3 \cdot min^{-1}$ can be found in the Appendix in Figure A9a, A9b, and A9c respectively. Here it can be noticed that when increasing the volume flow, the smaller particles behave more similar to the larger particles compared to lower volume flows. When increasing the volume flow the flow regime transitions from a transitional regime to a heterogeneous regime. From Figure 4.1.3a it was evident that the bubble size distributions were much broader for 400, 450, and $500\ \ cm^3 \cdot min^{-1}$ than for $350\ \ cm^3 \cdot min^{-1}$. Additionally, from Figure 4.2.1d the velocity distribution experienced a shift when increasing the volume flow from 400 to $500\ \ cm^3 \cdot min^{-1}$. It could therefore be the case that when increasing the volume flow from 350 to $500\ \ cm^3 \cdot min^{-1}$ the transitional regime transforms to the heterogeneous regime. The transitional regime could occur at $350 - 400\ \ cm^3 \cdot min^{-1}$, and the heterogeneous regime at $450 - 500\ \ cm^3 \cdot min^{-1}$. In the heterogeneous regime bubble coalescence and breakup are balanced, which could results in less deviation inside the bubble column compared to the transitional regime. Therefore, the particle velocity distribution stabilizes, and the smaller particles behave similar to the larger particles.

4.2.3. Dimensionless Analysis

To understand why the particles behave similarly, the Stokes number was calculated based on a range of occurring bubble sizes with their velocity calculated by Equation 2.23. The results are depicted in Figure 4.2.8.

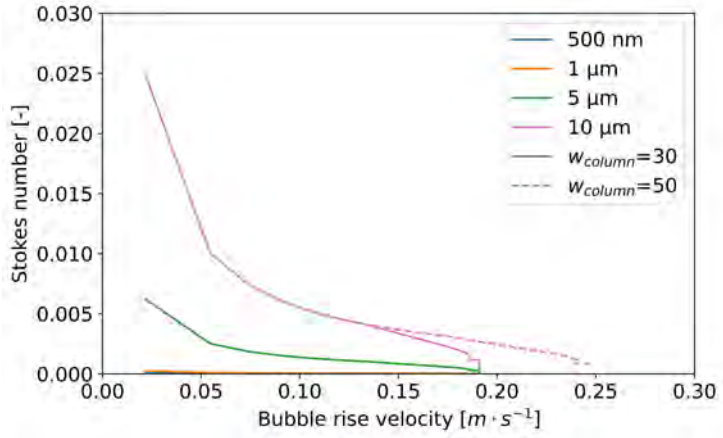

Figure 4.2.8: Stokes number for a range of bubble sizes with velocity described by Equation 2.23, jumps in Stokes number occur due to the change in $\frac{d_b}{D_T}$, which affects the SF in the determination of the bubble rise velocity. w_{column} is given in mm.

From Figure 4.2.8, it is seen that the Stokes' number is very low. This indicates that inertial forces have practically no effect on the motion of the particles, and the motion can thus regarded to be inertia-free. The trajectory of the particle is dominated by hydrodynamic interaction. As a result the trajectory of the particles coincide with the fluid streamlines [63]. This further confirms that the particle lift in the bubble column is independent of particle size and density in this range investigated.

4.3. Particle Recovery

This section discusses the results of experimentally investigated particle recovery under different conditions. First, particle recovery in the small column is discussed. Then particle recovery in the large column. Followed by the particle recovery over time and the influence of different collectors. Finally, sedimentation time is argued to have a possible effect on particle recovery.

4.3.1. Particle Recovery in Small Column

Since understanding the mechanism behind particle recovery is easier for low volume flows due to less complexity in comparison to higher volume flows, a volume flow of $100\ cm^3 \cdot s^{-1}$ was selected. Figure 4.3.1 depicts the particle recovery for a range of zinc-oxide and nickel particles at $100\ cm^3 \cdot s^{-1}$ for different inlet diameters. From this figure it is noticed that the inlet with a diameter of $1\ mm$ always outperforms the inlets with 1.5 and $2.5\ mm$. Furthermore, for an inlet of $1\ mm$ the particle recovery is similar for the size range of zinc-oxide particles. For the nickel particles, the particles with a diameter of $1\ \mu m$ have double the recovery than the other sized particles.

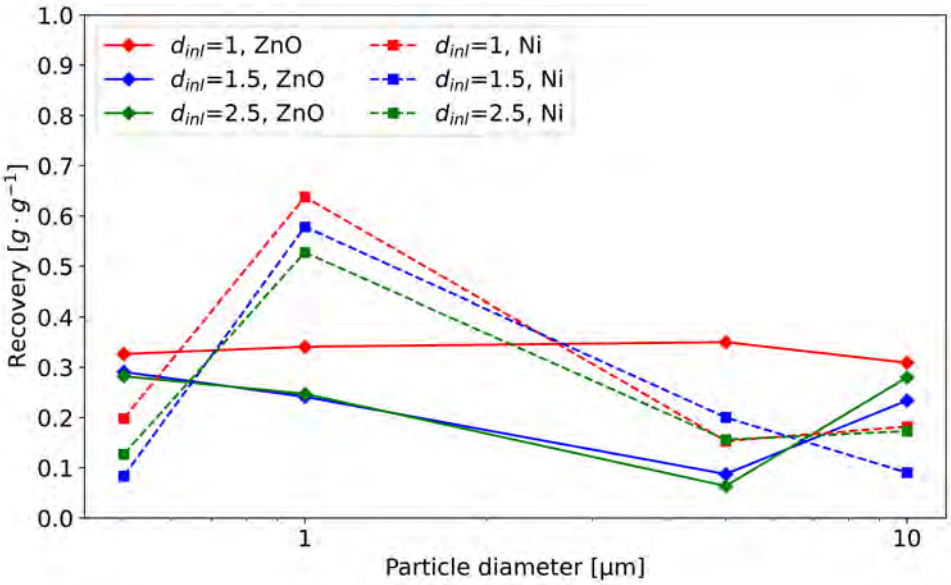

Figure 4.3.1: Particle recovery for a range of sizes of zinc-oxide and nickel particles at a volume flow of $100\ cm^3 \cdot min^{-1}$ *in the small column,* d_{inl} *is given in* mm.

A reason for the higher recovery for smaller inlet diameter might be due to the number of bubbles in the column. As was seen in Figure 4.1.2, the bubbles grow bigger for a bigger inlet. This would mean that there are more bubbles present when using a smaller inlet size. If there are more bubbles, there are more bubbles at which entrainment can occur, resulting in a higher particle recovery. Furthermore, it is observed that at an inlet diameter of $1\ mm$ there is only a slight deviation of particle recovery for differently sized particles. This is in line with earlier discussed evidence that particle lift is independent of particle size. Furthermore, at a volume flow of $100\ cm^3 \cdot s^{-1}$ it can be

noticed that generally zinc-oxide particles are easier to recover than nickel particles. This could be because the mass of the zinc-oxide particles is almost half the mass of the nickel particles, and therefore it might be easier to push the zinc-oxide particles through the opening of the collector.

When the particles have been pushed into the collector, the sedimentation time might have an effect on particle recovery. The sedimentation time can be calculated using Stokes' law, as in Equation 2.37. The results can be found in Table A1 in the Appendix. From this it is suggested that with decreasing particle size, the sedimentation time increases significantly. For zinc-oxide particles for an inlet of $1\ mm$ particle recovery of $5\ \mu m > 1\ \mu m > 500\ nm > 10\ \mu m$ particles, for an inlet of $1.5\ mm$ particle recovery of $500\ nm > 1\ \mu m > 10\ \mu m > 5\ \mu m$ particles, and for an inlet of $2.5\ mm$ particle recovery of $500\ nm > 10\ \mu m > 1\ \mu m > 5\ \mu m$ particles. Additionally, for nickel particles for an inlet of $1\ mm$ particle recovery of $1\ \mu m > 500\ nm > 10\ \mu m > 5\ \mu m$ particles, for an inlet of $1.5\ mm$ particle recovery of $1\ \mu m > 5\ \mu m > 10\ \mu m > 500\ nm$ particles, and for an inlet of $2.5\ mm$ particle recovery of $1\ \mu m > 10\ \mu m > 5\ \mu m > 500\ nm$ particles. This does not suggest a clear relationship between sedimentation time and particle recovery if the volume flow is $100\ \ cm^3 \cdot min^{-1}$.

Results obtained by Dr. Ir. Ruben Dewes showed that particle recovery for nickel particles increased with increasing volume flow. Next to a higher volume fraction of air being present at higher volume flows, this might be due to the change from a homogeneous regime to a heterogeneous regime. In the heterogeneous regime, turbulence in the column is increased. Higher turbulence might results in trapping the particles more effectively in the wake of the bubbles. Additionally, when increasing the volume flow, $10\ \mu m$ and $5\ \mu m$ nickel particles obtain a higher recovery than $1\ \mu m$ and $500\ nm$ nickel particles. For larger particles, the sedimentation time decreases. This suggests that when increasing the volume flow the sedimentation velocity becomes more important than at lower volume flows. This could be because at higher volume flows, a higher volume fraction of air is present in the column, which could increase the probability of flushing particles out of the collector whilst they sediment. During flushing the particles are flushed from the collector back inside the column, instead of being recovered inside the collector. Since the sedimentation time is much larger for smaller particles, this leads to more time for possible flushing, hence decreasing the particle recovery for smaller particles.

To investigate the effect of the column diameter on the particle recovery, the recovery under different flowrates was investigated in the large column. The results will be examined in the next section.

4.3.2. Particle Recovery Difference in Large Column

It was investigated whether the same results could be obtained for the large column as in the small column. The results are depicted in Figure 4.3.2. The results obtained by Dr. Ir. Ruben showed a recovery of $> 50\%$ at a volume flow of $350\ cm^3 \cdot s^{-1}$ in the small column. For the large column, except for the $1\ \mu m$ particles, the recovery is $< 30\%$. When increasing the volume flow, a slight increase in particle recovery for $10\ \mu m$ particles is observed. However, for $1\ \mu m$ particles, a slight decrease in particle recovery

is noticed. For $500\ nm$ particles, an increase in particle recovery for $400\ cm^3 \cdot s^{-1}$, but a decrease in particle recovery when increasing the volume flow further can be discerned. For $5\ \mu m$ particles, an increase in particle recovery when increasing the volume flow to $400\ cm^3 \cdot s^{-1}$, a decrease for $450\ cm^3 \cdot s^{-1}$, and an increase again for $500\ cm^3 \cdot s^{-1}$ is distinguished.

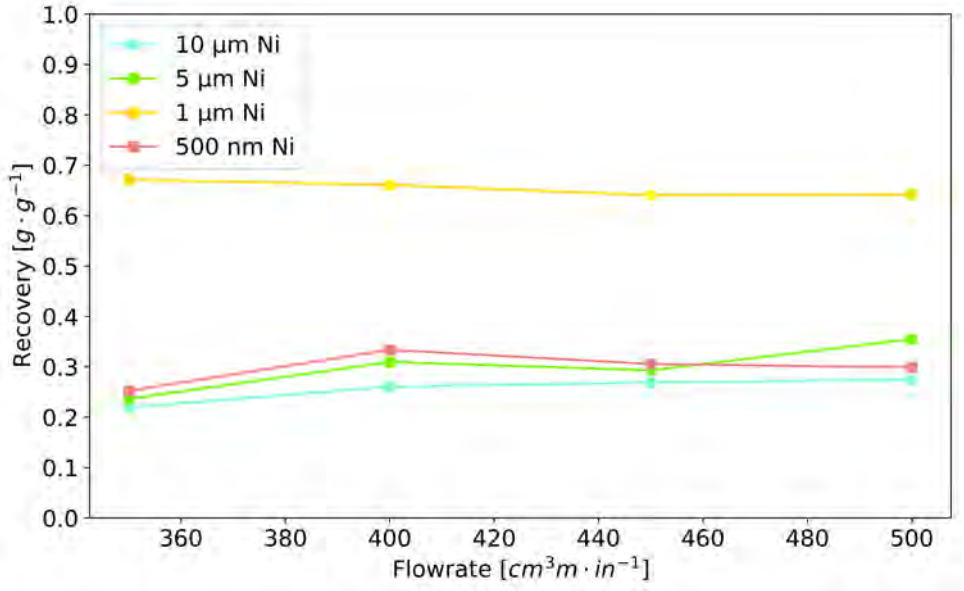

Figure 4.3.2: Particle recovery for a range of sizes of nickel particles at different volume flows in the large column.

From Figure 4.1.4 it has been argued that bubble size increased at $400\ cm^3 \cdot s^{-1}$ compared to 350, 450, and $500\ cm^3 \cdot s^{-1}$. This could explain why particle recovery is generally higher for $400\ cm^3 \cdot s^{-1}$ than for $350\ cm^3 \cdot s^{-1}$. Additionally, for higher volume flows it was noticed that the particles behave more similar to the glass beads including the collector on top. This could indicate that for higher volume flows the particles follow the fluid streamlines better, which in turn could be the reason for a higher particle recovery.

Interestingly, Figure 4.3.2 suggests that particle recovery in the large column is higher for smaller particles than for larger particles, whereas in the small column particle recovery is higher for larger particles than for smaller particles. In the small column, the gas volume fraction is much larger at the investigated volume flows than in the large column. This could result in a higher probability of flushing particles out in the small column than in the large column, suggesting that sedimentation time is of less importance in the large column than in the small column at these volume flows.

It is known that flotation performs best for small bubbles and big particles, however this thesis aims to analyze whether entrainment can be used for effective particle removal. Therefore, to analyze whether the assumption that all particles recovered are due to entrainment, the collision efficiency can be calculated. However, models to calculate the collision efficiency are valid for a maximum Reynolds number of 500. In the bubble column, the Reynolds numbers encountered exceed this value significantly, therefore, no model exists which would accurately determine the collision efficiency.

Hence, it is assumed that the collision efficiency is negligible at high Reynolds numbers, and is therefore exceedingly low. Since the flotation probability is also dependent on the attachment, and detachment probability, the flotation probability can be assumed to be even lower than the collision efficiency. Therefore it is assumed that the particles recovered are purely due to entrainment, and not flotation.

4.3.3. Particle Recovery over Time

In the previous results, the particle recovery was measured after one hour of operation time. Since Equation 3.14 suggest that after a certain time a plateau is reached, it was investigated whether there is a correlation between particle recovery and time. Figure 4.3.3 depicts the particle recovery over time for $10\ \mu m$ zinc-oxide and nickel particles for different volume flows, and different collector opening diameters. The corresponding values for k, R_{max}, and R^2 for the fits can be found in the Appendix. From this Figure it is noticed that the particle recovery for nickel appears to occur quicker than for zinc-oxide. After two hours, for zinc-oxide particles the least amount of particles are recovered for a volume flow of $300\ cm^3 \cdot s^{-1}$ with an collector opening diameter of $10\ mm$. The second-least amount of particles are recovered at a volume flow of $100\ cm^3 \cdot s^{-1}$ and a collector opening diameter of $7.5\ mm$. Lastly, almost equal amount of particles are recovered for a volume flow of $300\ cm^3 \cdot s^{-1}$ with either an inlet diameter of $2.5\ mm$ in combination with a collector opening diameter of $10\ mm$, or an inlet diameter of $1\ mm$ with a collector opening diameter of $7.5\ mm$. For nickel particles, the least amount of particles are recovered for a volume flow of $100\ cm^3 \cdot s^{-1}$ with a collector opening diameter of $7.5\ mm$. Then similar amounts of particles are recovered at a higher volume flow of $350\ cm^3 \cdot s^{-1}$ with the different inlet sizes and a collector opening diameter of $10\ mm$. Lastly, the most amount of particles are recovered at a volume flow of $350\ cm^3 \cdot s^{-1}$, an inlet size of $1\ mm$, and a collector opening diameter of $7.5\ mm$.

The results suggest that more particles were recovered using the collector with a smaller opening diameter at higher volume flows. This could be due to flushing out of the particles. When the opening diameter is larger, the probability of the particles being flushed back into the column increases, since a larger area is available for the particles to travel back into the column. This could indicate that using a smaller opening diameter than bubble size could help prevent flushing out of the particles, resulting in a higher particle recovery.

For the large column, particle recovery over time was determined for the different particle sizes. The results can be found in Figure 4.3.4, and the k, R_{max}, and R^2 values in the Appendix. From Figure 4.3.4 it is observed that particle recovery occurs quicker for larger particles than for smaller particles. After two hours, the particle recovery of $500\ nm$ particles still increases significantly compared to the particles recovered after one hour. For $1\ \mu m$ particles, it can be noticed that the particles recovered after two hours start to be constant compared to the particles recovered after one hour. Whereas for both $10\ \mu m$ particles and $5\ \mu m$ particles, the particles recovered after one hour is not increased significantly compared to the particles recovered after 30 minutes.

From particle recovery in the small column and the large column it is evident that

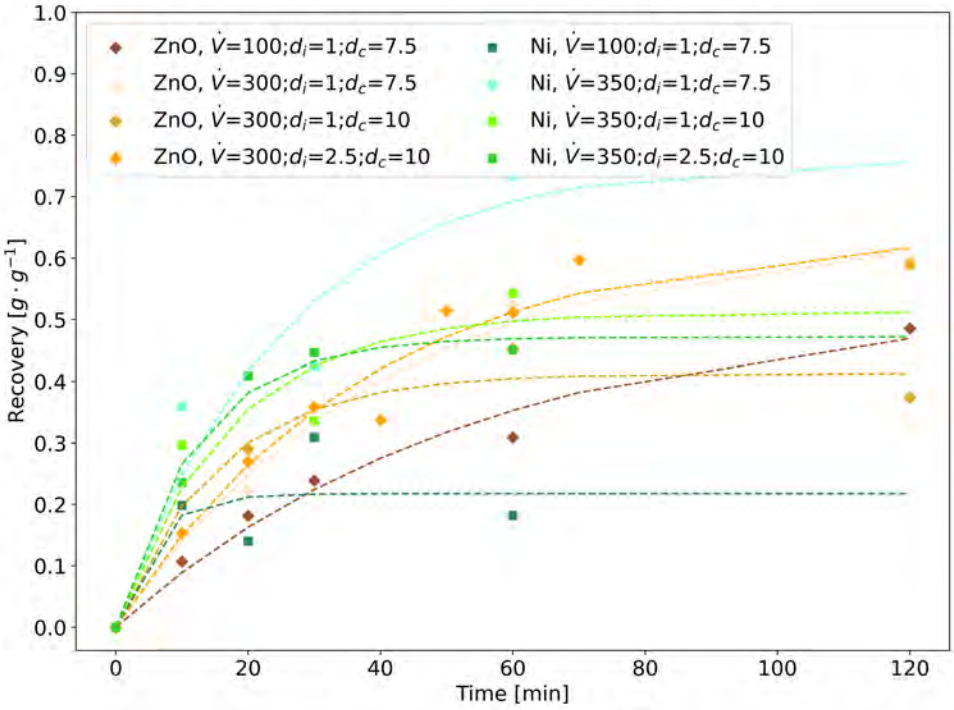

Figure 4.3.3: Particle recovery over time for $10\ \mu m$ *zinc-oxide and nickel particles, fitted with Equation 3.14, for different inlets, volume flows, and collector opening diameters,* $\dot{V}$ *is given in* $cm^3 \cdot min^{-1}$*,* d_i *in* mm*, and* d_c *in* mm*.*

nickel particles are recovered faster than zinc-oxide particles, and larger particles are recovered faster than smaller particles. This might be due to the difference in sedimentation time of the particles. As can be seen from Table A1 in the Appendix, the sedimentation time for zinc-oxide particles is larger due to their density being smaller than for nickel particles. Furthermore, the smaller particles need longer time to sediment than larger particles. Together with the particle recovery of small particles in Figure 4.3.4 being larger than that for bigger particles, this might suggest that smaller particles are easier to recover through entrainment if the time of recovery is increased. This is in line by results obtained by Wang et al. (2015) in Figure 2.2.2, where particle recovery by entrainment increased significantly when decreasing the particle size.

What could be a possible disadvantage of the recovery of small particles, is flushing the particles out of the collector whilst they sediment. Because the sedimentation time is much larger for smaller particles, this leads to more time for possible flushing. This might lead that the time it will take to recover all particles from the column takes simply too long. However, in the scope of the MSR, it is not needed to recover all particles, since the continuous flow of the molten salt would lead to particle agglomeration, until eventually the particles reach an optimal size for particle entrainment.

The R^2 values of fitting Equation 3.14 through the experimentally obtained results are generally higher than 0.9. This suggests that Equation 3.14 describes the time-dependent behavior of particle recovery sufficiently accurate. The R_{max} values suggest that particle recovery for $1\ \mu m$ and $500\ nm$ nickel particles in the large column with a collector with opening diameter of $10\ mm$ reaches up to 90%. This would indicate that

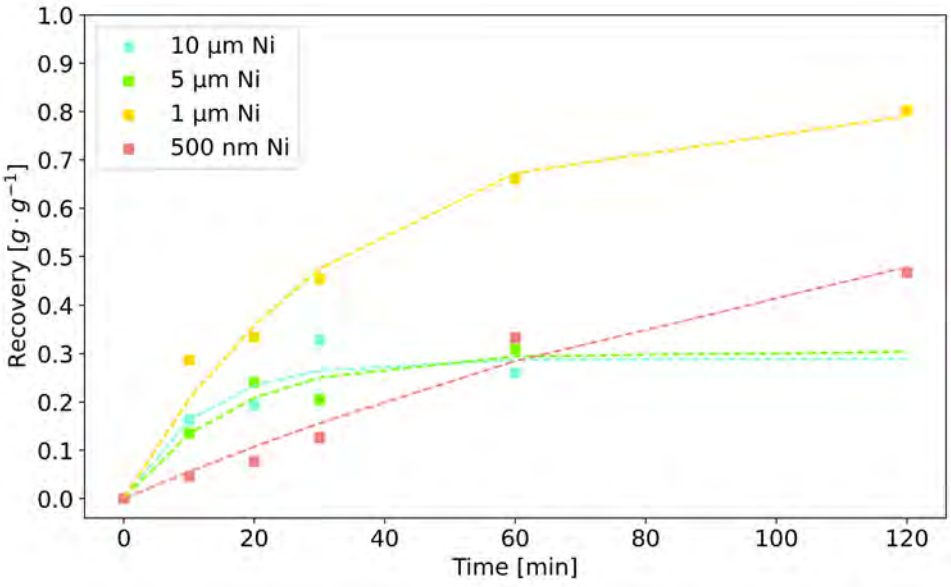

Figure 4.3.4: Particle recovery over time for differently sized nickel particles, fitted with Equation 3.14 at volume flow $400\ \ cm^3 \cdot min^{-1}$.

particle recovery through entrainment can be very effectively in the MSR. However, this should be experimentally determined if this maximum is indeed reached after a longer operation time, or if the maximum value for recovery will be lower. For the small column the dependency of operation time and particle size was only determined for $10\ \mu m$ nickel particles. However, it would be interesting to investigate whether particle removal for smaller particles increases as well for longer flow-time in the small column. Since particle removal in the small column was generally higher than in the large column, the recovery of small particles in the small column could reach even higher than 90%, which would be a very promising result.

From the values for k no direct relationship was detected between particle size and volume flow. To understand what could affect the recovery constant, more research is needed.

Some further comments need to be noted. As can be seen in Figure A1 in the Appendix, the particle recovery of $500\ nm$ of nickel particles is difficult to accurately measure. This is due to the particles sticking to the collector, leading to an underestimation of the number of particles recovered. This would suggest that the recovery of $500\ nm$ nickel particles is actually much higher than that is indicated in the results. Furthermore, for higher volume flows of zinc-oxide particles, many particles were ejected out of the column, as can be seen in Figure A2 in the Appendix. This also leads to an underestimation of recovered particles for zinc-oxide.

Some error might occur in the measurement of particles recovered. In the column, the water level was tried to be the same between experiments, however, it is reasonable that some deviations might have occurred between experiments. A difference in water level would result in a difference in sedimentation time, which in turn could result in deviations in the number of particles recovered. Additionally, the scale used might include some error. For the scope of this thesis this error has been assumed to be neg-

ligible, but deviations in measurement could have an effect on the predicted amount of particles recovered. Furthermore, deviations in rinsing the collector might occur in differences in how many particles were rinsed out of the collector, and therefore measured. Because of the color of the collector, it was for some particles more difficult to decipher whether all particles had been rinsed out of the collector. To investigate the effect of the possible errors in particle measurements, the experiments should be repeated, to see whether the same results would be obtained with repetition of the experiments done.

4.4. CFD Study of the Vertical Velocity in a Bubble Column

The results obtained so far have been experimentally determined by using water and air as a replacement model for molten salt and helium. To be able to investigate the effect of switching from water and air to molten salt and helium, a CFD model might prove useful. When building a set-up with molten salt and helium, it is much more difficult to obtain optical data inside the column, since the use of molten salt requires the usage of metal alloys as column material. Therefore, to investigate particle and bubble behavior in the column, it is useful to obtain a model that accurately describes the real world problems. To this end, a basic model was developed in Ansys Fluent, from which the results will be discussed in the next sections.

4.4.1. Velocity Profiles of a Single Bubble in the Small Column

In this section, the velocity of the liquid induced by a single bubble in the small column is examined. First, the effect of bubble size is highlighted, then the effect of the collector is discussed.

4.4.1.1. Bubble Size Dependent Velocity without Collector

The velocity of the fluid that is induced by a single bubble of different size was investigated in the small column, and the results are depicted in Figure 4.4.1. In this Figure, it can be noticed that the velocity increases with increasing bubble size. Furthermore, the velocity is highest in the middle of the column, and lowest at the wall. Which is as expected, since the rise of the bubble is driven by natural convection. Deng, Mehta, and Warren (1996) also reported that the liquid velocity obtains positive values in the central part of the flotation column, and negative near the wall area [99]. Additionally, Kováts, Thévenin, and Zähringer (2020) stated that rising bubbles generate an ascending flow in the center of the column, which reaches and evolves a thin, descending back-flow near the wall, which is independent of position [56]. The differences in velocity profiles in Figure 4.4.1 could be allocated to differences in location with respect to the bubble. Some similarities in the velocity profiles can be noticed. In Figure 4.4.1a a similar profile for $y = 150\ mm,\ t = 1.1\ s$ and $y = 200\ mm,\ t = 1.5\ s$ is observed, which could indicate that indeed the velocity induced by the bubble is not dependent on the location in the column, but rather on the location with respect to the bubble.

In Figure 4.4.1b it is observed that the velocity is not symmetrical in the horizontal axis in all profiles. This could be due to asymmetry in the bubble shape, causing deformations in the bubble and thus an asymmetrical bubble rise velocity. This could indicate that deformations in bubble shape and thus in velocity profiles are caused by differences in bubble size. For a bubble size with equivalent diameter $5\ mm$, it is detected that the bubbles do not experience deviations, see Figure B1a in the Appendix. For bubble sizes with equivalent diameter 7.5 and $10\ mm$ deformations in the bubble shape are noticed. Whereas for bubbles with equivalent diameter 12.5 (Figure B1b in the Appendix) and $15\ mm$ again no deformations are observed. Islam et al. (2013) reported that as bubbles rise upward a liquid jet forms at the bottom of the bubble. The

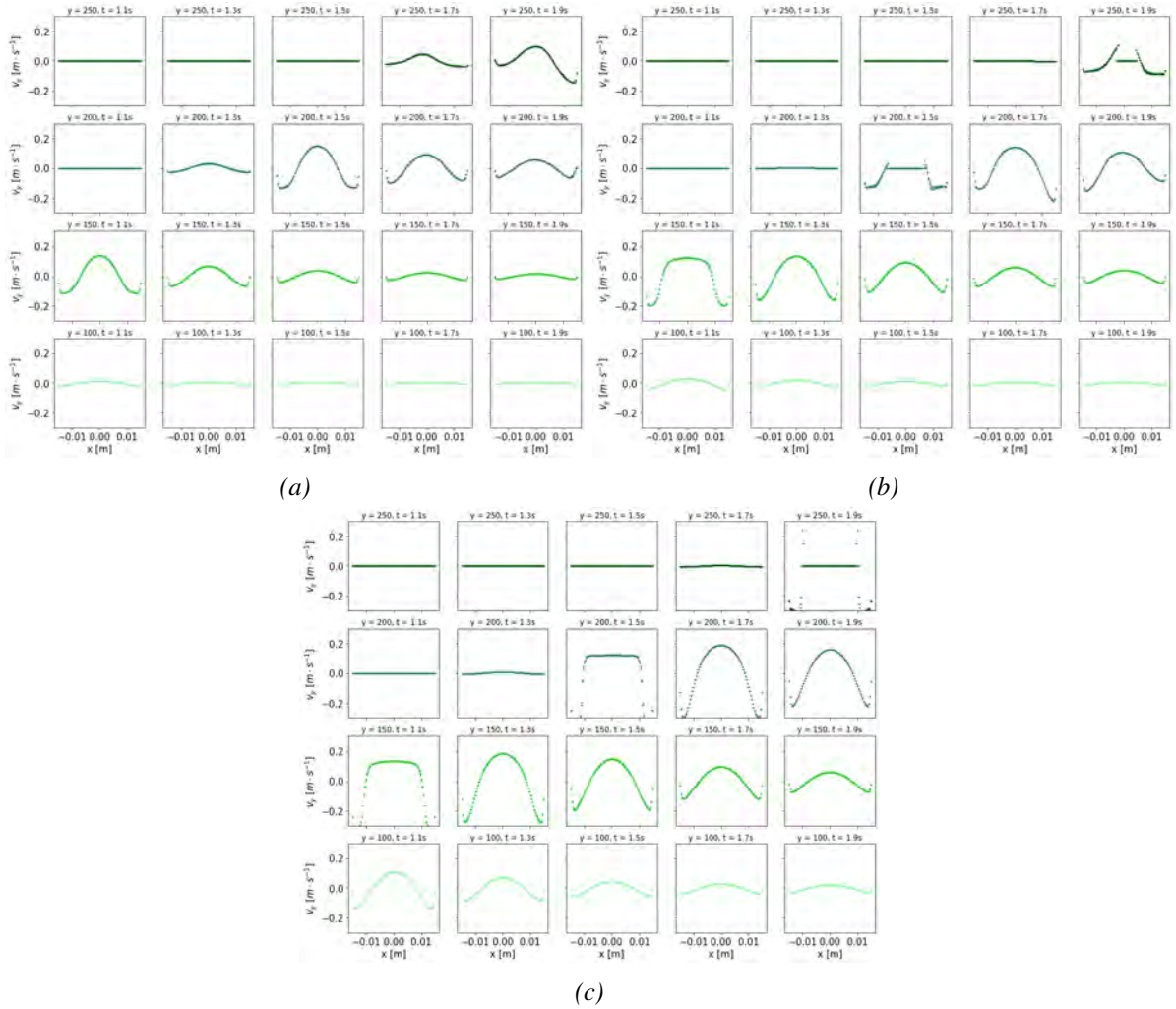

Figure 4.4.1: Velocity profiles of water in the small column with no collector with bubble equivalent diameter 7.5 *(a),* 10 *(b), and* 15 mm *(c), the unit of the position is given in* mm*, of time in* s *which indicates the flow-time of the simulation. Positions with zero velocity can indicate the position of the bubble.*

jet pushes the lower surface of the bubble towards the top surface, creating a pressure gradient at the lower surface greater than at the top surface of the bubble. The pressure differences create a vortex that includes rotation, which causes the bubble to deform. Generally, larger bubbles deform more than smaller bubbles, and the wall can affect the vortex by creating secondary vortices [54]. It is possible that for bubbles smaller than $5\ mm$ the vortex does not experience deformations due to the wall, whereas for bubbles between 7.5 and $10\ mm$, deformation are induced due to the wall. Then, for bubbles bigger than $12.5\ mm$, the wall stabilizes the bubble trajectory, so that no deformations can be noticed.

4.4.1.2. Velocity of Liquid Dependency on Collector

To investigate whether adding the collector in the geometry would have an effect on the bubble rise velocity, two different collectors were simulated. The results are de-

picted in Figure 4.4.2. It can be seen that adding the collector results in a more chaotic velocity profile. However, the general profile is still similar, indicating that indeed the collector does not have a significant effect on the velocity profiles in the column. Furthermore, the velocity profile is more chaotic for the collector with opening diameter of $7.5\ mm$ compared to the collector with opening diameter of $10\ mm$. At $y = 196\ mm,\ t = 1.8\ s$ in Figure 4.4.2b the liquid experiences a negative velocity near the edges of the collector opening. This can also be explained by shear stress at the wall. Additionally, at the opening of the collector, it is more difficult for the bubble to get pushed through the opening, resulting in the hold up of the bubble at the opening. This is especially visible for the collector with opening diameter $7.5\ mm$, where the bubble is not able to travel through the collector in the depicted flow-time.

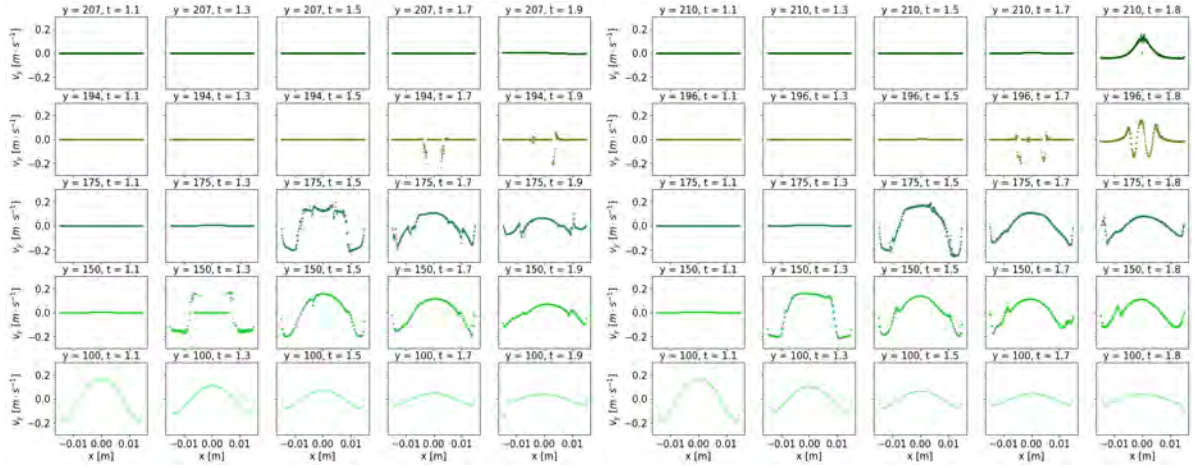

(a) *(b)*

Figure 4.4.2: Velocity profiles of water in the small column with collectors $d_{opening} = 7.5\ mm,\ \theta = 60°$ (a), and $d_{opening} = 10\ mm,\ \theta = 64.7°$ (b) with bubble equivalent diameter $10\ mm$, the unit of the position is given in mm, of time in s which indicates the flow-time of the simulation. Positions with zero velocity can indicate the position of the bubble.

4.4.2. Velocity Profiles of a Single Bubble in the Large Column

In this section the velocity induced by a bubble in the large column is discussed. First, the effect of the different collectors is considered, then the effect of a second row of bubbles, and lastly the conical shape of the column.

4.4.2.1. Velocity of Liquid Dependency on Collector

The bubble rise velocity of the bubbles in the large column is higher than that of the bubbles in the small column. This is in line with experimentally determined bubble rise velocities. This is due to the bubble not experiencing the effect of the wall as much as for the small column, resulting in a higher bubble rise velocity.

To investigate the effect of the collector in the large column, the two different collectors are compared. The results are depicted in Figure 4.4.3. Again, minimal difference between the two different collectors is noticed. The velocity is again highest in the

middle and lowest at the wall. It should be noted that the deformations in velocity profiles are less than in the small column with equal bubble equivalent diameter. Because the diameter of the column is wider, the bubbles experience less influence of the wall, which could result in no formation of secondary vortices, therefore stabilizing the bubble shape. Furthermore, the collector with an opening diameter of $7.5\ mm$ prevents the bubble to get pushed through the column, resulting in a hold up of the air bubble at the opening, whereas for the opening diameter of $10\ mm$ the bubble does get pushed through. To investigate whether multiple bubbles could prevent the gas hold-up at the opening of the collector, a simulation has been done that examines the velocity profiles induced by multiple bubbles. The results will be the subject of the next section.

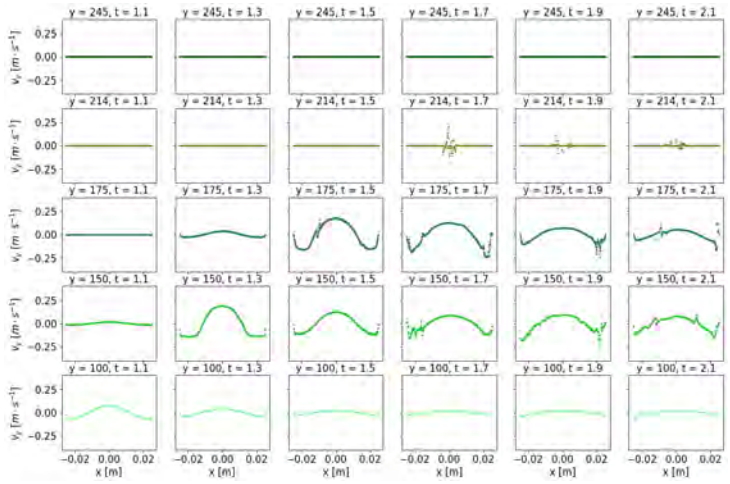

(a)

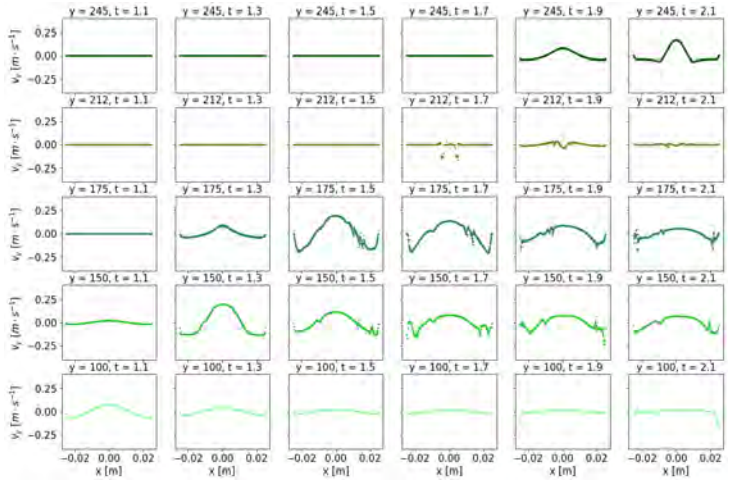

(b)

Figure 4.4.3: Velocity profiles of water in the large column with collectors $d_{opening} = 7.5\ mm$, $\theta = 60°$ (a), and $d_{opening} = 10\ mm$, $\theta = 61.9°$ (b) with bubble equivalent diameter $10\ mm$, the unit of the position is given in mm, of time in s which indicates the flow-time of the simulation. Positions with zero velocity can indicate the position of the bubble.

4.4.2.2. Velocity of Multiple Bubbles and Effect of Column Shape

Figure 4.4.4 visualizes the effect of multiple bubbles in the column, and the effect of the cone-like shape of the column with respect to the rectangular shape previously simulated. In Figure 4.4.4a a horizontally symmetrical velocity profile is observed. From this it becomes evident that when increasing the bubble equivalent diameter from $10\ mm$ to $15\ mm$, still no deformations of the bubble shape occur. Therefore, it can be concluded that no secondary vortices are formed due to less influence of the wall of the column. However, when simulating a second bubble, as can be seen in Figure 4.4.4b the velocity profile is no longer symmetrical at each position in time. This could indicate that the wake of the preceding bubble influences the vortex behind the second bubble, creating instabilities, which results in deformations in the bubble shape. Additionally, at the opening of the collector it can be noticed that the first bubble does not get pushed through, whereas adding a second bubble allows the first bubble to be partly pushed through.

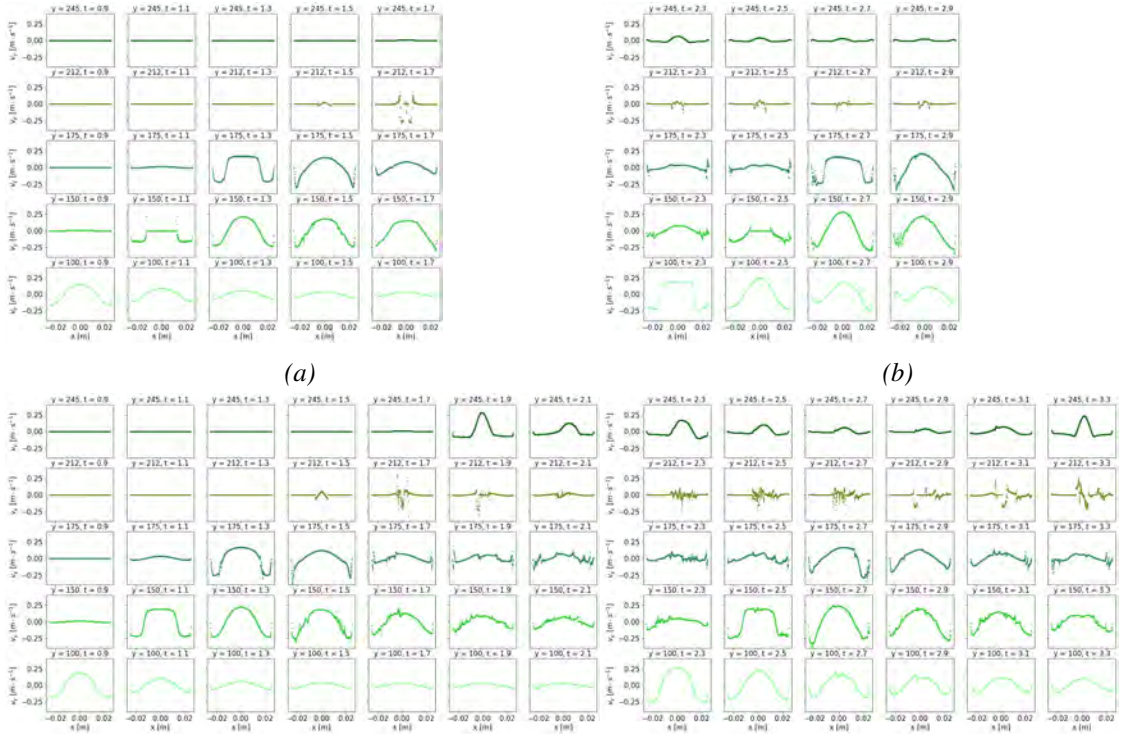

Figure 4.4.4: Velocity profiles of water in the large column with a collector with opening diameter of $10\ mm$ *and angle* $61.9°$ *for a bubble with equivalent diameter of* $15\ mm$ *(a), where the conical shape is included (c), and for a second round of bubbles excluding (b), and including the conical shape (d), the unit of the position is given in* mm*, of time in* s *which indicates the flow-time of the simulation. Positions with zero velocity can indicate the position of the bubble.*

From Figure 4.4.4b it can be noticed that the bubble rise velocity is higher for the second bubble than for the first bubble. This can be explained by the second bubble being affected by the wake of the first bubble, experiencing an acceleration in its bubble rise velocity.

When simulating the conical shape of the column, it becomes evident that the shape of the bottom part of the column does not significantly affect the velocity of the liquid in the top part column. From Figure 4.4.4c indeed a symmetrical velocity profile can be observed. It becomes also evident that the bubble does get pushed through the opening of the collector if more flow-time has passed. Additionally, the velocity profiles in Figure 4.4.4d are no longer symmetrical, showing evidence of the wake of the first bubble affecting the rise of the second bubble.

Since the shape of the column does not significantly affect the velocity profiles in the column, this suggests that modeling a rectangular column instead of a conical column is indeed a correct assumption. The shape of a rectangular column is less complex than a conical column. Therefore, this could help with decreasing the complexity of the simulation, and thus decreasing the simulation time.

Simulations have been carried out to investigate the effect of multiple small bubbles on the velocity inside the column. The results can be found in the Appendix. From this it was found that above and behind the bubble the velocity was highest, whereas a negative velocity occurred at the wall and in between the bubbles. The bubbles eventually tended to coalescence, forming again a single velocity profile as displayed by a single bubble. Additionally, when adding a second round of bubbles, the bubbles experienced a higher bubble rise velocity, and earlier coalescence. The results can be found in the Appendix.

4.4.3. From Water and Air to Molten Salt and Helium

Figure 4.4.5 visualizes the effect of changing a water and air system to a molten salt and helium system. When changing the water and air system to a molten salt and helium system, it is noticeable that the bubble rise velocity increases. Besides the increased bubble rise velocity, there is little difference between the velocity profiles. This could be due to an increased buoyancy force on the bubble. The buoyancy is dependent on the density difference between the liquid, and the gas. The density of water is $997\ kg \cdot m^{-3}$, the density of the molten salt is $1847.6\ kg \cdot m^{-3}$, the density of helium is $0.166\ kg \cdot m^{-3}$, and the density for air is $1.21\ kg \cdot m^{-3}$. The density of the gas is negligible, since $\rho_G \ll \rho_L$. Since the density of the molten salt is much higher than that of the water, a bubble in molten salt experiences a higher buoyancy force compared to water. Additionally, gravitational forces are expected to be negligible, due to the low density of the gas. Additionally, in this bubble regime, surface tension was shown to be negligible, therefore the bubble rise velocity is only dependent on buoyancy. The differences in the velocity profiles could be due to differences in deformations of the bubble, causing different fluid patterns inside the liquid.

4.4.4. Convergence Issues in Ansys Fluent

As can be seen in the results above, not all simulations reached equal flow time. This was due to divergence in the solution of the simulation. Multiple strategies, like decreasing the step size, increasing the mesh size, or using a different model, have been employed to try and reach a stable simulation, however none resulted in a converging

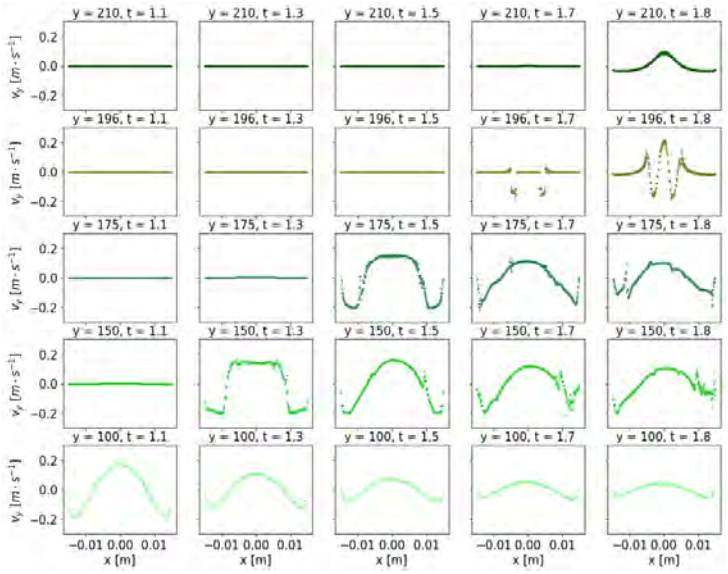

Figure 4.4.5: Velocity of molten salt induced by a helium bubble with bubble equivalent diamter of $10\ mm$ *in the small column with the collector with opening diameter* $10\ mm$ *and angle* $64.7°$

solution. Crha et al. (2021) looked at the comparison of Ansys Fluent and COMSOL for the CFD simulation of a single bubble, and found that Ansys did not result in a convergent solution. Since they used the VOF model, and recommended that different methods might result in a converging simulation [100], the Eulerian model was used, since it could increase the accuracy of the simulation [84]. However, a stable solution was not reached in each simulated situation, which could suggest that using Ansys Fluent to model the rising of a bubble in a liquid, might not be the most suitable software to choose. Therefore, it might be useful to investigate whether different programs, like COMSOL or OpenFOAM, might provide a more accurate and stable solution.

4.5. CFD Study of Particle Lift in a Bubble Column

This section discusses the effect of different conditions on the effectiveness on particle lift, and subsequently particle recovery. First the particle lift of different particles is discussed, then the particle lift in the small column and the large column is examined. The effect of multiple bubbles is visualized, and the effect of changing the water and air system to a molten salt and helium system.

4.5.1. Particle Lift in Small Column Without collector

Figure 4.5.1 visualizes particle lift in the small column for different particles and particle sizes with a bubble with equivalent bubble diameter of $10\ mm$. In this Figure, minimal differences are indeed distinguished in particle lift for different particles, and particle sizes. Besides, the noticed differences can also be allocated to numerical deviations, instead of differences in particle lift. Therefore, it is assumed that each particle is equally well lifted to the top, which was also confirmed experimentally. In addition, it is observed that the particles directly behind the bubble experience a spiraling motion, whereas the particles at the wall experience a downward motion. The spiraling motion is dependent on the bubble size. For bubbles with bubble equivalent diameter of 5, 7.5, 10, 12.5, and $15\ mm$, the spiraling motion could only be distinguished for bubbles with bubble equivalent diameter of 7.5 and $10\ mm$. For a bubble equivalent diameter of $5\ mm$, the motion of the particles was upwards behind the bubble, and downwards near the wall. The same pattern was observed for bubbles with bubble sizes 12.5 and $15\ mm$. This could indicate, that particle lift is dependent on bubble size, and that too small or too large bubbles could have a negative impact on particle recovery.

When the bubble pushes through the area where the particles are located, no direct attachment of particles to the top of the bubble surface is observed. The flotation rate increases with decreasing bubble size [63], showing that indeed in this set-up particle lift occurs due to entrainment. The two relevant entrainment mechanisms are the transportation of particles in the bubble lamella, and particles trapped in the wake of the bubble [65]. In Figure 4.5.1 the particles that are located at the bubble surface could show evidence of particles being transported in the thin hydrodynamic layer of water that surrounds the bubble. More importantly, the particles that experience a spiraling motion show evidence that particles are affected by the wake of the bubble, which implies the potential for particle recovery in this set-up through entrainment.

4.5.2. Particle Lift in Small Column with Collector

Figure 4.5.2 visualizes the effect of particle lift of $10\ \mu m$ nickel particles in the small column with the addition of a collector with different opening diameters and angles. Figure 4.4.2a visualizes particle lift with the collector with a smaller opening, and Figure 4.4.2b shows particle lift in a column with the collector with the bigger opening. There is initially no big difference between the two collectors. With both collectors the particles experience a spiraling motion behind the bubble, and a downward motion

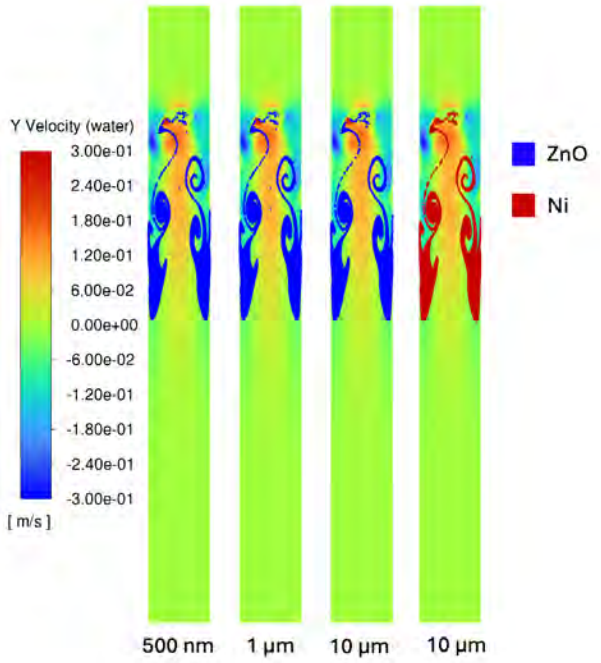

Figure 4.5.1: Particle lift of different sized zinc-oxide and nickel particles in the small column, with a bubble with bubble equivalent diameter of 10 mm after a flow-time of $1.9\ s$.

near the wall. However, at top of the column, just underneath the opening of the collector, particles experience a significantly higher upward movement when the opening of the collector is smaller. Additionally, when increasing the opening of the collector, the particles experience a higher downward movement in the middle of the column. This might suggest that particle recovery increases when reducing the opening of the collector, which aligns with experimental results.

To test whether particle lift with the collector was indeed not dependent on the type of particle, a simulation has been carried out where nickel was replaced by molybdenum. The results are depicted in Figure B10 in the Appendix. From this it is seen that indeed the type of particle does not result in a profound difference in particle lift. Furthermore, this would indicate that nickel can be used as a replacement for molybdenum. So that if adequate recovery of nickel particles occurs, adequate recovery for molybdenum particles is assumed to occur as well.

4.5.3. Particle Lift in Large Column with Collector

In Figure 4.5.3 the particle lift of $10\ \mu m$ nickel particles in the large column with a bubble equivalent diameter of 10 mm with the addition of different sized collectors is visualized. Figure 4.4.3a depicts the collector with a smaller diameter opening, and Figure 4.4.3b with a larger opening diameter. As in the small column, the size of the collector does not have a profound effect on the particle lift in the column. However, it is noticed that for the smaller collector after a flow-time of $2.1\ s$, the particles experience a higher downward velocity at the wall than for the larger collector. This can be attributed to the fact that for the smaller collector the bubble gets stuck at the

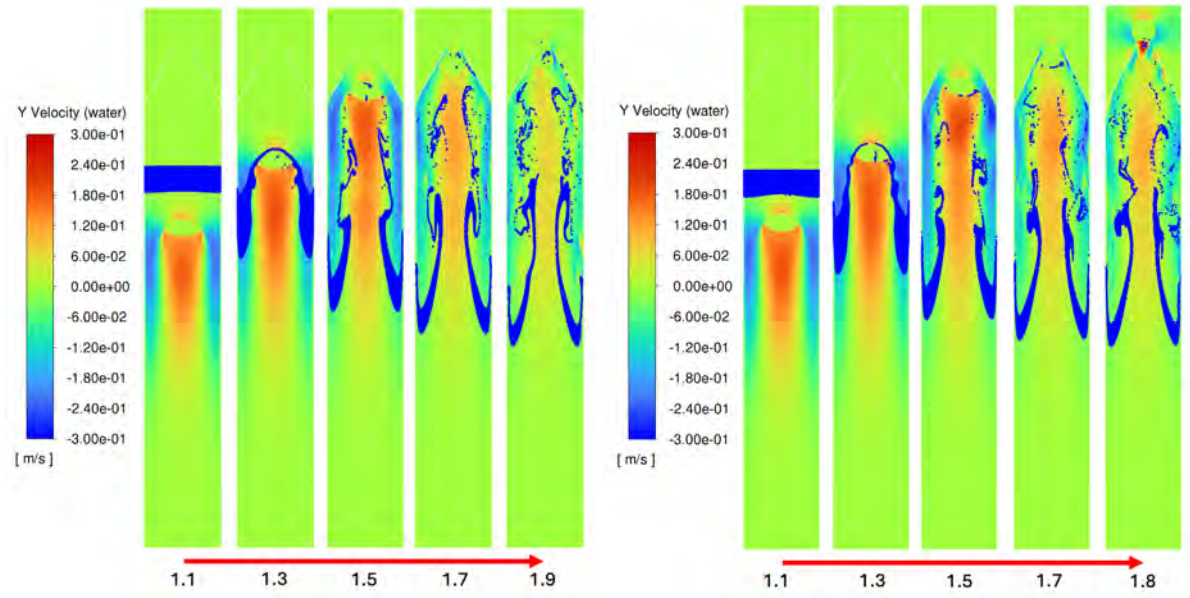

(a) *(b)*

Figure 4.5.2: Particle lift of $10\ \mu m$ *nickel particles in the small column with collectors* $d_{collector} = 7.5\ mm$, $\theta = 60°$ *(a), and* $d_{collector} = 10\ mm$, $\theta = 64.7°$ *(b), with a bubble with bubble equivalent diameter of* $10\ mm$*, the timeline is given in* s *of flow-time.*

opening of the collector, resulting in a higher negative velocity of the liquid, which results in particles moving to the bottom of the column. This could indicate that either the opening diameter should be increased, or that one should aim to generate smaller bubbles in the column to increase particle recovery. Additionally, the spiraling motion of the particles is less in the large column compared to the small column. As the vortex behind the bubble is less influenced by the wall, this could result in the lack of secondary vortices behind the bubble in the large column. This is confirmed by the absence of a spiraling motion experienced by the particles. The lack of secondary vortices might negatively affect the trapping of particles in the wake of the bubble, potentially explaining the decrease in particle recovery observed in the large column.

Up until now, the simulations discussed concerned simulations of a single bubble. A second bubble might have an influence on particle recovery, by increasing the turbulence in the column. Therefore, to investigate whether multiple bubbles could increase particle lift in the column, simulations have been carried out with multiple bubbles, which will be reviewed in the next section.

4.5.4. Particle Lift in Large Column for Multiple Bubbles

Figure 4.5.4 shows the effect of multiple small bubbles in the large column. Here, the middle bubble is pushed downward by the other two bubbles. This could be because the bubble experiences a negative velocity due to the water flowing downward at the sides of the bubble. The bubble then moves into the wake of one of the bubbles, catches up, and coalescence of the two bubbles occurs. Because of this, secondary vortices are created behind the bubbles, and the particles experience a stronger spiraling motion.

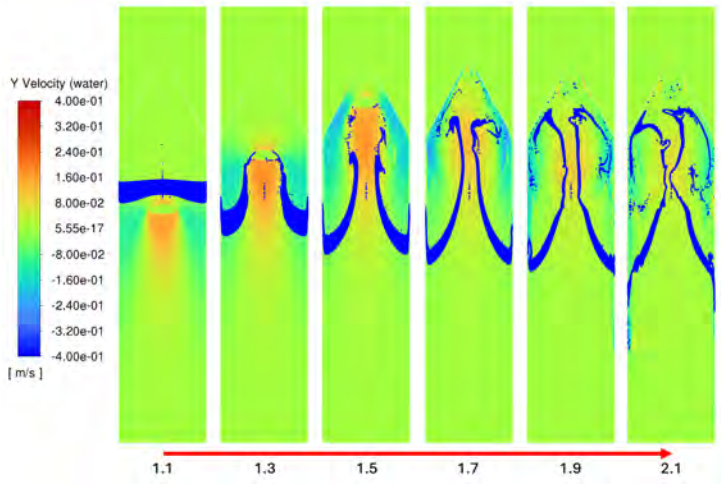

(a)

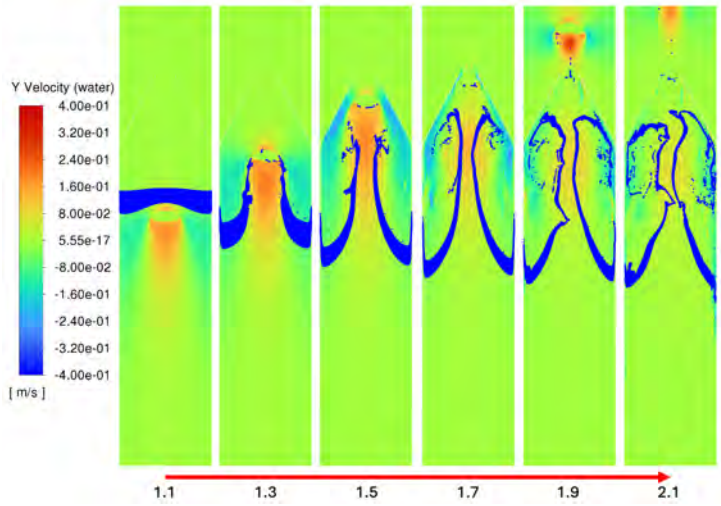

(b)

Figure 4.5.3: Particle lift of $10\ \mu m$ *nickel particles in the large column with collectors* $d_{collector} = 7.5\ mm$, $\theta = 60°$ *(a), and* $d_{collector} = 10\ mm$, $\theta = 61.9°$ *(b), with a bubble with bubble equivalent diameter of* $10\ mm$*, the timeline is given in* s *of flow-time*

If another three bubbles are added into the simulation, the same pattern occurs once more. However, now all three bubbles coalesce into one big bubble, since the wake of the preceding bubbles affect the velocity experienced by the second round of bubbles. This results in a stronger velocity at the right-hand side of the column, which forces the second bubble into the wake of the other two bubbles as well. This results in a strong upwards motion at one side of the column, but a stronger downwards motion at the other side. Additionally, the second round of bubbles, results in a higher dispersion of the particles in the column, resulting in a higher sedimentation rate towards the bottom of the column.

The addition of multiple bubbles increases both velocity profiles in the column as dispersion of particles. However, the effect of multiple bubbles of particle recovery needs further investigation. To be able to simulate a situation which visualizes the effect of multiple bubbles correctly, an inlet should be implemented where bubbles are formed

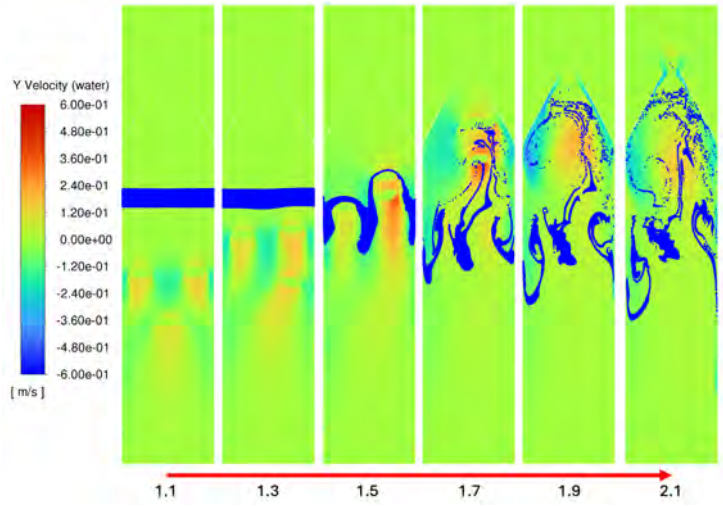

(a)

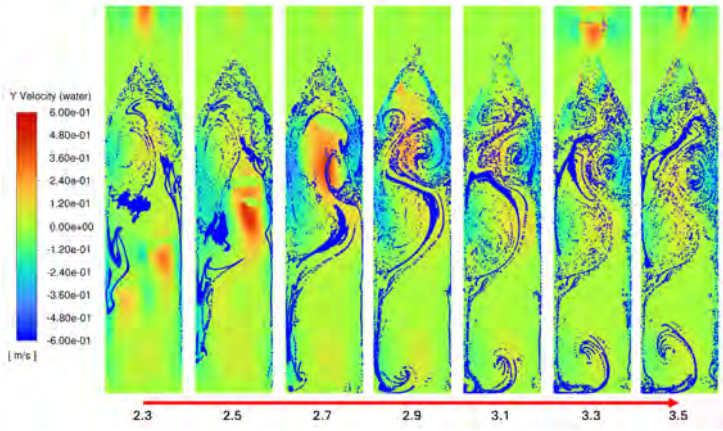

(b)

Figure 4.5.4: Particle lift of $10\ \mu m$ *nickel particles in the large column, with three bubbles with bubble equivalent diameter of* $4.3\ mm$ *(a), and a second round of bubbles (b), with collector with opening diameter of* $10\ mm$ *and angle of* $61.9°$*, the timeline is given in* s *of flow-time.*

based on a continuous flow of gas into the column. An attempt has been made to try and simulate the full bubble column, however convergence issues arose, which could not be solved. Simulating a single bubble has proven to be numerically more stable, regardless still not all simulations converged into a stable solution. To simulate the full bubble column, one should look to alternative software programs than Anys Fluent.

The effect of switching a water and air system towards a molten salt and helium system on particle lift, has been investigated and will be discusses in the next section.

4.5.5. Particle Lift in Bubble Column with Molten-salt and Helium

Figure 4.5.5 visualizes the effect of switching a water and air system towards a molten salt and helium system. From this indeed only small differences in particle lift are noticed. The bubble rise velocity of the helium bubble is larger, which results in higher differences of the velocity of the fluid. Therefore, particles experience a higher down-

wards velocity at the wall, but a higher upwards motion in the middle of the column.

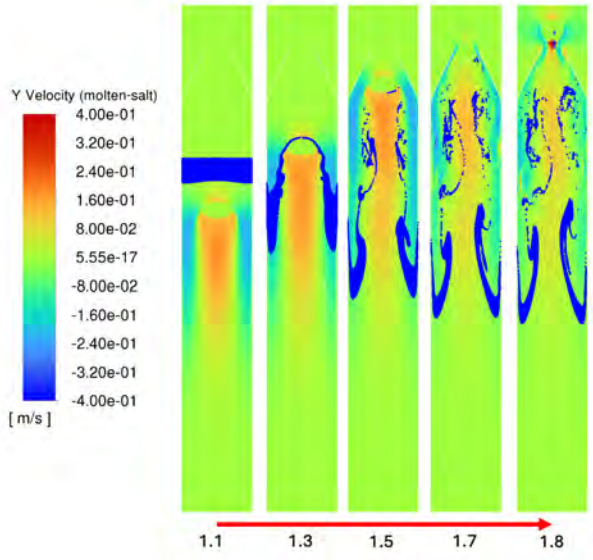

Figure 4.5.5: Particle lift of $10\ \mu m$ *nickel particles in the small column with the addition of a collector with opening diameter of 10 mm and angle* $64.7°$ *and a bubble equivalent diameter of* $10\ mm$ *in molten salt of a helium bubble, the timeline is given in* s *of flow-time.*

Behind the helium bubble, particles experience increased spiraling motion compared to the water and air system. This might be due to the higher bubble rise velocity in the middle of the column. The bubble velocity is dependent on the viscosity of the medium [56]. The dynamic viscosity of molten salt at $700°C$ is higher than that for water, which should decrease the bubble velocity. However the surface tension is higher in molten salt than in water, which increases the velocity. Additionally, the buoyancy force is higher in molten-salt than in water, resulting in a higher bubble rise velocity. Consequently, the increased velocity could impact the vortices formed behind the bubble, which could in turn result in the higher spiraling motion of the particles in the wake of the helium bubble. Additionally, because of the higher bubble rise velocity, the molten salt might require more time to return to a state of zero velocity after the bubble has passed. Hence, the particles experience an extended period of upward velocity within the center of the column, leading to a prolonged upward motion in the molten salt compared to water.

Switching the water and air system to a molten salt and helium system might increase the particle recovery due to a more turbulent wake formed behind the bubble. However, this should be experimentally confirmed.

4.5.6. Particle Lift in 3D

All simulations highlighted in this Section, and in Section 4.4, are performed in 2D. However, the bubble column is not a 2D system, but rather a 3D environment. Some preliminary results have been obtained in 3D, which showed that simulating in 2D

should be an accurate description to understand particle behavior inside the column. Since, simulating in more dimensions, increases the computational time, no further attempts have been made to simulate a 3D situation. However, to be able to fully understand the dynamics of particle lift inside the bubble column, a 3D simulation would be preferable.

CHAPTER 5
CONCLUSIONS AND RECOMMENDATIONS

To be able to meet sustainable energy demands of the future, nuclear power should be included into the possible sources which generate electricity. The MSR is one of the most promising Generation IV techniques currently under investigation. The advantages of the MSR include increased safety, efficiency, economic viability, and possible closure of the fuel cycle. This master thesis has attempted to contribute to the ongoing research in the MSR by investigating the possibility of particle removal of fission products in the MSR through helium bubbling by the exploitation of entrainment. Efficient particle removal of molybdenum will not only prove the proposed on-line helium bubbling mechanism for particle removal, but will help with closing the fuel cycle, so that the MSR produces minimal waste. This section will contain some concluding remarks on the results obtained, and some recommendations for further research.

5.1. Conclusions

The aim of this thesis was to investigate the trade-off between bubble size, particle size, and particle density in particle recovery. To this end, some sub-questions have been answered, which will be discussed shortly in this paragraph, but more elaborately in the upcoming paragraphs. First the mechanism that can be used to recover ultra-fine particles is called entrainment. In this mechanism the particles follow the path of the wake of the bubbles and follow the fluid streamlines to the top of the column. Secondly, higher volume flows are preferable and results in a higher particle recovery. Thirdly, particles in the size range of at least $500\ nm$ until $10\ \mu m$ can be recovered. Lastly, a water and air system is an adequate approximation for a molten salt and helium system.

One of the main concluding remarks of this thesis is that entrainment can be used to recover ultra-fine particles. The volume flows used resulted in large bubble sizes and high bubble rise velocities. Therefore, the Reynolds' numbers were much higher than flotation models developed in literature. Consequently, it can be assumed that no particle-bubble collision occurs in the column, and therefore flotation is minimal. On that account, the particles recovered are solely due to entrainment. Since particle

recovery could possibly reach up to $0.9\ g{\cdot}g^{-1}$, it can be concluded that particle recovery of ultra-fine particles by entrainment is an appropriate mechanism for particle removal in bubble columns.

Bubble size, bubble rise velocity, and bubble trajectories have an influence on particle lift inside the column. The particle lift is independent on particle density or size, and each ultra-fine particle is lifted to the top of the column equally. The main parameters influencing bubble size, hence bubble rise velocity and bubble trajectory, are the volume flow and the inlet size. Higher volume flows and bigger inlet diameter generally resulted in larger bubble sizes. Bigger bubbles generally resulted in higher particle recovery, however, when increasing the inlet size, the particle recovery decreases. This can be allocated to a lower gas hold-up inside the column. A lower gas hold-up results in less bubbles present, therefore, less bubbles that are able to transport particles to the top of the column, hence a decrease in particle recovery.

Particle lift is independent of particle size and particle density, however, sedimentation of particles plays a key role in the recovery of particles inside the collector. Sedimentation can be described by Stokes' law, which indicates that lighter and smaller particles experience a significantly longer sedimentation time. An increase in sedimentation time allows particles to be flushed out of the collector, back into the column, which decreases the particle recovery. This might to some extend be prevented by decreasing the collector opening diameter. Experiments showed that a smaller opening diameter resulted in higher particle recovery. Numerical simulations showed that for a smaller opening diameter of the collector, the particles experienced a higher upwards movement of the particles to the top of the column, further confirming that particle recovery increases with decreasing the opening of the collector.

It has been shown that after a certain amount of time for recovery, a constant maximum is reached for particle recovery. Smaller particles reach a higher R_{max} value than larger particles after. However, larger particles are recovered more quickly than smaller particles. This can be related to an increased sedimentation time of smaller particles, since the sedimentation time of small particles is longer. For optimal particle recovery of small particles, an increase of the time of removal might result in higher particle recovery.

In this thesis, the effect of increasing the diameter of the bubble column was investigated. From this it has become evident that up-scaling of the set-up is not a straightforward process. The particle recovery in the large column was generally lower than in the small column at equal volume flows. This can be assigned to the fact that inside the large column smaller bubbles are formed at the same volume flow, and that the gas hold-up in the large column is smaller than in the small column. To this end, higher volume flows should be investigated in the large column to check whether particle recovery can reach equal heights as in the small column. Otherwise, it will be preferable to implement multiple smaller bubble columns into the MSR for adequate particle removal of non-soluble fission products.

To conclude, the trade-off between bubble size, particle size, and particle density is mainly dependent on volume flow and particle sedimentation time. Higher volume flows generally results in higher particle recovery. Furthermore, due to the longer sed-

imentation time of smaller particles, more time for the removal of particles is needed to reach higher particle recovery.

5.2. Recommendations

The recommendations will be divided into two subcategories. The first one concerns recommendations to improve the research done in this master thesis, and the second one to improve the obtained results in relation to the MSR. First, the recommendations to improve the research done will be discussed.

5.2.1. Improvements in Experimental and Numerical Procedure

To investigate the effect of up-scaling the set-up, higher volume flows should be exploited in the large column. The flow regulator used in this thesis could reach up to $500\ cm^3 \cdot min^{-1}$. This proved to be insufficient for adequate particle removal in the large column. Calculations done by Dr. Ir. Ruben Dewes showed that increasing the volume flow to around $800\ cm^3 \cdot min^{-1}$, would result in a similar gas hold up in the large column as in the small column for $350\ cm^3 \cdot min^{-1}$. Increasing the volume flow could thus result in higher particle recovery in the large column. If particle recovery in the large column increases with increased volume flow, this could indicate that up-scaling of the set-up to an industrial level is straightforward, and the bubble column can than be implemented easily into the MSR design. An alternative to increasing the volume flow to increase the gas hold-up is to increase the number of inlets. Multiple inlets might increase turbulence inside the bubble column, result in less sedimentation, and a higher particle recovery. To investigate the effectiveness of multiple inlets, a model column should be included which could include the possibility of exploiting multiple inlets for bubble formation.

Furthermore, the effect of longer time for particle removal needs further investigation. It has been shown that for smaller particles higher particle removal can be achieved for longer operation time. This suggests, that there is an optimum for removal time. This could indicate whether particle removal of Molybdenum in the MSR is possible. The half-life of Molybdenum-99, which is the precursor of Technetium-99m commonly used in radiotherapy, is $66\ hours$. If a long time is needed before particles can be removed from the MSR, the bubble column might not be sufficient for particle removal in the MSR, since together with storage and transportation many particles will already have decayed. However, if the optimal time of removal is less, particle removal through entrainment would provide a promising technique for the effective removal of particles in the MSR.

In this thesis, data is obtained from single experiments. To increase the accuracy of the experimentally obtained data, the experiments should be repeated. Moreover, increasing the experimentally obtained data would provide measure of deviation encountered in the bubble column, thereby allowing analysis of the error that occurs in the experiments.

Two algorithms have been proposed in this thesis for data analysis. The first one is to determine the bubble size. This algorithm is dependent on the background removal

provided in Mac-Book software. Additionally, the algorithm used requires manual pre-processing of multiple-bubble images into single-bubble images. To be able to determine the bubble sizes computationally, and without the use of a Mac-Book, the algorithm should be altered. To this end, among other things, a deep learning model could be exploited for direct analysis of the bubble sizes. A deep learning model would also decrease the time needed for the analysis, since it extracts the manually performed actions.

The second algorithm used was based on statistical tests. To determine the accuracy of the statistically performed test, it should be investigated when the tests allow for type I and II errors, i.e., false positives or false negatives. Furthermore, a single α value has been used as a cut-off value, but when using multiple tests this α value should be altered accordingly. However, since relatively few tests were performed, this was neglected. This assumption should be validated to improve the accuracy of the fits obtained in the LDA profiles.

A simple numerical model has been proposed to investigate the dynamics of particle recovery inside the bubble column. However, using Ansys Fluent convergence issues arose, therefore it has been argued that using Ansys Fluent might not be the most convenient program to use to build a particle-bubble model. Due to convergence issues, instead of building a model that included a complete description of the bubble column, single bubble simulations have been performed. However, single bubble simulations do not provide a complete description of bubble-particle interactions inside the column. In addition, Ansys Fluent does not provide easy altering of build-in numerical models. Many numerical models have been proposed that describe the bubble-particle interactions. To be able to compare these models with experimentally obtained data, it might be useful to implement the models. However, since Ansys Fluent does not allow easy adaptations in the numerical model, this was not possible in the model proposed in this thesis. Therefore, using a different CFD software, like OpenFOAM, could provide a more accurate model, and might even prevent the convergence issues that were encountered in this thesis.

Apart from changing the software, some alterations into the model can be implemented that could increase the stability and accuracy of the model. This includes the type of mesh, the type of model, and the type of time step, i.e., fixed or adaptive. Further research should be conducted to investigate the effect of altering the model on its ability to convergence and produce accurate results.

5.2.2. Improvements Towards Implementation in a Molten Salt Reactor

To be able to implement the bubble columns into the design of the MSR, some unknown variables need further investigation. Firstly, from numerical simulations it has been argued that switching from a water and air systems towards a molten salt and helium system will not result in profound differences. However, this should be experimentally confirmed. Additionally, when switching to molten salt, the temperature of the molten salt could have an impact on the conditions inside the column, therefore altering the phenomena observed. In this thesis a constant temperature has been assumed, however, this could not be entirely true, resulting in density differences in

the molten salt, which could in turn affect the bubble behavior. Furthermore, Cervi et al. (2019) demonstrated that the helium bubble motion, the propagation of pressure waves in the fuel mixture, and neutronics are strongly coupled [101]. Therefore, to ensure a stable and safe design of the bubble columns, a more complex model should be developed that accounts for all significant processes occurring in the MSR.

Adding to a stable and safe design of the MSR, the gas hold-up in the column could have an effect on the stability of the molten salt core. This effect should be investigated. The implantation of a bubble system into the MSR design is not a straightforward process. The bubble columns will probably include molten salt in which fissionable products have been dispersed. The effect of the collector and gas hold-up in the bubble columns on the criticality of the system should be investigated to ensure a safe and stable design. Furthermore, the collector needs further investigation, and how the particles will be flushed out of the column. This has not been the objective of this thesis, but should be investigated before implementation in the MSR.

BIBLIOGRAPHY

[1] European Union Council. *Climate change: what the EU is doing*. URL: https://www.consilium.europa.eu/en/policies/climate-change/#:~:text=Under%20the%20European%20climate%20law,EU%20climate%20neutral%20by%202050.. (accessed: 22-09-2023).

[2] T et al Stocker. "Technical Summary". In: *Climate Change 2013: The Physical Science Basis* (2013), Contribution of Working Group I to the Fifth Assessment Report of the Intergovernmental Panel on Climate Change.

[3] T. Editors of Encyclopaedia Britannica. *Industrial Revolution*. URL: https://www.britannica.com/money/topic/Industrial-Revolution. (accessed: 22-09-2023).

[4] S. Chu and A. Majumdar. "Opportunities and challenges for a sustainable energy future". In: *Nature* 488 (2012), pp. 294–303. DOI: 10.1038/nature11475.

[5] Hannah Ritchie, Max Roser, and Pablo Rosado. *Energy Production and Consumption*. URL: https://ourworldindata.org/energy-production-consumption#citation. (accessed: 22-09-2023).

[6] IAEA. "The Role of Critical World Energy Outlook Special Report Minerals in Clean Energy Transitions". In: *Climate Change 2013: The Physical Science Basis* (2022).

[7] S. Golroudbary et al. "Global environmental cost of using rare earth elements in green energy technologies". In: *Science of the Total Environment* 832 (2022). DOI: 10.1016/j.scitotenv.2022.155022.

[8] J Korhonen. *Climate Gamble, Carbon intensity of electric power sources (Weekly pic)*. 2015. URL: https://climategamble.net/tag/renewables/. (accessed: 16-02-2024).

[9] KIWI ENERGY. *Pros and Cons of Nuclear Energy*. URL: https://kiwienergy.us/pros-and-cons-of-nuclear-energy/. (accessed: 29-03-2024).

[10] NEA and IEA. "Technology Roadmap Nuclear Energy". In: *IEA and NEA Secretariat* (2015).

[11] J. Duderstadt and L. Hamilton. *Nuclear Reactor Analysis*. John Wiley & Sons, Inc., 1976. ISBN: 0-471-22363-8.

[12] IEA and OECD NEA. *Projected Costs of Generating Electricity*. 202. URL: https://www.iea.org/reports/projected-costs-of-generating-electricity-2020. (accessed: 02-04-2024).

[13] V. Ignatiev et al. "Molten-salt reactors: new possibilities, problems and solutions". In: *Atomic Energy* 112 (3) (2012). DOI: 10.1007/s10512-012-9537-2.

[14] B. Brook et al. "Why nuclear energy is sustainable and has to be part of the energy mix". In: *Sustainable Materials and Technologies* 1-2 (2014), pp. 8–16. DOI: 10.1016/j.susmat.2014.11.001.

[15] SNETP. *Discover the MIMOSA Project*. URL: https://snetp.eu/2022/10/19/mimosa-project-developing-a-multi-recycling-strategy-for-spent-nuclear-fuels/#. (accessed: 01-03-2024).

[16] G. Locatelli, M. Mancini, and N. Todeschini. "Generation IV nuclear reactors: Current status and future prospects". In: *Energy Policy* 61 (2013), pp. 1503–1520. DOI: 10.1016/j.enpol.2013.06.101.

[17] K. Furukawa et al. "Thorium Molten-Salt Nuclear Energy Synergetics". In: *Journal of Nuclear Science and Technology* 27 (12) (1990), pp. 1157–1178. DOI: 10.1080/18811248.1990.9731310.

[18] R. Roper et al. "Molten salt for advanced energy applications: A review". In: *Annals of Nuclear Energy* 169 (2022). DOI: 10.1016/j.anucene.2021.108924.

[19] D. Chavez et al. "Experimental investigation of single helium bubbles rising in FLiNaK molten salt". In: *International Journal of Heat and Fluid Flow* 92 (2021). DOI: 10.1016/j.ijheatfluidflow.2021.108875.

[20] S. Walker and J. Wei. "Species transport analysis of noble metal fission product transport, deposition, and extraction in the molten salt reactor experiment". In: *Annals of Nuclear Energy* 158 (2021). DOI: 10.1016/j.anucene.2021.108250.

[21] IAEA. "A Technology Roadmap for Generation IV Nuclear Energy Systems". In: *U.S. DOE Nuclear Energy Research Advisory Committee and the Generation IV International Forum* (2002).

[22] D. Zhao et al. "On the viscosity of molten salts and molten salt mixtures and its temperature dependence". In: *Journal of Energy Storage* 61 (2023). DOI: 10.1016/j.est.2023.106707.

[23] R. Kedl. "The migration of a class of fission products (noble metals) in the molten-salt reactor experiment". In: *Molten-Salt Reactor Program* (1972).

[24] Z. Mausolff, M DeHart, and S. Goluoglu. "Design and assessment of a molten chloride fast reactor". In: *Nuclear Engineering and Design* 379 (2021). DOI: 10.1016/j.nucengdes.2021.111181.

[25] D. Gérardin et al. "Design Evolutions of the Molten Salt Fast Reactor". In: ().

[26] J. Serp et al. "The molten salt reactor (MSR) in generation IV: Overview and perspectives". In: *Progress in Nuclear Energy* 77 (2014), pp. 308–319. DOI: 10.1016/j.pnucene.2014.02.014.

[27] K. Sridharan and T. Allen. “Corrosion in Molten Salts”. In: *Elsevier* (2013), pp. 241–267. DOI: 10.1016/B978-0-12-398538-5.00012-3.

[28] E. Compere et al. “Fission Product Behavior in the Molten Salt Reactor Experiment”. In: *Oak Ridge National Laboratory* (1975).

[29] E. Cervi et al. “Multiphysics analysis of the MSFR helium bubbling system: A comparison between neutron diffusion,SP_3 neutron transport and Monte Carlo approaches”. In: *Annals of Nuclear Energy* 132 (2019), pp. 227–235. DOI: 10.1016/j.anucene.2019.04.029.

[30] S. Delpech et al. “Reactor physics and reprocessing scheme for innovative molten salt reactor system”. In: *Journal of Fluorine Chemistry* 130 (2009), pp. 11–17. DOI: 10.1016/j.jfluchem.2008.07.009.

[31] M. Stoddard, J. Harb, and M. Memmott. “Numerical analysis of isotope production in molten salt reactors: A case study for Molybdenum-99 production”. In: *Annals of Nuclear Energy* 129 (2019), pp. 56–61. DOI: 10.1016/j.anucene.2019.01.021.

[32] G. Hewitt. “Multiphase Flow”. In: *Thermopedia* (2010). DOI: 10.1615/AtoZ.m.multiphase_flow.

[33] S. Cheung, G. Yeoh, and J. Tu. “A Review of Population Balance Modelling for Isothermal Bubbly Flows”. In: *Journal of Computational Multiphase Flows* 1 (2) (2009), pp. 420–437.

[34] G. Besagni, N. Varallo, and R. Mereu. “Computational Fluid Dynamics Modelling of Two-Phase Bubble Columns: A Comprehensive Review”. In: *Fluids* 8 (91) (2023). DOI: 10.3390/fluids8030091.

[35] G. Corchero, J. Montañés, and C. Téllez. “Effect of flow rate conditions on bubble formation”. In: *International Journal of Heat and Mass Transfer* 55 (2012), pp. 5044–5052. DOI: 10.1016/j.ijheatmasstransfer.2012.05.002.

[36] M. Ruzicka et al. “Effect of bubble column dimensions on flow regime transition”. In: *Chemical Engineering Science* 56 (2001), pp. 6117–6124. DOI: 10.1016/S0009-2509(01)00215-9.

[37] S. Orvalho et al. “Flow regimes in slurry bubble column: Effect of column height and particle concentration”. In: *Chemical Engineering Journal* 351 (2018), pp. 799–815. DOI: 10.1016/j.cej.2018.06.115.

[38] J. Kim et al. “Gas holdup and hydrodynamic flow regime transition in bubble columns”. In: *Journal of Industrial and Engineering Chemistry* 56 (2017), pp. 450–462. DOI: 10.1016/j.jiec.2017.07.043.

[39] Y. Hur et al. “Origin of regime transition to turbulent flow in bubble column: Orifice- and column-induced transitions”. In: *International Journal of Multiphase Flow* 50 (2013). DOI: 10.1016/j.ijmultiphaseflow.2012.11.001.

[40] P. Wang et al. “Effect of Particle Size on the Rising Behavior of Particle-Laden Bubbles”. In: *Langmuir* 35 (2019), pp. 3680–3687. DOI: 10.1021/acs.langmuir.8b04112.

[41] M. Jamialahmadi et al. “Study of bubble formation under constant flow conditions”. In: *Trans IChemE* 79 (2001), pp. 523–532.

[42] X. Jian, C. Zhu, and H. Li. “Bubble pinch-off in Newtonian and non-Newtonian fluids”. In: *Chemical Engineering Science* 170 (2017), pp. 98–104. DOI: 10.1016/j.ces.2016.12.057.

[43] N. Hassan, M. Khan, and M. Rasul. “A study of bubble trajectort and drag co-efficient in water and non-newtonian fluids”. In: *Wseas transations on fluid mechanics* 3 (3) (2008). DOI: 10..

[44] M. Götz et al. “Novel gas holdup correlation for slurry bubble column reactors operated in the homogeneous regime”. In: *Chemical Engineering Journal* 308 (2017), pp. 1209–1224. DOI: 10.1016/j.cej.2016.09.101.

[45] R. Schäfer, C. Merten, and G. Eigenberger. “Bubble size distributions in a bubble column reactor under industrial conditions”. In: *Experimental Thermal and Fluid Science* 26 (2002), pp. 595–604. DOI: 10.1016/S0894-1777(02)00189-9.

[46] S Mohagheghian and B Elbing. “Characterization of Bubble Size Distributions within a Bubble Column”. In: *Fluids* 3 (2018). DOI: 10.3390/fluids3010013.

[47] A. Gordiychuk et al. “Size distribution and Sauter mean diameter of micro bubbles for a Venturi type bubble generator”. In: *Experimental Thermal and Fluid Science* 70 (2016), pp. 51–60. DOI: 10.1016/j.expthermflusci.2015.08.014.

[48] W. Luewisutthichat, A. Tsutsumi, and K. Yoshida. “Bubble characeristics in multiphase flow systems: bubble sizes and size distributions”. In: *Journal of chemical engineering of Japan* 30 (3) (1997).

[49] P. Kowalczuk and J. Drzymala. “Physical Meaning of the Sauter Mean Diameter of Spherical Particulate Matter”. In: *Particulate science and technology* 34 (6) (2016), pp. 645–647. DOI: 10.1080/02726351.2015.1099582.

[50] E. Amini et al. “Influence of turbulence kinetic energy on bubble size in different scale flotation cells”. In: *Minerals Engineering* 45 (2013), pp. 146–150. DOI: 10.1016/j.mineng.2013.01.015.

[51] J. Wang, G. Forbes, and E. Forbes. “Frother Characterization Using a Novel Bubble Size Measurement Technique”. In: *Applied Sciences* 12 (2022). DOI: 10.3390/app12020750.

[52] D. Kosior et al. “Bubble Formation and Motion in Liquids - A Review”. In: *Minerals* 13 (1130) (2023). DOI: 10.3390/min13091130.

[53] S. Park et al. “A Simple Parametrization for the Rising Velocity of Bubbles in a Liquid Pool”. In: *Nuclear Engineering and Technology* 49 (2017), pp. 692–699. DOI: 10.1016/j.net.2016.12.006.

[54] M. Islam et al. “A single air bubble rise in water: a CFD study”. In: *Mechanical Engineering Research Journal* 9 (2013), pp. 1–6.

[55] R. Krishna et al. “Rise velocity of a swarm of large gas bubbles in liquids”. In: *Chemical Engineering Sciences* 54 (1999), pp. 171–183.

[56] P Kováts, D. Thévenin, and K. Zähringer. “Influence of viscosity and surface tension on bubble dynamics and mass transfer in a model bubble column”. In: *International Journal of Multiphase Flow* 123 (2020). DOI: 10.1016/j.ijmultiphaseflow.2019.103174.

[57] D. Langevin. “Bubble coalescence in pure liquids and in surfactant solutions”. In: *Current Opinion in Colloid & Interface Science* (2015), pp. 92–97. DOI: 10.1016/j.cocis.2015.03.005.

[58] R. Kirkpatrick and M. Lockett. “The influence of approach velocity on bubble coalescence”. In: *Chemical Engineering Science* 29 (1974), pp. 2363–2372.

[59] R. Clift, J. Grace, and M. Weber. *Bubbles, Drops, and Particles*. Academic Press, Inc., 1978. ISBN: 0-12-176950-X.

[60] R. Prakash, S. Kumar-Majumder, and A. Singh. “Flotation technique: Its mechanisms and design parameters”. In: *Chemical Engineering and Processing* 127 (2018), pp. 249–270. DOI: 10.1016/j.cep.2018.03.029.

[61] S. Farrokhpay, L. Fillipov, and D. Fornasiero. “Flotation of Fine Particles: A Review”. In: *Mineral Processing and Extractive Metallurgy Review* 42.7 (2021), pp. 473–483. DOI: 10.1080/08827508.2020.1793140.

[62] A. Nguyen, J. Ralston, and H. Schulze. “On modelling of bubble-particle attachment probability in flotation”. In: *Int. J. Miner. Process* 5 (1998), pp. 225–249.

[63] T. Miettinen, J. Ralston, and D. Fornasiero. “The limits of fine particle flotation”. In: *Minerals Engineering* 23 (2010), pp. 420–437. DOI: 10.1016/j.mineng.2009.12.006.

[64] A. Nguyen, H. Schulze, and J. Ralston. “Elementary steps in particle-bubble attachment”. In: *Int. J. Miner. Process* 51 (1997), pp. 183–195.

[65] L. Wang et al. “A review of entrainment: Mechanisms, contributing factors and modelling in flotation”. In: *Minerals Engineering* 70 (2015), pp. 77–91. DOI: 10.1016/j.mineng.2014.09.003.

[66] Encyclopaedia Britannica. *Stokes’s law*. URL: https://www.britannica.comhttps//www.britannica.com/science/Stokess-law. (accessed: 06-03-2024).

[67] The entrainment factor in froth flotation: Model for particle size and other operating parameter effects. “Neethling, S. and Cilliers, J.” In: *Int. J. Miner. Process.* 93 (2009), pp. 141–148. DOI: 10.1016/j.minpro.2009.07.004.

[68] J. Meng et al. “A review of turbulence measurement techniques for flotation”. In: *Minerals Engineering* 95 (2016), pp. 79–95. DOI: 10.1016/j.mineng.2016.06.007.

[69] I. Ayranci et al. “Effect of particle polydispersity on particle concentration measurement by using laser Doppler anemometry”. In: *Experimental Thermal and Fluid Science* 31 (2007), pp. 839–847.

[70] LibreTexts Physics. *The Doppler Effect*. URL: https://phys.libretexts.org/Bookshelves/University_Physics/University_Physics_(OpenStax)/Book%3A_University_Physics_I_-_Mechanics_Sound_Oscillations_and_Waves_(OpenStax)/17%3A_Sound/17.08%3A_The_Doppler_Effect. (accessed: 07-03-2024).

[71] J. Abbiss, T. Chubb, and E. Pike. "Laser Doppler anemometry". In: *Optics and Laser Technology* (1974).

[72] Dantec Dynamics. *Measurement Principles of LDA*. URL: https://www.dantecdynamics.com/solutions/fluid-mechanics/laser-doppler-anemometry-lda/measurement-principles-of-lda/. (accessed: 16-01-2024).

[73] "Experimental Economics, Lecture 5: Statistical Tests in Experiments". In: (2023).

[74] T. Quirk. *Excel 2007 for Educational and Psychological Statistics*. Springer, 2012. ISBN: 978-1-4614-3724-6.

[75] T. Lim and W. Loh. "A comparison of tests of equality of variances". In: *Computational Statistics & Data Analysis* 22 (1996), pp. 287–301.

[76] M. Fagerland. "t-tests, non-parametric tests, and large studies - a paradox of statistical practice?" In: *BMC Medical Research Methodology* 12(78) (2012). DOI: 10.1186/1471-2288-12-78.

[77] M. Xu et al. "The differences and similarities between two-sample t-test and paired t-test". In: *Shanghai Archives of Psychiatry* 29 (3) (2017), pp. 184–188. DOI: 10.11919/j.issn.1002-0829.217070.

[78] T. Sakai. "Two Sample T-tests for IR Evaluation: Student or Welch". In: (2016). DOI: 10.1145/2911451.2914684.

[79] T. Kim and J. Park. "More about the basic assumptions of t-test: normality and sample size". In: *Korean Journal of Anesthesiology* 72 (4) (2019). DOI: 10.4097/kja.d.18.00292.

[80] E. Fein et al. *Statistics for Research Students*. University of Southern Queensland, 2022. ISBN: 978-0-6453261-0-9.

[81] T. Kim. "Understanding one-way ANOVA using conceptual figures". In: *Korean Journal of Anesthesiology* 70 (1) (2017).

[82] E. Ostertagová, O. Ostertag, and J. Kovác. "Methodology and Application of the Kruskal-Wallis Test". In: *Applied Mechanics and Materials* (2014). DOI: 10.4028/www.scientific.net/AMM.611.115.

[83] ANSYS FLUENT. *Theory Guide, Release 12.0*. ANSYS, Inc., 2009. Chap. 1. Basic Fluid Flow.

[84] ANSYS FLUENT. *Theory Guide, Release 12.0*. ANSYS, Inc., 2009. Chap. 16. Multiphase Flows.

[85] ANSYS FLUENT. *Theory Guide, Release 12.0*. ANSYS, Inc., 2009. Chap. 15. Discrete Phase.

[86] ANSYS FLUENT. *Theory Guide, Release 12.0*. ANSYS, Inc., 2009. Chap. 4. Turbulence.

[87] Wikipedia. *Neutral buoyancy*. URL: https://en.wikipedia.org/wiki/Neutral_buoyancy. (accessed: 22-03-2024).

[88] SciPy v1.12.0 Manual. *scipy.optimize.least_squares*. URL: https://docs.scipy.org/doc/scipy/reference/generated/scipy.optimize.least_squares.html. (accessed: 22-03-2024).

[89] Cole's classroom. *How to Calculate Crop Factor*. URL: https://colesclassroom.com/calculate-crop-factor/#:~:text=The%20easiest%20way%20to%20do,75mm%20(50mm%20x%201.5).. (accessed: 16-02-2024).

[90] Nikon. *Z50*. URL: https://imaging.nikon.com/imaging/lineup/mirrorless/z_50/. (accessed: 16-02-2024).

[91] D. Mathies. *Full Frame vs. APS-C and MFT: Crop factor explained*. URL: https://prophotosupply.com/blogs/resources/full-frame-vs-aps-c-and-mft-crop-factor-explained#. (accessed: 19-02-2024).

[92] A. Riquelme et al. "Predictive control of the bubble size distribution in a two-phase pilot flotation column". In: *Minerals Engineering* 89 (2016), pp. 71–76. DOI: 10.1016/j.mineng.2016.01.014.

[93] R. Panjipour, M. Karamoozian, and B. Albijanic. "Investigations of gas holdup, interfacial area of bubbles and bubble size distributions in a pilot plant flotation column". In: *Minerals Engineering* 164 (2021). DOI: 10.1016/j.mineng.2021.106819.

[94] CEMS DSC. *The R Squared Value of a Fit*. URL: https://docs.cems.umn.edu/data-plot-tips/R_squared.html. (accessed: 12-03-2024).

[95] SciPy documentation 1.13.0. *scipy.stats.levene*. URL: https://docs.scipy.org/doc/scipy/reference/generated/scipy.stats.levene.html. (accessed: 04-04-2024).

[96] StellarNet Inc. *What is Full Width at Half Maximum (FWHM)?* URL: https://www.stellarnet.us/what-is-full-width-at-half-maximum-fwhm/#:~:text=The%20full%20width%20at%20half,is%20about%202.4%20standard%20deviations.. (accessed: 12-03-2024).

[97] K. Grjotheim et al. "Surface Tension of Liquid Binary and Ternary Chloride Mixtures". In: *Acta chemica scandinavica* 26 (5) (1972), pp. 2050–2062.

[98] E. Olmos et al. "Description of flow regime transitions in bubble columns via laser Doppler anemometry signals processing". In: *Chemical Engineering Science* 58 (2003). DOI: 10.1016/S0009-2509(03)00002-2.

[99] H. Deng, R. Mehta, and G. Warren. "Numerical modeling of flows in flotation columns". In: *Int. J. Miner. Process.* 48 (1996), pp. 61–71.

[100] J. Crha et al. "Comparison of Two Solvers for Simulation of Single Bubble Rising Dynamics: COMSOL vs. Fluent". In: *Minerals* 11 (2021). DOI: 10.3390/min11050452.

[101] E. Cervi et al. "Development of a multiphysics model for the study of fuel compressibility effects in the Molten Salt Fast Reactor". In: *Chemical Engineering* 193 (2019), pp. 379–393. DOI: 10.1016/j.ces.2018.09.025.

APPENDIX

A. Additional Experimental Information

A.1. Particle Rinsing and Particle Ejection

Figure A1 depicts the before particle recovery, after particle recovery, and after rinsing $500\ nm$ nickel particles out of the collector. As can be seen, the particles tend to stick to the collector, and a lot of particles still remain inside the collector after rinsing the particles out. This could result in an underestimation of particle recovery of $500\ nm$ particles.

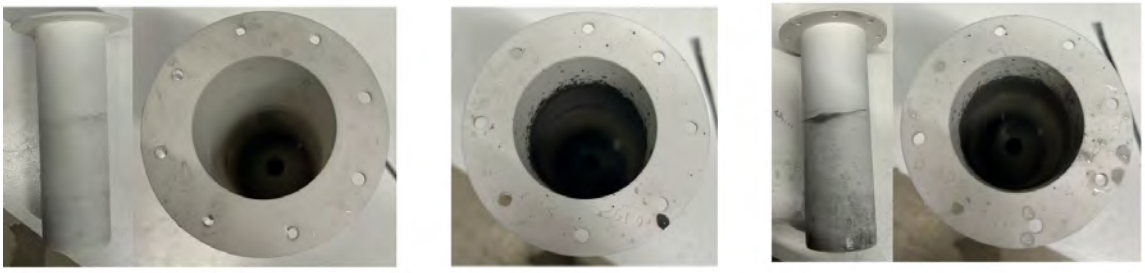

Figure A1: $500\ nm$ *nickel particles before particle collection, after particle collection, and after rinsing.*

Figure A2 depicts the amount of zinc-oxide particles that were ejected out of the column at higher volume flows. This could result in an underestimation of particle recovery of zinc-oxide particles.

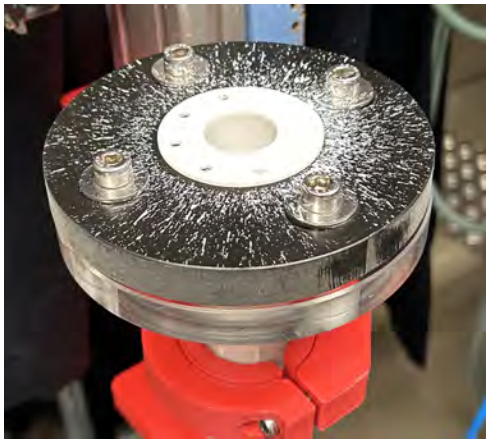

Figure A2: $10\ \mu m$ *of zinc-oxide with* $7.5\ mm$ *collector and inlet diameter of* $1\ mm$ *at volume flow of* $300\ cm^3 \cdot s^{-1}$. *Many particles were ejected out of the column, leading to an underestimation of particles recovered.*

A.2. Bubble Sizes Bottom of the Column

Figure A3 shows the bubble size distribution at formation of the bubbles, so at the inlet at the bottom of the column.

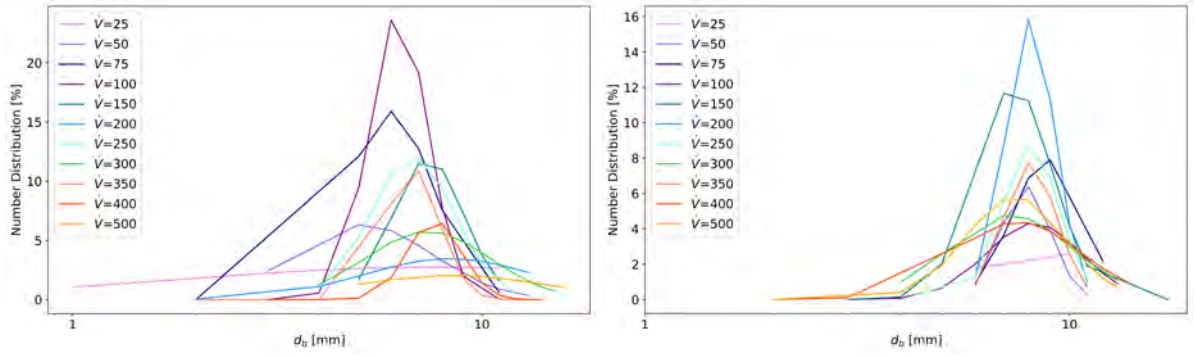

(a) *(b)*

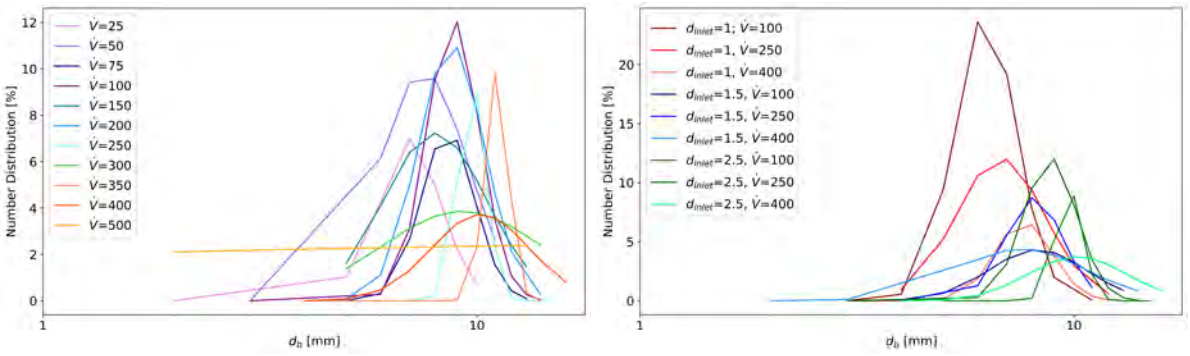

(c) *(d)*

Figure A3: Log-normal distribution fitted through experimentally obtained bubble chord lengths at different volume flows for the small column for inlet diameters 1 mm (a), 1.5 mm (b), and 2.5 mm (c), and a comparison for selected volume flows at the three different inlet sizes (d). The unit of the volume flow is $cm^3 \cdot min^{-1}$. The R^2 values of the fits can be found in Table A2.

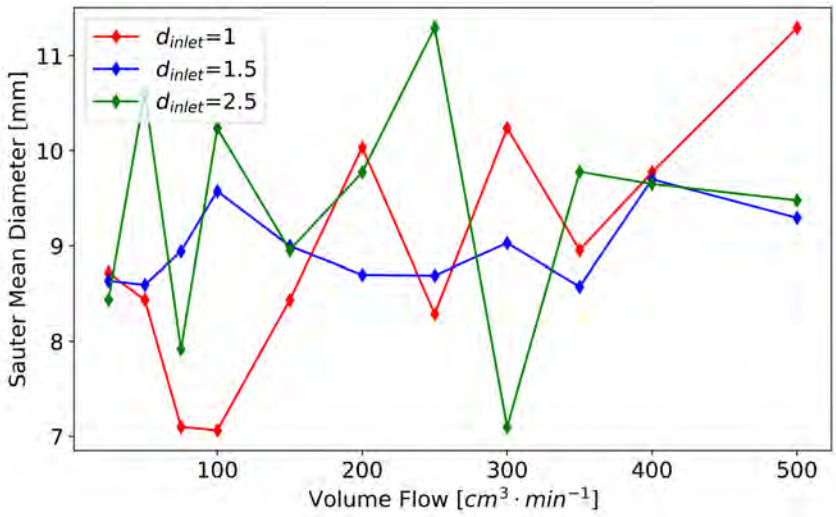

Figure A4: Sauter mean diameter for bubble size distribution at the bottom of the small column for different volume flows. The inlet diameter is given in mm.

A.3. Bubble Size Distribution that Visualizes Two-peaked Distribution

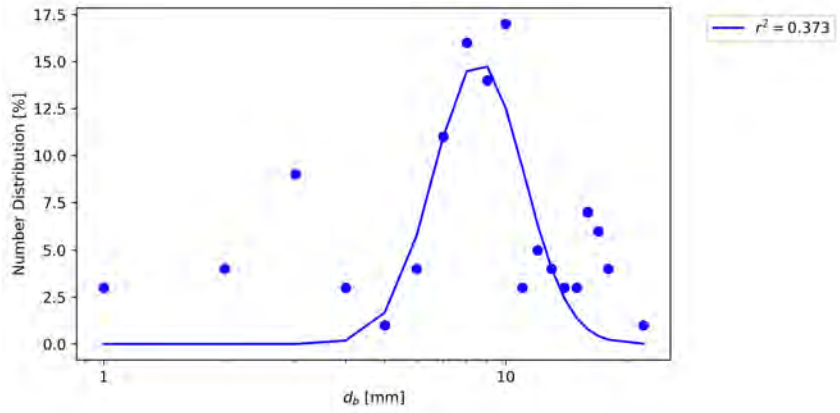

Figure A5: Bubble size distribution for bubbles measured at volume flow of 300, inlet diameter of 1.5. From here it becomes evident that for this bubble size distribution the fit would probably benefit from a two-peaked distribution rather than a one-peak distribution.

A.4. Additional LDA velocity profiles

Here additional velocity profiles obtained by LDA can be found.

A.4.1. Small Column

Figure A6 shows the velocity of glass beads in the small column with a collector with opening diameter of $10\ mm$ and angle $64.7°$. Figure A7a shows the velocity distribution of different particles in the small column with an inlet diameter of $1.5\ mm$, and Figure A7b with an inlet diameter of $2.5\ mm$. In Figures A8a and A8c the FWHM is visualized, and Figures A8b and A8d show the velocity at the peak.

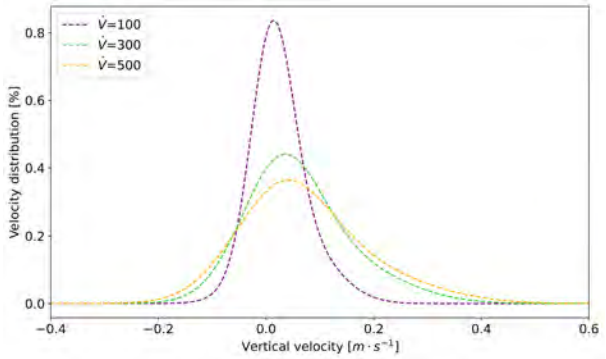

Figure A6: Velocity distribution in vertical direction for glass beads with inlet size of 1 mm in diameter, for small column, with collector with 10 mm opening diameter and angle of 64.7°.

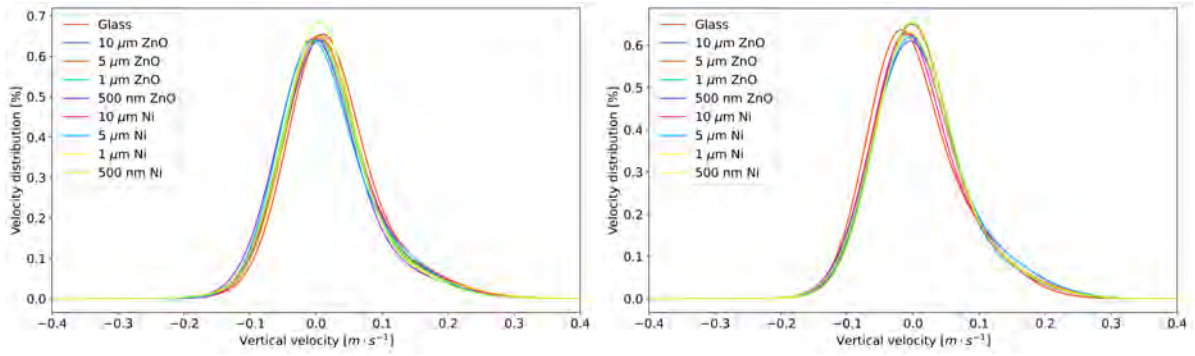

(a) *(b)*

Figure A7: Velocity distribution in vertical direction for small column with inlet diameter of $1.5\ mm$ *(a), and* $2.5\ mm$ *(b) at a volume flow of* $100\ \ cm^3 \cdot min^{-1}$ *for different particles.*

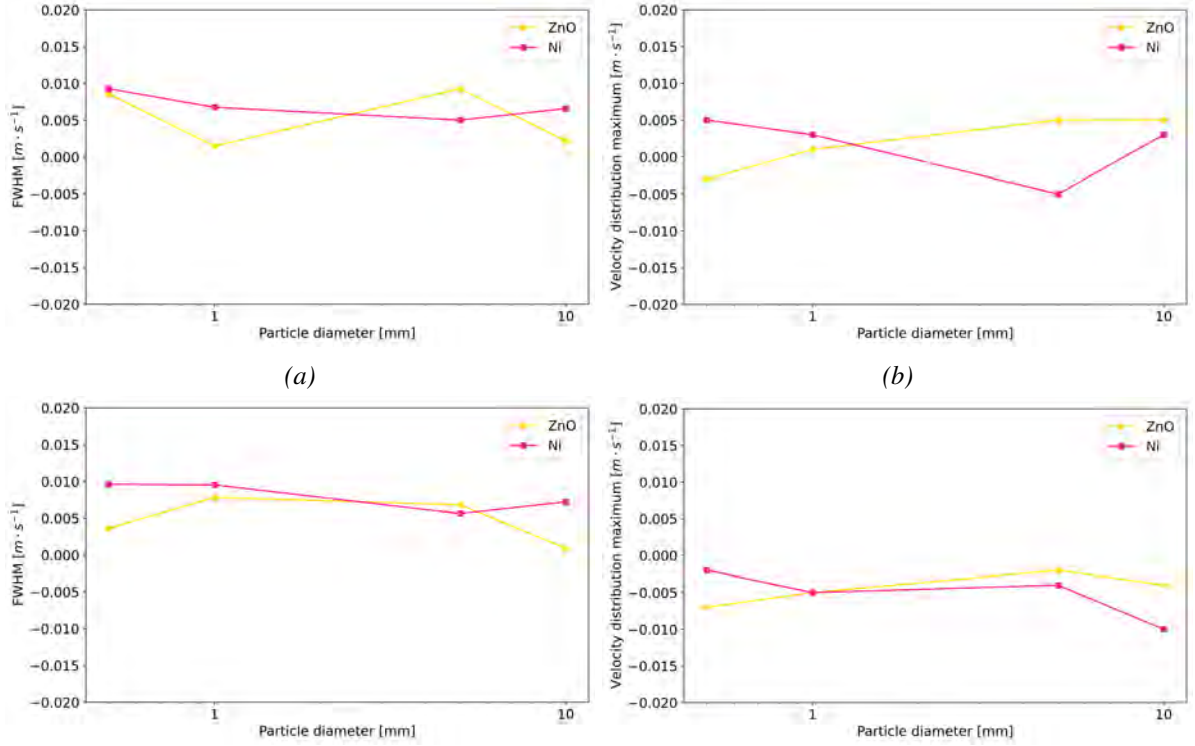

(a) *(b)*

(c) *(d)*

Figure A8: FWHM of velocity profiles in vertical direction with inlet diameter of $1.5\ mm$ *(a), and* $2.5\ mm$ *(c) for different particles with volume flow of* $100\ \ cm^3 \cdot min^{-1}$*, and the velocity at the maximum of the velocity distribution with inlet diameter* $1.5\ mm$ *(b) and* $2.5\ mm$ *(d) for Figure A7.*

A.4.2. Large Column

Figures A9a, A9b, A9c show the velocity of nickel particles in the large column with a collector with opening diameter of $10\ mm$ and angle $61.9°$ for a volume flow 350, 450, and $500\ \ cm^3 \cdot min^{-1}$, respectively. In Figure A10 the corresponding FWHM and velocity at maximum can be found.

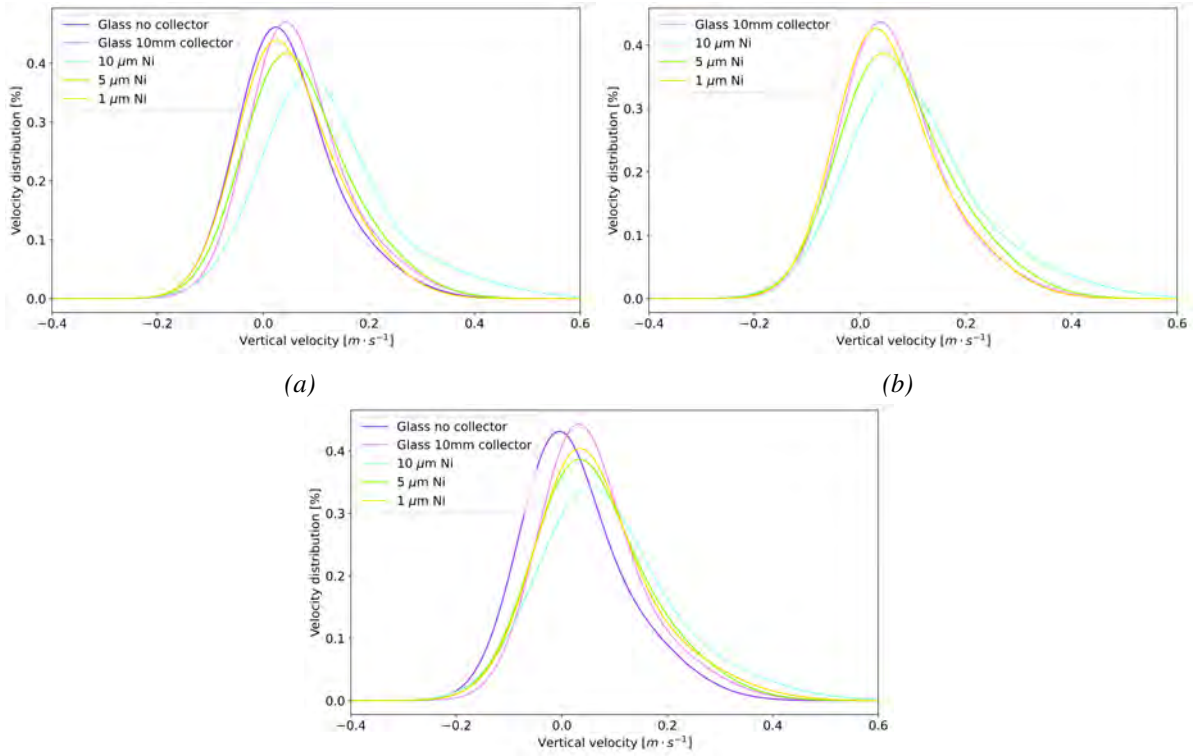

(a) *(b)*

(c)

Figure A9: Velocity distribution in vertical direction for large column with inlet diameter of $1\ mm$ *for nickel particles with volume flow of* 350 *(a),* 450 *(b), and* $500\ \ cm^3 \cdot min^{-1}$ *(c).*

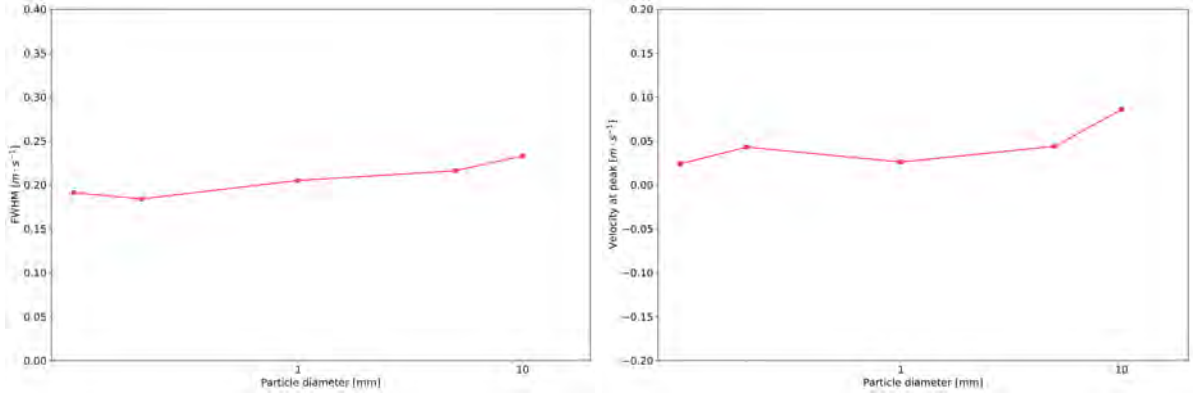

(a) *(b)*

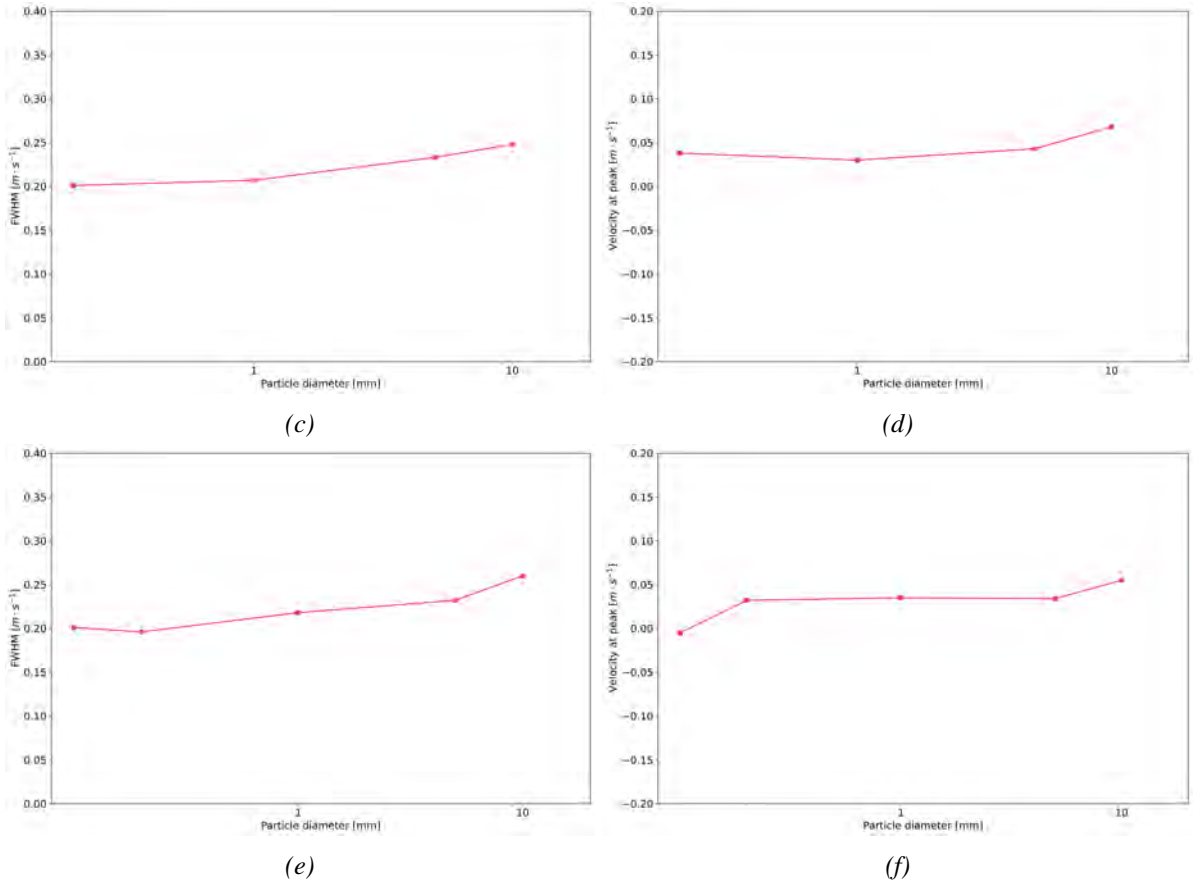

Figure A10: FWHM of velocity profiles in vertical direction of large column with inlet diameter of $1\ mm$ *for different particles with volume flow of* 350 *(a),* 450 *(c), and* $500\ \ cm^3 \cdot min^{-1}$ *(e) and velocity at maximum of velocity profiles in vertical direction of large column with inlet diameter of* $1\ mm$ *for different particles with volume flow of* 350 *(b),* 450 *(d), and* $500\ \ cm^3 \cdot min^{-1}$ *(f) for Figure A9.*

A.5. Particle Recovery at Different Volume Flows

Figure A11 shows particle recovery for some tested conditions. This Figure shows that lowering the volume flow decreases the particle recovery, whereas increasing the volume flow also increases particle recovery.

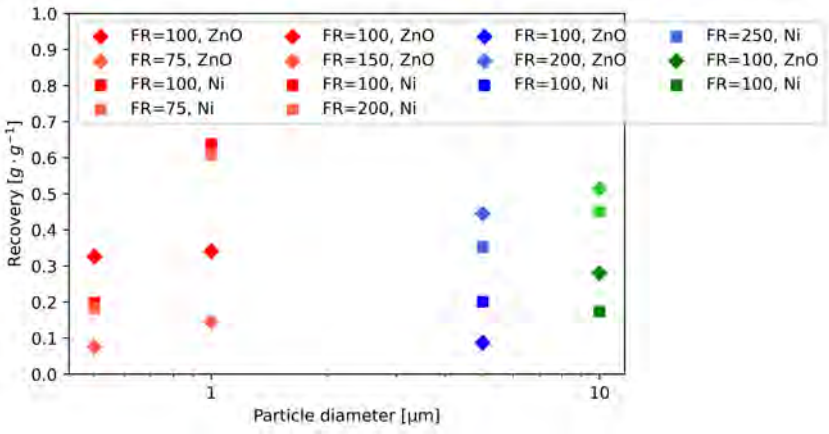

Figure A11: Particle recovery at different conditions in small column.

A.6. Sedimentation Time

Table A1 shows the sedimentation time and velocity for different particles in the small and the large column.

Table A1: Sedimentation time for different particles in the small and the large column, velocity calculated as described in Equation 2.37.

w_{column} $[mm]$	Particle	$d_{particle}$ [µm]	$v_{sedimentation}$ $[cm \cdot s^{-1}]$	$t_{sedimentation}$ [min]
30	ZnO	10	0.113	1.180
30	ZnO	5	0.0282	4.720
30	ZnO	1	0.00113	118.0
30	ZnO	0.5	0.000282	472.0
50	ZnO	10	0.113	1.770
50	ZnO	5	0.0282	7.080
50	ZnO	1	0.00113	177.0
50	ZnO	0.5	0.000282	708.0
30	Ni	10	0.194	0.6888
30	Ni	5	0.0484	2.755
30	Ni	1	0.00194	68.88
30	Ni	0.5	0.000484	275.5
50	Ni	10	0.194	1.033
50	Ni	5	0.0484	4.133
50	Ni	1	0.00194	103.3
50	Ni	0.5	0.000484	413.3

A.7. R^2 Values from Fits

In this section all R^2 values of the different equations fitted for obtained data can be found.

A.7.1. R^2 values bubble size distributions

This section concerns the R^2 values for the bubble size distributions.

Table A2: All R^2 values for bubble size distributions.

Inlet	$\dot{V}$ $[cm^3 \cdot min^{-1}]$	w_{column} [mm]	R^2 middle	R^2 bottom	# bubbles analyzed middle/bottom
1	25	30	0.349	0.0966	94/22
1	50	30	0.419	0.845	114/26
1	75	30	0.976	0.983	164/51
1	100	30	0.990	0.987	102/66
1	150	30	0.929	0.815	122/44
1	200	30	0.897	0.406	131/28
1	250	30	0.839	0.837	136/49
1	300	30	0.473	0.728	107/38
1	350	30	0.533	0.813	110/38
1	400	30	0.835	0.600	112/28
1	500	30	0.855	0.148	114/15
1.5	25	30	0.797	0.083	82/12
1.5	50	30	0.663	0.909	107/18
1.5	75	30	0.201	0.952	93/22
1.5	100	30	0.958	0.460	164/26
1.5	150	30	0.907	0.847	119/49
1.5	200	30	0.865	0.883	124/45
1.5	250	30	0.878	0.910	116/28
1.5	300	30	0.373	0.600	118/20
1.5	350	30	0.623	0.941	113/23
1.5	400	30	0.547	0.462	118/26
1.5	500	30	0.339	0.531	108/27
2.5	25	30	0.771	0.966	96/18
2.5	50	30	0.706	0.555	96/41
2.5	75	30	0.806	0.624	103/29
2.5	100	30	0.743	0.918	134/43
2.5	150	30	0.734	0.659	120/39
2.5	200	30	0.600	0.871	100/45
2.5	250	30	0.699	0.606	107/27
2.5	300	30	0.339	0.435	97/30
2.5	350	30	0.367	0.648	97/27
2.5	400	30	0.430	0.415	99/26
2.5	500	30	0.208	0.007	91/23
1	25	50	0.933	-	92/-
1	50	50	0.849	-	107/-
1	75	50	0.613	-	116/-
1	100	50	0.928	-	126/-
1	150	50	0.984	-	163/-

1	200	50	0.869	-	102/-
1	250	50	0.894	-	115/-
1	300	50	0.719	-	105/-
1	350	50	0.919	-	104/-
1	400	50	0.423	-	107/-
1	450	50	0.583	-	130/-
1	500	50	0.528	-	105/-

A.7.2. LDA Velocity Profiles

Here R^2 values of LDA velocity distributions fitted by a double Gaussian distribution can be found. Additionally, the statistical test result is displayed. Figure A3 visualizes the data for glass beads, Figure A4 for the different particles in the small column, and Figure A5 for nickel particles in the large column.

Table A3: Data glass beads small and large column, w_{column} is given in mm, $d_{collector}$ in mm, $\Theta_{collector}$ in $^\circ$, and $\dot{V}$ in $cm^3 \cdot min^{-1}$.

w_{column}	$d_{collector}$	$\Theta_{collector}$	$\dot{V}$	Statistical Result	R^2
30	-	-	25	ANOVA valid, all data merged	0.9941
30	-	-	50	ANOVA valid, all data merged	0.9937
30	-	-	75	ANOVA valid, all data merged	0.9949
30	-	-	100	ANOVA valid, all data merged	0.9957
30	-	-	150	ANOVA, all data merged	0.9943
30	-	-	200	ANOVA, all data merged	0.9946
30	-	-	250	Levene valid, ANOVA and t-test not, middle dataset displayed	0.9958
30	-	-	300	ANOVA, all data merged	0.9945
30	-	-	350	ANOVA, all data merged	0.9945
30	-	-	400	ANOVA, all data merged	0.9945
30	-	-	500	ANOVA, all data merged	0.9927
30	7.5	60	25	ANOVA valid, all data merged	0.9933
30	7.5	60	50	ANOVA valid, all data merged	0.9929
30	7.5	60	75	ANOVA valid, all data merged	0.9937
30	7.5	60	100	ANOVA valid, all data merged	0.9928
30	7.5	60	150	ANOVA valid, all data merged	0.9911
30	7.5	60	200	ANOVA valid, all data merged	0.9859
30	7.5	60	250	ANOVA valid, all data merged	0.9868
30	7.5	60	300	ANOVA valid, all data merged	0.9876
30	7.5	60	350	ANOVA valid, all data merged	0.9845
30	7.5	60	400	ANOVA valid, all data merged	0.9844
30	7.5	60	500	ANOVA valid, all data merged	0.9840
30	10	64.7	100	ANOVA valid, all data merged	0.9940
30	10	64.7	300	ANOVA valid, all data merged	0.9899
30	10	64.7	500	ANOVA valid, all data merged	0.9882
50	-	-	25	ANOVA valid, all data merged	0.9923

50	-	-	50	ANOVA valid, all data merged	0.9898
50	-	-	75	ANOVA valid, all data merged	0.9921
50	-	-	100	ANOVA valid, all data merged	0.9887
50	-	-	150	ANOVA valid, all data merged	0.9908
50	-	-	200	Kruskal-Wallis valid, all data merged	0.9779
50	-	-	250	ANOVA valid, all data merged	0.9889
50	-	-	300	Welch's t-test valid for datasets 2 and 3, dataset 2 and 3 merged	0.9891
50	-	-	350	ANOVA valid, all data merged	0.9883
50	-	-	400	ANOVA valid, all data merged	0.9866
50	-	-	500	ANOVA valid, all data merged	0.9867
50	10	61.9	25	ANOVA valid, all data merged	0.9903
50	10	61.9	50	ANOVA valid, all data merged	0.9876
50	10	61.9	75	ANOVA valid, all data merged	0.9866
50	10	61.9	100	ANOVA valid, all data merged	0.9848
50	10	61.9	150	ANOVA valid, all data merged	0.9814
50	10	61.9	200	ANOVA valid, all data merged	0.9772
50	10	61.9	250	ANOVA valid, all data merged	0.9773
50	10	61.9	300	ANOVA valid, all data merged	0.9712
50	10	61.9	350	ANOVA valid, all data merged	0.9690
50	10	61.9	400	Levene valid, ANOVA and t-test not, middle dataset displayed	0.9682
50	10	61.9	500	ANOVA valid, all data merged	0.9708

Table A4: Data zinc-oxide particles at volume flow of $100\ cm^3 \cdot min^{-1}$ *in small column with different inlet diameters,* w_{column} *is given in* mm*,* d_{inlet} *in* mm*, and* $\dot{V}$ *in* $cm^3 \cdot min^{-1}$*.*

w_{column}	d_{inlet}	$\dot{V}$	Particle	Statistical Result	R^2
30	1	100	Glass no collector	Anova valid, all data merged	0.9957
30	1	100	10 μm ZnO	Anova valid, all data merged	0.9958
30	1	100	5 μm ZnO	Anova valid, all data merged	0.9951
30	1	100	1 μm ZnO	Anova valid, all data merged	0.9962
30	1	100	500 nm ZnO	Anova valid, all data merged	0.9949
30	1	100	10 μm Ni	Kruskal Wallis valid, all data merged	0.9934
30	1	100	5 μm Ni	Kruskal Wallis valid, all data merged	0.9934
30	1	100	1 μm Ni	Anova valid, all data merged	0.9965
30	1	100	500 nm Ni	Kruskal Wallis valid, all data merged	0.9951
30	1.5	100	Glass no collector	Anova valid, all data merged	0.9942

30	1.5	100	10 μm ZnO	Anova valid, all data merged	0.9954
30	1.5	100	5 μm ZnO	Kruskal Wallis valid, all data merged	0.9948
30	1.5	100	1 μm ZnO	Anova valid, all data merged	0.9945
30	1.5	100	500 nm ZnO	Anova valid, all data merged	0.9944
30	1.5	100	10 μm Ni	Kruskal Wallis valid, all data merged	0.9928
30	1.5	100	5 μm Ni	Welch's t-test valid for datasets 1 and 2, dataset 1 and 2 merged	0.9919
30	1.5	100	1 μm Ni	Anova valid, all data merged	0.9948
30	1.5	100	500 nm Ni	Anova valid, all data merged	0.9951
30	2.5	100	Glass no collector	Anova valid, all data merged	0.9937
30	2.5	100	10 μm ZnO	Anova valid, all data merged	0.9937
30	2.5	100	5 μm ZnO	Kruskal Wallis valid, all data merged	0.9949
30	2.5	100	1 μm ZnO	Anova valid, all data merged	0.9951
30	2.5	100	500 nm ZnO	Anova valid, all data merged	0.9952
30	2.5	100	10 μm Ni	No tests passed, middle 3 min displayed	0.9947
30	2.5	100	5 μm Ni	Kruskal Wallis valid, all data merged	0.9915
30	2.5	100	1 μm Ni	Anova valid, all data merged	0.9954
30	2.5	100	500 nm Ni	Anova valid, all data merged	0.9950

Table A5: Data nickel particles with collector for large column at different volume flows and inlet diameter of $1\ mm$*,* w_{column} *is given in* mm*, and* $\dot{V}$ *in* $cm^3 \cdot min^{-1}$*.*

w_{column}	$\dot{V}$	Particle	Statistical Result	R^2
50	350	Glass no collector	ANOVA valid, all data merged	0.9883
50	350	Glass with collector	ANOVA valid, all data merged	0.9690
50	350	10 um Ni	ANOVA valid, all data merged	0.8812
50	350	5 um Ni	ANOVA valid, all data merged	0.9885
50	350	1 um Ni	ANOVA valid, all data merged	0.9481
50	400	Glass no collector	ANOVA valid, all data merged	0.9866
50	400	Glass with collector	No tests passed, middle 3 min displayed	0.9682
50	400	10 um Ni	Student's t-test valid for datasets 2 and 3, dataset 2 and 3 merged	0.9912

50	400	5 um Ni	No tests passed, middle 3 min displayed	0.9928
50	400	1 um Ni	Kruskal Wallis valid, all data merged	0.9682
50	400	500 nm Ni	ANOVA valid, all data merged	0.9819
50	450	Glass with collector	ANOVA valid, all data merged	0.9661
50	450	10 um Ni	Kruskal Wallis valid, all data merged	0.9902
50	450	5 um Ni	ANOVA valid, all data merged	0.9914
50	450	1 um Ni	ANOVA valid, all data merged	0.9508
50	500	Glass no collector	ANOVA valid, all data merged	0.9867
50	500	Glass with collector	ANOVA valid, all data merged	0.9708
50	500	10 um Ni	Student's t-test valid for datasets 2 and 3, dataset 2 and 3 merged	0.9900
50	500	5 um Ni	Kruskal Wallis valid, all data merged	0.9892
50	500	1 um Ni	ANOVA valid, all data merged	0.8642

Table A6: Data $1\ \mu m$ *nickel particles with collector for small column at different volume flows and inlet diameter of* $1\ mm$ *at different points in time.*

Column Width	Flowrate	Time	Statistical Result	R^2
30	100	5	ANOVA valid	0.99647
30	100	20	Welch's ttest 2&3 valid	0.9966
30	100	35	ANOVA valid	0.9960
30	100	50	ANOVA valid	0.9964
30	200	5	ANOVA valid	0.9961
30	200	20	ANOVA valid	0.9954
30	200	35	ANOVA valid	0.9946
30	200	50	ANOVA valid	0.9952

A.7.3. R^2 values time recovery

Table A7: Data for particle recovery over time.

w_{column}	Particle	$d_{particle}$	d_{inlet}	$\dot{V}$	$d_{collector}$	R^2	R_{max}	k
30	ZnO	$10\ \mu m$	1	100	7.5	0.9783	0.5265	0.01848
30	ZnO	$10\ \mu m$	1	300	7.5	0.9930	0.6458	0.02427
30	ZnO	$10\ \mu m$	1	300	10	0.9667	0.4130	0.06502
30	ZnO	$10\ \mu m$	2.5	300	10	0.9630	0.6438	0.02648
30	Ni	$10\ \mu m$	1	100	7.5	0.6962	0.2175	0.1829

30	Ni	10 μm	1	350	7.5	0.9086	0.7631	0.03961
30	Ni	10 μm	1	350	10	0.9026	0.5121	0.05910
30	Ni	10 μm	2.5	350	10	0.9856	0.4718	0.08286
50	Ni	10 μm	1	400	10	0.8953	0.2894	0.08242
50	Ni	5 μm	1	400	10	0.9399	0.3039	0.05800
50	Ni	1 μm	1	400	10	0.9804	0.8159	0.02900
50	Ni	500 nm	1	400	10	0.9739	0.8875	0.006450

B. Numerical Simulations

B.1. Additional Velocity Profile Plots

B.1.1. Small Column

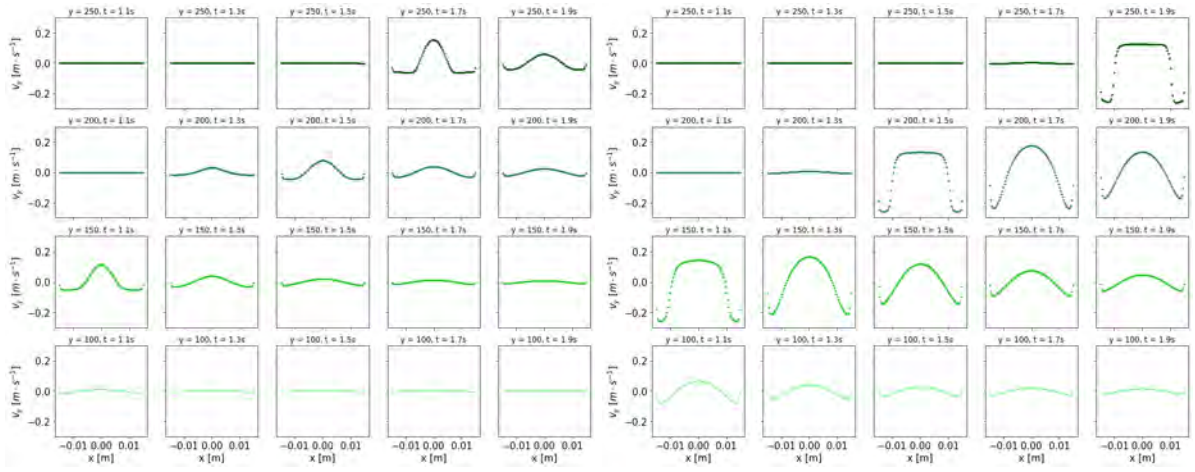

(a) *(b)*

Figure B1: Velocity profiles of water in the small column with no collector for a bubble equivalent diameter of 5 mm *(a), and* 12.5 mm *(b), the unit of the position is given in* mm*, of time in* s *which indicates the flow-time of the simulation. Positions with zero velocity can indicate the position of the bubble.*

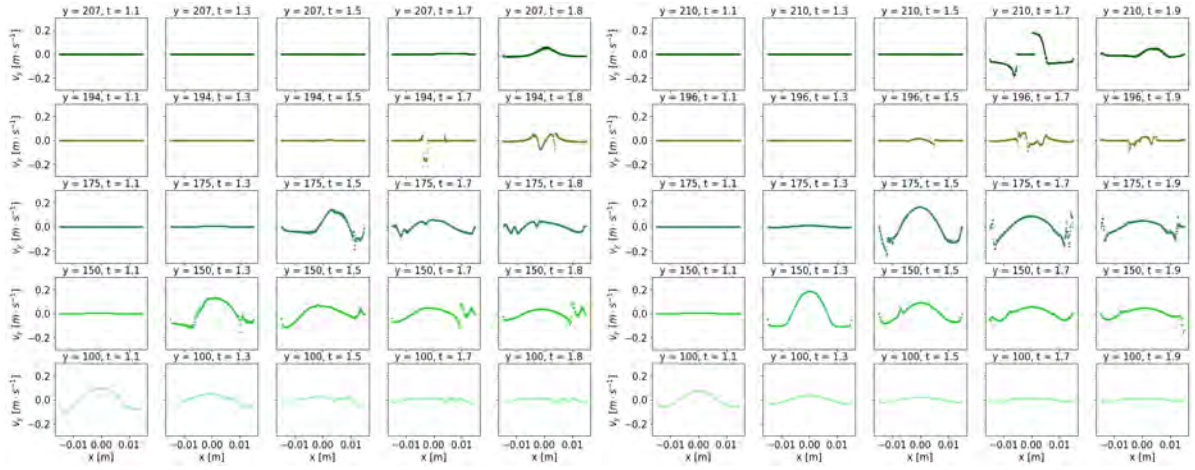

(a) *(b)*

Figure B2: Velocity profiles of water in the small column with the collector with opening diameter $7.5\ mm$ *and angle* $60°$ *(a), and opening diameter* $10\ mm$ *and angle* $64.7°$ *(b) for a bubble equivalent diameter of* $6.5\ mm$*, the unit of the position is given in* mm*, of time in* s *which indicates the flow-time of the simulation. Positions with zero velocity can indicate the position of the bubble.*

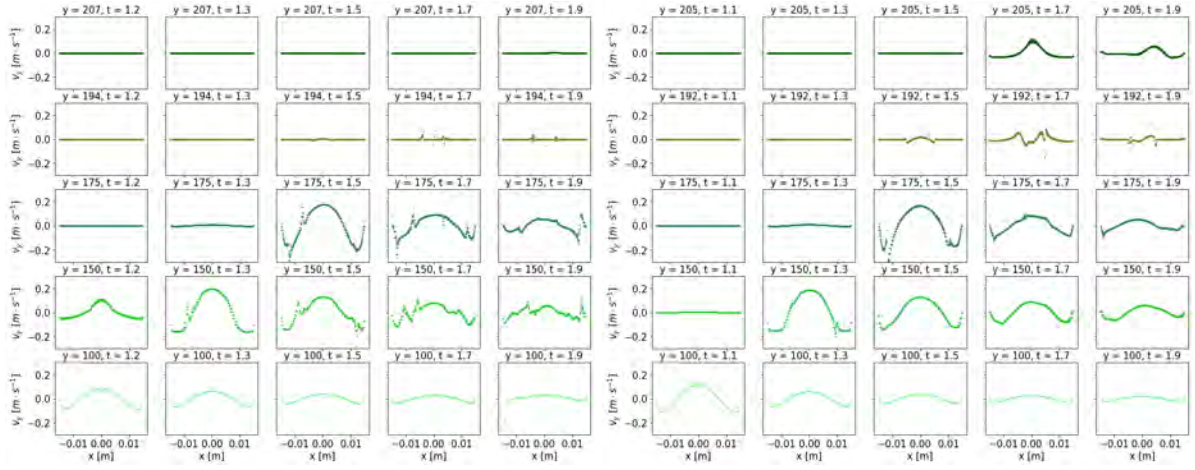

(a) *(b)*

Figure B3: Velocity profiles of water in the small column with opening diameter $7.5\ mm$ *and angle* $60°$ *(a), and opening diameter* $10\ mm$ *and angle* $60°$ *(b) for a bubble equivalent diameter of* $8\ mm$*, the unit of the position is given in* mm*, of time in* s *which indicates the flow-time of the simulation. Positions with zero velocity can indicate the position of the bubble.*

B.1.2. Large Column

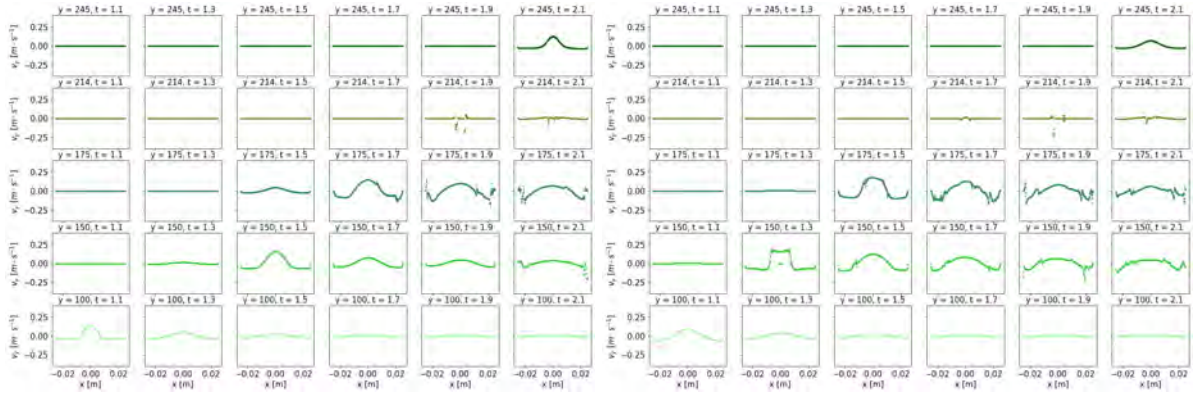

(a) *(b)*

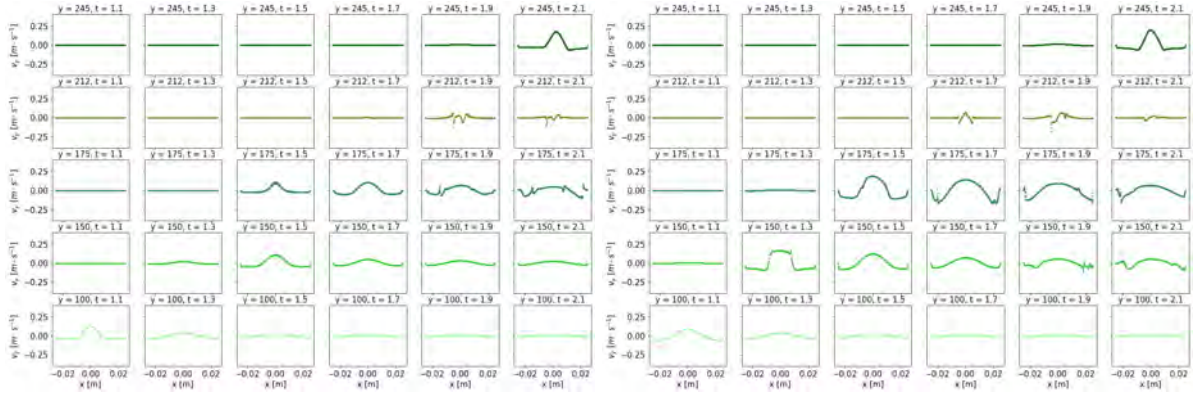

(c) *(d)*

Figure B4: Velocity profiles of water in the large column with the collector with opening diameter $7.5\ mm$ *and angle* $60°$ *for a bubble equivalent diameter of* $6.5\ mm$ *(a) and* $8\ mm$ *(b), and with the collector with opening diameter* $10\ mm$ *and angle* $61.9°$ *for a bubble equivalent diameter of* $6.5\ mm$ *(c) and* $8\ mm$ *(d), the unit of the position is given in* mm*, of time in* s *which indicates the flow-time of the simulation. Positions with zero velocity can indicate the position of the bubble.*

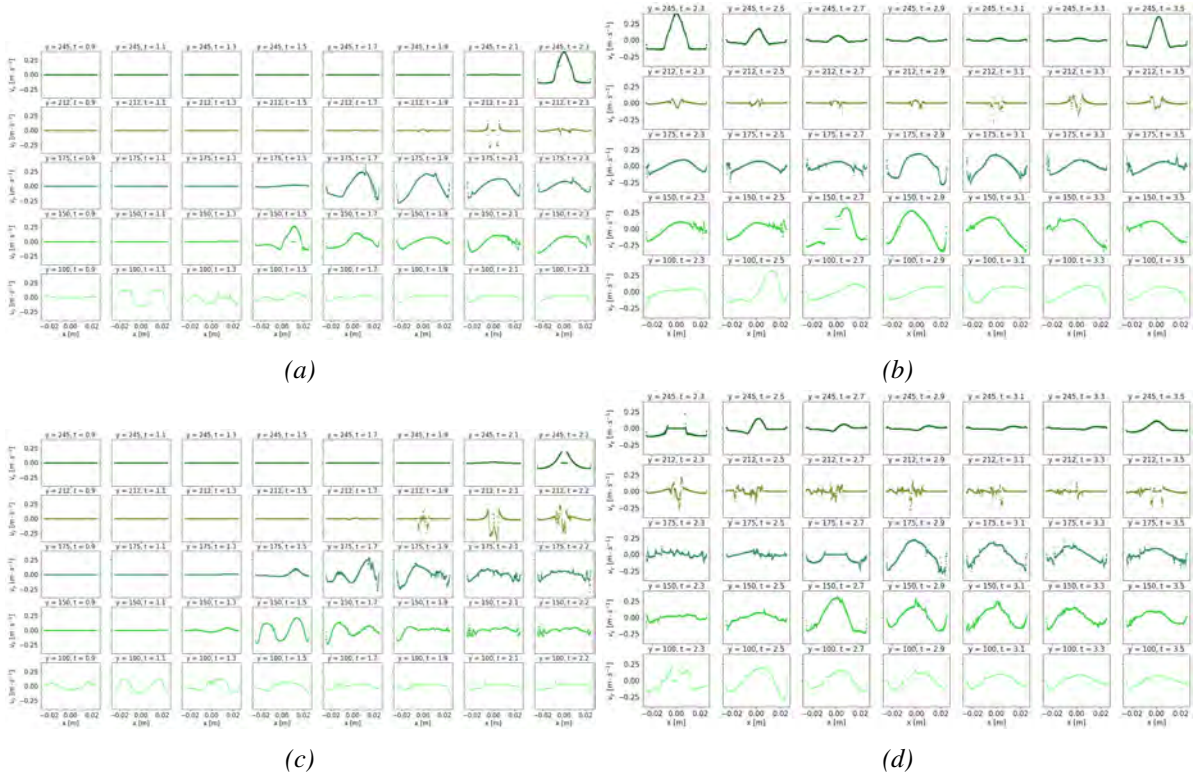

(a) *(b)* *(c)* *(d)*

Figure B5: Velocity profiles of water in the large column for three bubbles with equivalent diameter of $4.3\ mm$ *with a collector with opening diameter of* $10\ mm$ *and angle* $61.9°$ *(a), a second round of bubbles (b), and including the cone shape for three bubbles (c), and a second round of three bubbles (d), the unit of the position is given in* mm*, of time in* s *which indicates the flow-time of the simulation. Positions with zero velocity can indicate the position of the bubble.*

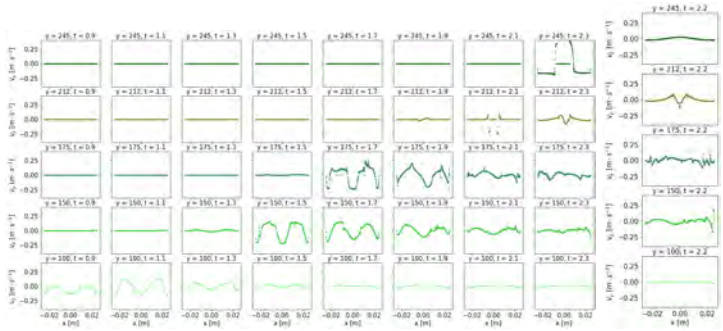

(a) *(b)*

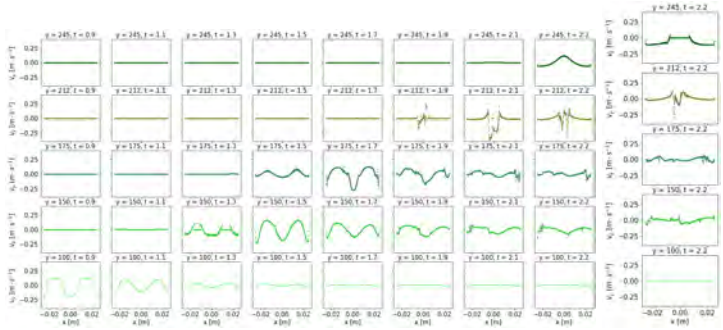

(c) *(d)*

Figure B6: Velocity profiles of water in the large column for two bubbles with equivalent diameter of $5.8\ mm$ *with a collector with opening diameter of* $10\ mm$ *and angle* $61.9°$ *(a), a second round of bubbles (b), and including the cone shape for two bubbles (c), and a second round of three bubbles (d), the unit of the position is given in* mm*, of time in* s *which indicates the flow-time of the simulation. Positions with zero velocity can indicate the position of the bubble.*

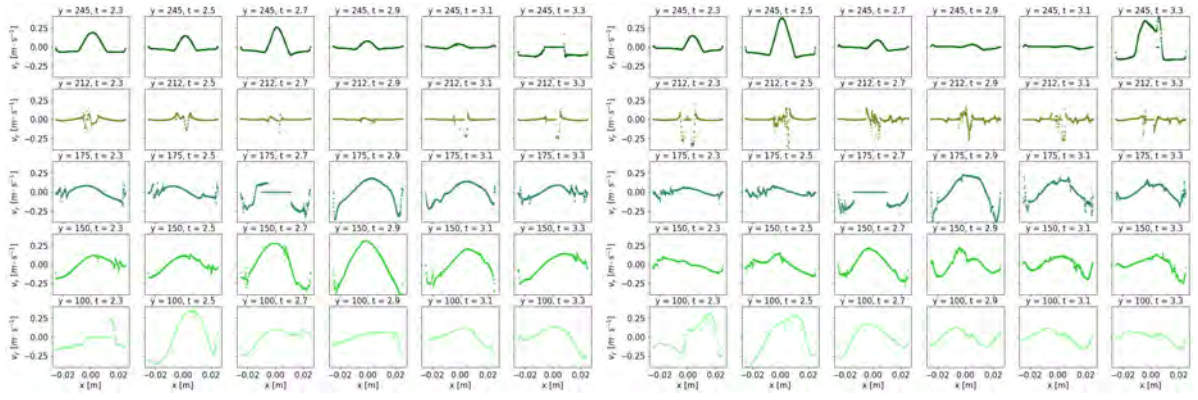

(a) *(b)*

Figure B7: Velocity profiles of water in the large column for a second round of two bubbles with equivalent diameter of $7.1\ mm$ *with a collector with opening diameter of* $10\ mm$ *and angle* $61.9°$ *(a), and including the conical shape (b), the unit of the position is given in* mm*, of time in* s *which indicates the flow-time of the simulation. Positions with zero velocity can indicate the position of the bubble.*

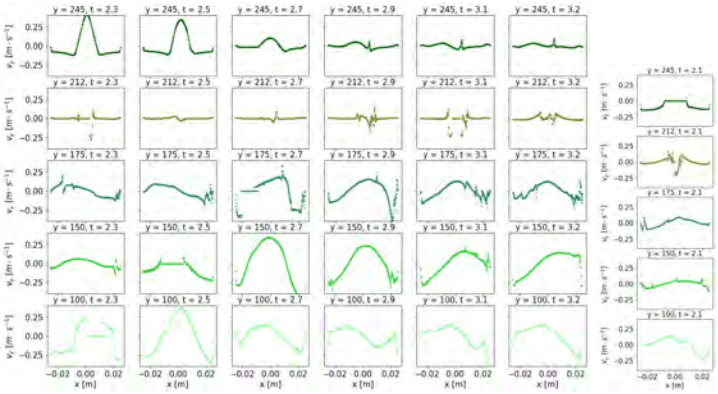

(a) *(b)*

Figure B8: Velocity profiles of water in the large column for a second round of three bubbles with equivalent diameter of $5.4\ mm$ *with a collector with opening diameter of* $10\ mm$ *and angle* $61.9°$ *(a), and including the conical shape of the column (b), the unit of the position is given in* mm*, of time in* s *which indicates the flow-time of the simulation. Positions with zero velocity can indicate the position of the bubble.*

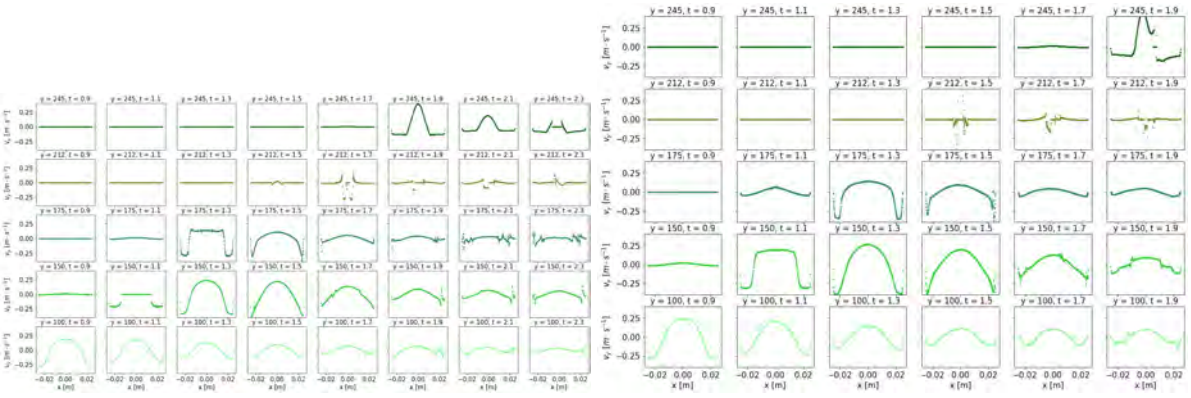

(a) *(b)*

Figure B9: Velocity profiles of water in the large column for a bubble with equivalent diameter of $20\ mm$ *with a collector with opening diameter of* $10\ mm$ *and angle* $61.9°$ *(a), and including the conical shape of the column (b), the unit of the position is given in* mm*, of time in* s *which indicates the flow-time of the simulation. Positions with zero velocity can indicate the position of the bubble.*

B.2. Additional Figures for Particle Behavior

B.2.1. Small Column

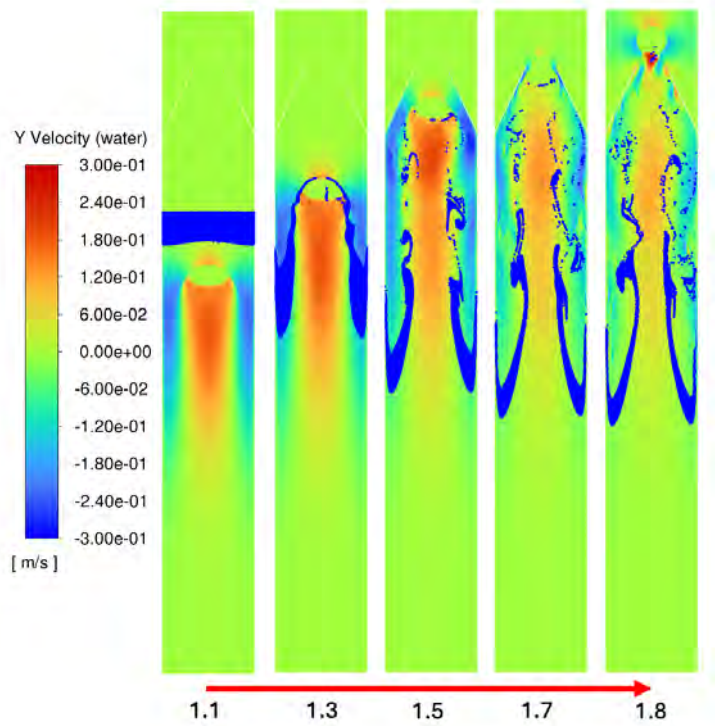

Figure B10: Particle lift of $10\ \mu m$ *molybdenum particles in the small column, with a bubble with bubble equivalent diameter of* $10\ mm$*, with a collector with opening diameter* $10\ mm$ *and angle* $64.7°$*, the timeline is given in* s *of flow-time.*

B.2.2. Large Column

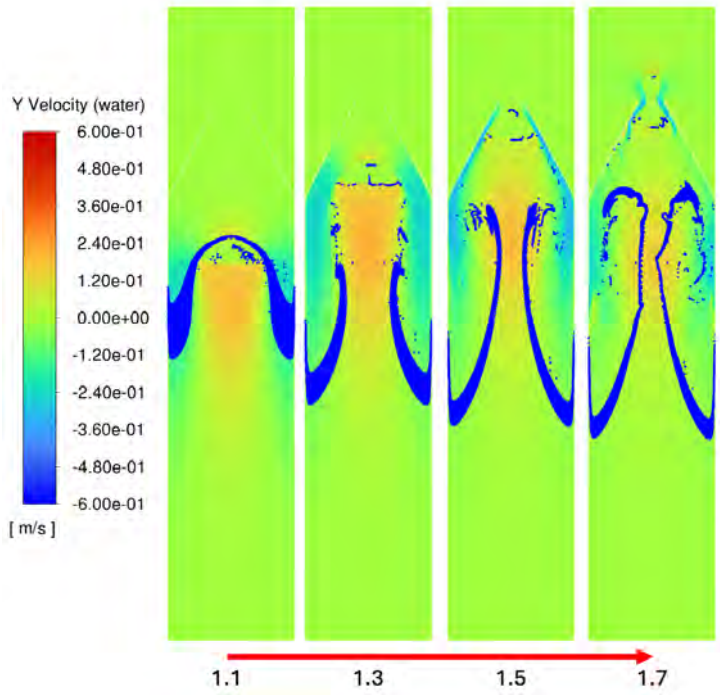

Figure B11: Particle lift of $10\ \mu m$ *nickel particles in the large column, with a bubble with bubble equivalent diameter of* $15\ mm$*, with a collector with opening diameter* $10\ mm$ *and angle* $61.9°$*, the timeline is given in* s *of flow-time.*

C. Python Codes

All python codes can be found on Github using the following QR code.